論文 / 著書情報
Article / Book Information

題目(和文)	酸化物超伝導体の磁化応答：下部臨界磁場と表面バリアー
Title(English)	Magnetic response of oxide superconductors : Lower critical field and surface barrier
著者(和文)	栃原信二郎
Author(English)	
出典(和文)	学位:博士(理学), 学位授与機関:東京工業大学, 報告番号:乙第3408号, 授与年月日:2000年3月31日, 学位の種別:論文博士, 審査員:垣花 真人
Citation(English)	Degree:Doctor (Science), Conferring organization: Tokyo Institute of Technology, Report number:乙第3408号, Conferred date:2000/3/31, Degree Type:Thesis doctor, Examiner:
学位種別(和文)	博士論文
Type(English)	Doctoral Thesis

A Thesis

Magnetic Response of Oxide Superconductors

– Lower Critical Field and Surface Barrier –

SHINJIRO TOCHIHARA

November 1999

CONTENTS

Chapter 1

Introduction

I. HISTORICAL REVIEW

The history of superconductivity opened in 1911 when the total lack of resistance to electrical currents in mercury at the liquid helium temperature was discovered by Onnes [1]. Following this dramatic discovery, many physicists tried to find another material which shows superconductivity and more than 20 metallic elements appeared to become superconducting below the specific temperatures, called the *critical temperature*, T_c.

In 1933, Meissner and Ochsenfeld [2] made a new peculiar discovery; an applied magnetic field H to a superconductor is completely excluded from the interior of the sample as far as H does not exceed a certain threshold. This finding, the so-called *Meissner effect*, is crucial in understandings of superconductivity, i.e., superconductivity is essentially perfect diamagnetism. Supercurrents induced by the applied field at the surface of a sample produce magnetic fields in the opposite direction, resulting in a cancellation or a complete exclusion of the applied field. This phenomenon, the Meissner effect, is reversible, and the field begins to penetrate into the sample when H exceeds a certain threshold H_c. This magnetic threshold H_c which destroys the superconducting state is expected to be related to the difference between free energies of the normal and superconducting states in zero magnetic field. More concretely, H_c which is called the *thermodynamic critical field* can be expressed by

$$\frac{H_c^2(T)}{8\pi} = f_n(T) - f_s(T), \tag{1.1}$$

where f_n and f_s denote the Helmholtz free energies per unit volume in the normal and superconducting states respectively, and $H_c^2(T)/8\pi$ is the magnetic pressure acting on the sample per unit volume.

To interpret these specific characteristics of superconductivity, the first phenomenological theory was formulated by F. London and H. London [3]. They gave two electromagnetic equations which could account for two distinctive features of superconductivity, the perfect conductivity and the perfect diamagnetism.

$$\boldsymbol{E} = \frac{\partial}{\partial t}(\Lambda \boldsymbol{J}), \tag{1.2}$$

$$\boldsymbol{B} = -\mathrm{rot}\,\Lambda \boldsymbol{J}, \tag{1.3}$$

where

$$\Lambda = \frac{m}{n_s e^2}. \tag{1.4}$$

$\boldsymbol{E}$ is electric fields, $\boldsymbol{J}$ is the supercurrent density, m is the electron mass, n_s is the superconducting carrier density, and $\boldsymbol{B}$ is the magnetic flux density.

Equation (1.2) represents the perfect conductivity, indicating that the electric field $\boldsymbol{E}$ accelerates superconducting electrons. Using Eq. (1.3) together with the Maxwell equation rot$\boldsymbol{B} = \boldsymbol{J}$, they derived a differential equation

$$\nabla^2 \boldsymbol{B} - \frac{1}{\lambda^2}\boldsymbol{B} = 0. \tag{1.5}$$

This differential equation, the London equation, states that the magnetic field can exist only in the range λ at the edges of a superconductor, but exponentially drops to zero, i.e., expels the field from the inside of the sample (the Meissner effect). λ defined in Eq. (1.5) is well known as the *London penetration depth*.

The London equations have been successful for descriptions of the remarkable behaviors of a superconductor. However, their equations are not perfectly satisfactory to understand all superconducting phenomena, because in the London theory, a superconductor is treated entirely superconducting or entirely normal. To overcome this difficulty, Ginzburg and Landau [4] developed a phenomenological theory in 1950, in which the spatial dependence of the superconducting state is taken into consideration through a superconducting order parameter $\Psi(\boldsymbol{r})$ which has a form of wave function and is related to the superfluid density as $n_s = |\Psi(\boldsymbol{r})|^2$.

Assuming the Helmholtz free energy of the system in question can be expanded in terms of $\Psi(\boldsymbol{r})$, they derived a differential equation, the so-called Ginzburg–Landau (GL) equation, together with an expression of the supercurrent $\boldsymbol{J}_s$,

$$\frac{1}{2m^*}[\hbar\nabla - e^*\boldsymbol{A}(\boldsymbol{r})]^2\Psi(\boldsymbol{r}) + \beta|\Psi(\boldsymbol{r})|^2\Psi(\boldsymbol{r}) = -\alpha\Psi(\boldsymbol{r}), \tag{1.6}$$

$$\boldsymbol{J}_s = \frac{e^*\hbar}{2m^*}[\Psi^*(\boldsymbol{r})\nabla\Psi(\boldsymbol{r}) - \Psi(\boldsymbol{r})\nabla\Psi^*(\boldsymbol{r})] - \frac{e^{*2}}{m^*}|\Psi(\boldsymbol{r})|^2\boldsymbol{A}(\boldsymbol{r}), \tag{1.7}$$

where m^* is the effective electron mass, e^* is the charge of carriers, and α, β are constants. The magnetic field is included via the vector potential $\boldsymbol{A}(\boldsymbol{r})$. Unfortunately, very few researchers remarked the GL theory at that time. However, this theory is now the most conventional and useful phenomenological description with the sound physical basis underlying it.

Several years later from publication of the GL theory, Pippard [5] introduced the coherence length ξ which plays a similar role to the electron mean-free path in normal metals, and insisted that the superconducting wave function should have the specific extent correlated to ξ.

In 1957, Bardeen, Cooper, and Schrieffer [6] have constructed a microscopic theory (the BCS theory), of which the essence lies on a bound pair of two electrons created by a virtual exchange of phonons. The important results of the BCS theory are that the bound electrons with spins in the opposite direction (Cooper pairs) condense quantum mechanically into the ground state and that the energy needed to break a Cooper pair into two electrons is $2\Delta(T)$, i.e., twice of the energy gap $\Delta(T)$ yielded in the condensing state. Besides, the theory gave an equation for evaluations of the critical temperature.

$$T_c = \frac{1.764}{k_{\mathrm{B}}}\Delta(0), \tag{1.8}$$

where k_{B} is a Boltzmann constant.

Generalization of the BCS theory was soon made by Bogoliubov [7] in 1958, where he derived equations known as the Bogoliubov equations and dealt with the quasiparticles in a superconductor. Meanwhile, Gor'kov [8] independently gave formulations for a superconducting state using Green's functions. Noteworthy in this work is that the GL equations released in 1950 can be derived as an extreme case of the BCS theory near T_c, and the order parameter introduced in the GL theory physically corresponds to the BCS gap parameter $\Delta(T)$. In addition, Abrikosov [9] argued that the GL parameter defined as the ratio of the London penetration depth λ and the coherence length ξ, $\kappa = \lambda/\xi$, can be used as a mark which distinguishes type-I ($\kappa > 1/\sqrt{2}$) and type-II ($\kappa < 1/\sqrt{2}$) superconductors.

The superconducting state of type-I superconductors is destroyed when the applied magnetic field exceeds the thermodynamic critical field H_c. On the contrary, in type-II superconductors, the Meissner state holds up to the lower critical field H_{c1}, but above it, quantized magnetic flux ϕ_0 penetrates into the sample and the mixed (normal and superconducting) state emerges. In the applied field over the higher critical field H_{c2}, type-II superconductors fall in the normal state.

Owing to the establishment of these stimulating and successful descriptions reviewed above, the fundamental mechanism of a superconducting state has been convinced to be essentially realized.

In 1986, the world of superconductivity was struck by a violent shock when Bednorz and Müller [10] reported the existence of a material with the critical temperature beyond the limit predicted by the BCS theory. The new material found by them is a cuprate-based oxide superconductor, $La_{1.9}Ba_{0.1}CuO_4$, which shows superconductivity at around 30 K.

Soon after their discovery of a new class superconductor, Chu *et al.* [11] succeeded in fabrications of another cuprate superconductor $YBa_2Cu_3O_{7-\delta}$ (Y123), of which the critical temperature was beyond the liquid nitrogen temperature for the first time, giving a vast dream for applications of superconductivity. In the following years, a worldwide competition for searching high-T_c cuprate superconductors has been evolved and many related materials with critical temperatures ranging up to 134 K have been reported [12]. Table 1.1 lists representative high-T_c cuprates and their critical temperatures.

The specific structure of the cuprate superconductor has been thoroughly reviewed by Park and Snyder [13]. According to their article, the structure of most of the known cuprate superconductors is shown to belong structurally to a single family and is mainly characterized as followings:

(1) The structure is closely related to each other, i.e., cuprate superconductors result from the stacking of perovskite units with extra layers sandwiched between them.

(2) Cuprate superconductors possess the same structural element essential to high-T_c cuprate superconductivity; CuO_2 sheets that are separated by nonsuperconducting planes.

(3) T_c is related to the oxidation state of the Cu ion in the CuO_2 plane.

(4) The role of the insulating layers is to either squeeze or stretch the CuO bonds in the infinite layer to put them in the required oxidation state.

As typical examples, we show the structures of $Bi_2Sr_2CaCu_2O_{8+\delta}$ (Bi2212) in Fig. 1.1 and Y123 in Fig. 1.2. A remarkable asymmetry of the structures is worth to notice.

The theoretical basis of high-T_c superconductors which are far beyond the framework of the BCS theory has not been established yet. To the further promotion of the understandings, precise and reliable experimental evidences are indispensable.

TABLE 1.1. Cuprate superconducting compounds and their T_c [13].

Compound	T_c (K)
$(La,Ba)_2CuO_{4-\delta}$	38
$La_{1.6}Sr_{0.4}CaCu_2O_{6\pm\delta}$	60
$YBa_2Cu_3O_7$	95
$YBa_2Cu_4O_8$	80
$Y_2Ba_4Cu_7O_{15}$	92
$TlBa_2Ca_{n-1}Cu_nO_{2n+3}$ $(n = 3)$	120
$Tl_2Ba_2Ca_{n-1}Cu_nO_{2n+4}$ $(n = 3)$	127
$Bi_2Sr_2Ca_{n-1}Cu_nO_{2n+4}$ $(n = 3)$	110
$Hg_2Ba_2Ca_{n-1}Cu_nO_{2n+4+\delta}$ $(n = 3)$	134
$CuBa_2Ca_{n-1}Cu_nO_y$	120
$Sr_2Ca_{n-1}Cu_nO_y$	90
$Pb_2Sr_2(Ca,Y,Nd)Cu_3O_8$	70
$Pb_2(Sr,La)_2Cu_2O_6$	32
$PbBaSrYCu_3O_8$	50
$(Pb,Cu)(Ba,Sr)_2(Y,Ca)Cu_2O_7$	53
$Pb_{0.5}Sr_{2.5}(Y,Ca)Cu_2O_7$	104
$(Pb,Cu)(Sr,La)_2CuO_5$	32
$(Nd,Ce)_2CuO_{4-\delta}$	24
$(Nd,Ce,Sr)_2CuO_{4-\delta}$	28
$(Pb,Cu)(Eu,Ce)_2(Sr,Eu)_2Cu_2O_9$	25
$(Eu,Ce)_2(Ba,Eu)_2Cu_3O_{10}$	43
$Bi_2Sr_2(Gd,Ce)_2Cu_2O_{10}$	34
$Tl_{0.5}Pb_{0.5}Sr_4Cu_2(CO_3)O_7$	70
$(Ba,Sr)_2CuO_2(CO_3)$	40
$Sr_{4-x}Ba_xTlCu_2CO_3O_7$	62
$Tl_{0.5}Pb_{0.5}Sr_2Gd_{2-x}Ce_xCu_2O_{9-\delta}$	45
$NbSr_2(Gd,Ce)_2Cu_2O_y$	27
$Bi_2Sr_{6-x}Cu_3O_{10}(CO_3)_2$	40
$(Cu_{0.5}C_{0.5})Ba_2Ca_{n-1}Cu_nO_{2n+3}$ $(n = 3)$	117
$YCaBa_4Cu_5(NO_3)_{0.3}(CO_3)_{0.7}O_{11}$	82
$CuSr_{2-x}La_xYCu_2O_{7+\delta}$	60
$GaSr_2Ln_{1-x}Ca_xCu_2O_7$	73
$(C_{0.35}Cu_{0.65})Sr_2(Y_{0.73}Ce_{0.27})_2Cu_2O_x$	18
$Bi_4Sr_4CaCu_3O_{14+x}$	84
$(Sr_{2-x}Bi_x)(Ln_{2-y}Ce_y)Cu_2O_{8-\delta}$	30
$Sr_2Nd_{1.5}Ce_{0.5}NbCu_2O_{10-\delta}$	28

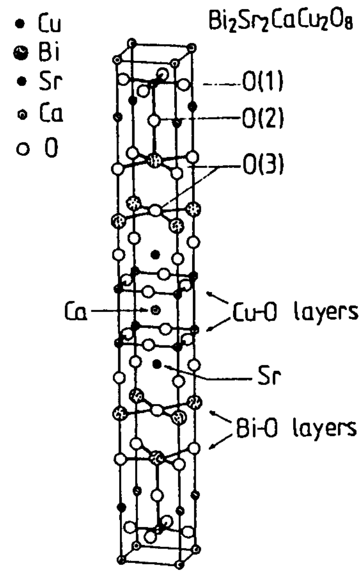

FIG. 1.1. Schematic structure of Bi2212 [14].

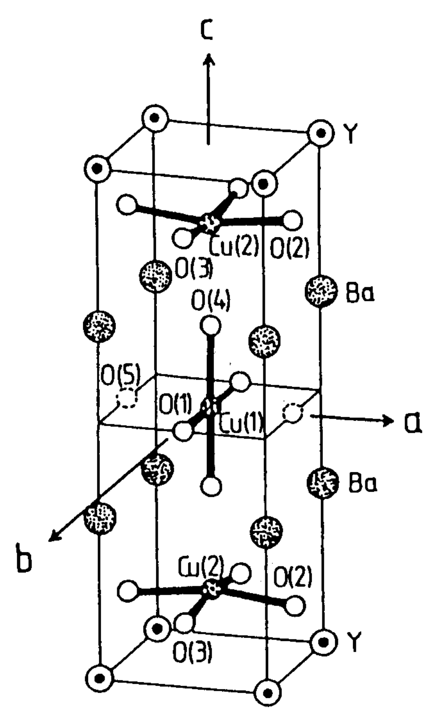

FIG. 1.2. Schematic structure of Y123 [15].

II. CRITICAL-STATE MODEL

Measurements of the magnetic characteristic of superconductors have supplied crucial informations of the superconducting state. The essential understandings of the magnetic response for type-II superconductors started with the work by Abrikosov [9] who has shown the quantized flux penetration occurs at the lower critical field H_{c1} and completes at the higher critical field H_{c2}. In the field region between H_{c1} and H_{c2}, the specimen is presumed to possess a structure of fluxons, i.e., a mixed state.

A remarkable paper by Bean [16] on the magnetization of type-II superconductors was first published in 1962. The basic premise of his theory, called the critical-state model, is that, when a magnetic field is applied to a sample, a macroscopic supercurrent circulates in the sample with a constant critical-current density J_c. An additional assumption for the original critical-state model is that the lower critical field is assumed to be zero. Surprisingly enough his simplified theory appeared to account for the magnetic properties of inhomogeneous mixed state.

On the assumption that the critical-current density as a function of the local flux density inside the specimen B_i has the form

$$J_c(B_i) = \frac{k}{B_0 + |B_i|}, \tag{1.9}$$

where k and B_0 are temperature-dependent material parameters, Kim, Hempstead, and Strnad [17, 18] and Anderson [19] made more refined investigations of the critical phenomena of type-II superconductors. As pointed out by Chen and Goldfarb [20], the relation Eq. (1.9) assumed in the Kim–Anderson (KA) model is a very generalized form of the critical-state model because, when $B_0 \gg B_i$, it is equivalent to the linear model [21] $J_c(B_i) = A - C|B_i|$, where A and C are positive constants, and to the Bean model [22, 23] when k and B_0 become infinite in such a way that k/B_0 is a constant. When $B_0 = 0$, it leads to the power-law model [24, 25] $J_c(B_i) = k/|B_i|$, where the power of B_i is -1, the so-called simplified Kim model.

In the critical-state model, the Lorentz force $\boldsymbol{J} \times \boldsymbol{B}$ imposed on a flux quantum is assumed to be balanced with the pinning force inside the specimen. From Eq. (1.9), therefore, we realize that the material parameter k has a clear physical meaning as the pinning force density, although the form of the temperature dependence has not been determined yet. Meanwhile, a physical interpretation to the material parameter B_0 is still conflicting. Besides, in the KA model, the effects of surface barriers ΔH and lower critical fields H_{c1} which may be crucial in the magnetic response of a superconductor subjected to lower-level applied fields have not been taken into account.

For more elaborate applications of the KA critical-state model, we need to find solutions of these unresolved problems. As the first step, we have modified the Bean model by taking into consideration ΔH and H_{c1} and derived all the magnetization equations [26]. More recently, we have made further modifications of the critical-state model, where the extension of the KA model has been attempted by taking explicitly into consideration ΔH and H_{c1} [27]. Within the construct of this modified KA model, we have fully derived the magnetization equations of type-II superconductors. The temperature dependences of the material parameters k and B_0 have also been obtained through analyses of the magnetization curves as well as the complex susceptibility of the sample.

We expect the theoretical formulations of the critical-state model developed in this thesis contribute to bring to light the magnetic characteristics which have not been clearly elucidated.

III. SCOPE OF THIS THESIS

The main theme of this thesis is the establishment of the modified KA model and the confrontation of the theory with experimental data. Chapters 2, 3, 4, and 5 form the central part of this thesis.

In Chap. 2, we extensively evolve the modified KA critical-state model by taking into consideration both ΔH and H_{c1}. A sample is assumed to be located in a time-dependent magnetic field superimposed on a dc field. Detailed derivations of the magnetization equations are presented. From the computed magnetization curves, the effect of ΔH and H_{c1} on the magnetic behavior of type-II superconductors has been revealed.

In Chap. 3, we present measurements as well as analyses of the temperature dependence of H_{c1} for two kinds of cuprate superconductors, Bi2212 and Y123 single crystals. Analyses were made using the appropriate magnetization equations derived in the preceding chapter. Of particular importance is that the anomaly observed in H_{c1} of Bi2212 in the lower temperature region would be attributed to a proximity effect induced in the region between the CuO_2 planes. In addition, the results indicate both the samples possess the nature of d-wave pairings.

For examinations of surface barriers, we have to make preliminary determinations of the temperature dependence of the material parameters k and B_0. This can be partially achieved by simulating the measured magnetization curves, where k and B_0 are used as fitting parameters. However, very near T_c, the above technique is not useful and we need help of complex magnetic susceptibilities. By this reason, in Chap. 4, we first treat complex susceptibilities χ_n generated from a superconductor in a time-dependent magnetic field. From measurements of χ_n, we deduce the magnetization curve very near T_c. Thus we have determined the temperature dependence of k and B_0 in a wide temperature range below T_c, giving more sound basis for applications of the KA or modified KA model.

In Chap. 5, surface barriers ΔH have been examined by using thin-film and bulk cuprates, where the temperature dependences of k and B_0 determined in the preceding chapter are used. There are two different origins of ΔH; the geometrical barrier and the Bean–Livingston barrier. Generally speaking, experimental evaluations of ΔH from magnetization curves are not easy. Meanwhile, as described in the preceding chapter, higher-harmonic susceptibilities χ_n ($n \geq 2$)

show very complicated profiles, sensitively reflecting a slight distortion of the magnetization curves. Based on this fact, we examine ΔH of Bi2212 and Y123 single crystals (thin film and bulk) with the intention of establishing a research technique for investigations of ΔH in terms of χ_n.

There have been many stimulating studies on a remarkable correlation between T_c of cuprate-based superconductors and the superconducting carrier density of the two-dimensional CuO_2 plane. Motivated by these previous investigations, in Chap. 6, we attempt to search the dependence of T_c on the carrier density through H_{c1}. Measurements of H_{c1} for Y/Pb-doped Bi2212 and Co/Ca-doped Y123 single crystals were carried out. Discussion was made with the aid of the London theory and the GL theory.

Finally, we would like to comment on the superconducting critical temperature T_c. In current publications, the definition to T_c is not always clear, i.e., the onset or the midpoint or the end point of the superconducting transition. Our studies presented in this thesis use the onset temperature as T_c. However, to avoid complexity, the critical temperature referred from other groups is also denoted by the same notation T_c throughout this thesis.

Chapter 2

Magnetization of Type-II Superconductors in the Critical-State Model

I. INTRODUCTION

The critical-state model first introduced by Bean [16, 22] and London [23] has been widely used for study of magnetic properties of type-II superconductors. The essential aspect of this model is that, when a magnetic field is applied to a sample, a macroscopic supercurrent circulates in the sample with a critical-current density $J_c(B_i)$, where B_i is the local flux density inside the specimen.

The simplest case proposed by Bean [16] is that J_c is a constant independent of B_i. Despite of the simplified treatment, Bean's model has been proved to be very useful for investigations of the magnetic response of superconductors.

On the assumption that the critical-current density has the form

$$J_c(B_i) \;=\; \frac{k}{B_0 + |B_i|}, \tag{2.1}$$

where k and B_0 are temperature-dependent material parameters, Kim, Hempstead, and Strnad [17, 18] and Anderson [19] studied the critical phenomena of type-II superconductors. The relation given by Eq. (2.1) is a very generalized form of the critical-state model, because it asymptotically leads to either the linear model [21] or the Bean model [22] or the power-law model [24, 25], depending on the relative magnitude of k, B_0, and B_i.

In a series of investigations of magnetic properties of cuprate-based oxide superconductors, we extensively used the magnetization equations derived by Yamamoto *et al.* [28] in the framework of the Kim–Anderson (KA) model and found that the magnetic behavior of the specimens can be qualitatively well reproduced [29–32]. However, in the derivations of the magnetization equations, they have neither taken into consideration the surface barrier ΔH nor the lower critical field H_{c1}, i.e. both of these were assigned to zero.

The role of ΔH and/or H_{c1} to magnetization of type-II superconductors has been studied by many workers [33–76]. However, to the author's knowledge, complete derivations of the magnetization equations including ΔH and H_{c1} have not so far been published.

As the simplest case, we first attempt to derive the magnetization equations in the framework of the Bean model modified by taking into consideration ΔH and H_{c1} [26]. Using this modified Bean model, we have calculated the initial magnetization curves and full-hysteresis loops of type-II superconductors immersed in an external field $H(\omega t) = H_{dc} + H_{ac}\cos(\omega t)$, where H_{dc} (≥ 0) is a dc bias field and H_{ac} (> 0) is an ac field amplitude. We consider an infinitely long cylinder with radius a, and the applied field along the cylinder axis. Denoting the maximum and minimum values of H by H_A ($= H_{dc} + H_{ac}$) and H_B ($= H_{dc} - H_{ac}$), magnetization equations $M(H)$ for full-hysteresis loops are derived for four different ranges of H_A: $0 < H_A \leq H_{c1} + \Delta H$, $H_{c1} + \Delta H \leq H_A \leq H_{c1} + \Delta H + H_p$, $H_{c1} + \Delta H + H_p \leq H_A \leq H_{c1} + \Delta H + 2H_p$, and $H_{c1} + \Delta H + 2H_p \leq H_A$. Here H_p is the field for full penetration. Each of these four cases is further classified for several ranges of H_B. To describe completely the descending and ascending branches of full-hysteresis loops for any H_A and H_B, 83 stages of H were considered. To verify the derivations, all the equations were confirmed to be continuous at their end points.

To obtain more elaborate magnetization equations of type-II superconductors in an external field similar to the above case, we have fully extended our derivations to the modified KA model which explicitly involves ΔH and H_{c1} [27]. Although both ΔH and H_{c1} depend on the local flux density, in the following discussion, we tentatively assume that they do not depend on the flux density.

In this chapter, we describe detailed derivations of the magnetization equations by the modified KA model. To complete full-hysteresis loops, it is needed to consider 113 stages of H. Using these equations, we calculate $M(H)$ curves and verify that the curves are continuous at their end points. For a further test of our derivations, we reduced $M(H)$ equations in the limit of $\Delta H \to 0$ and $H_{c1} \to 0$, and compared them with the results of Ref. 28. From the computed $M(H)$ curves, the effect of ΔH and H_{c1} on the magnetic behavior of type-II superconductors can be plainly seen.

II. INITIAL MAGNETIZATION AND FULL-PENETRATION FIELD FOR AN INFINITE CYLINDER

A. General Expression for Magnetization and Local Current Density

According to Dunn and Hlawiczka [34], the magnetization curve for type-II superconductors is somewhat complicated due to the nonzero values of ΔH and H_{c1}, but the effective field in the sample H_{eff} may be described by the following expression [34],

$$H_{eff} = H - \frac{H}{|H|}H_{c1} - \frac{dH/dt}{|dH/dt|}\Delta H, \tag{2.2}$$

where H is the applied field.

Adopting their proposal, we derive the general expression for magnetization. We consider an infinite cylindrical specimen with radius a, where the boundary of the sample is at $x = a$. An external field H is applied along the axis. In this configuration, both the local current density and the local magnetic-flux density are expressed as functions of x, and are denoted as $J(x)$ and $B_i(x)$, respectively.

When an external field H is applied, macroscopic supercurrent $J(x)$ flows in the sample and $B_i(x)$ is written as

$$B_i(x) = \mu_0 H_{eff} + \mu_0 \int_x^a J(x')dx', \tag{2.3}$$

where $\mu_0 = 4\pi \times 10^{-7}$ H/m. Using $B_i(x)$, we obtain the average flux density $B(H)$ in the sample

$$B(H) = \frac{2}{a^2}\int_0^a xB_i(x)dx. \tag{2.4}$$

Thus, the average magnetization $M(H)$ of the sample is given by

$$M(H) = B(H)/\mu_0 - H. \tag{2.5}$$

From Eq. (2.1) and Ampère's law, $\nabla \times \boldsymbol{B} = \mu_0 \boldsymbol{J}$, we obtain the local flux density $B_i(x)$ as

$$B_i(x) = -\mathrm{sgn}(B_i)B_0 \pm [B_0^2 - \mathrm{sgn}(JB_i)2\mu_0 k(x+c)]^{1/2}, \tag{2.6}$$

where the sign function $\mathrm{sgn}(X)$ is 1 if $X > 0$, -1 if $X < 0$, and 0 if $X = 0$, and c is an integration constant to be determined by the boundary conditions. Using Eqs. (2.1) and (2.6), we obtain the general expression for $J(x)$;

$$J(x) = \frac{\mathrm{sgn}(J)k}{[B_0^2 - \mathrm{sgn}(JB_i)2\mu_0 k(x+c)]^{1/2}}. \tag{2.7}$$

B. Current Distribution and Full-Penetration Field

We start from the initial state, $H = J(x) = B_i(x) = 0$, and increase H in the direction of the cylinder axis. When the applied field exceeds $H = H_{c1} + \Delta H$, the supercurrent J (of negative sign) begins to penetrate from the sample surface ($x = a$) inward. If the supercurrent penetrates until $x = x_0$, $J(x)$ is given as

$$J(x) = 0 \qquad (0 \le x \le x_0), \tag{2.8a}$$

$$J(x) = j_0(x) = \frac{-k}{[B_0 + 2\mu_0 k(x+c)]^{1/2}} \qquad (x_0 \le x \le a), \tag{2.8b}$$

where $j_0(x)$ is defined as the supercurrent corresponding to $J(x)$ in the region $x_0 \le x \le a$. From the boundary condition $j_0(a) = -J_c(\mu_0 H_{eff})$, where $H_{eff} = H - H_{c1} - \Delta H$, we get

$$2\mu_0 kc = (B_0 + \mu_0 H_{eff})^2 - B_0^2 - 2\mu_0 ka. \tag{2.9}$$

Substituting Eq. (2.9) into Eq. (2.8b), we obtain

$$j_0(x) = \frac{-k}{[(B_0 + \mu_0 H_{eff})^2 - 2\mu_0 k(a-x)]^{1/2}} = -k(p_0 x + q_0)^{-1/2}, \tag{2.10}$$

where

$$p_0 = 2\mu_0 k, \tag{2.10a}$$

$$q_0 = (B_0 + \mu_0 H_{eff})^2 - 2\mu_0 ka. \tag{2.10b}$$

From the boundary condition $j_0(x_0) = -J_c(0)$, x_0 can be obtained;

$$x_0 = a - [(B_0 + \mu_0 H_{eff})^2 - B_0^2]/2\mu_0 k. \tag{2.11}$$

Since the full-penetration field H_p is H_{eff} for $x_0 = 0$ [see Fig. 2.1(a) represented schematically by a straight-line segment], we obtain

$$H_p = [(B_0^2 + 2\mu_0 ka)^{1/2} - B_0]/\mu_0. \tag{2.12}$$

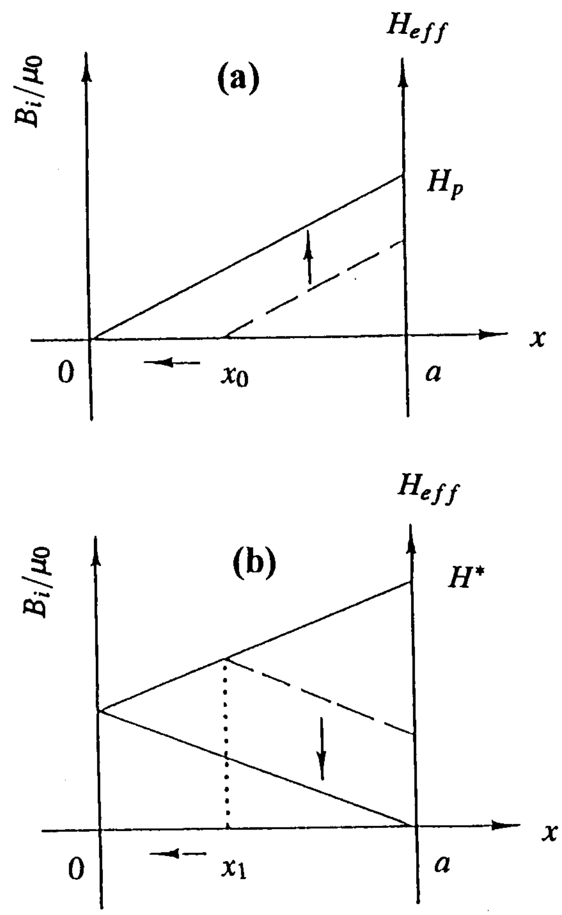

FIG. 2.1. Definition of (a) the full-penetration field H_p in the ascending branch and (b) a related parameter H^* in the descending branch, both represented schematically by straight-line segments. x_0 and x_1 are given by Eqs. (2.11) and (2.27), respectively, and $x = a$ is the cylinder surface.

C. Local and Average Flux Density

We consider the magnetization for three stages: $0 < H \le H_{c1} + \Delta H$, $H_{c1} + \Delta H \le H \le H_{c1} + \Delta H + H_p$, and $H_{c1} + \Delta H + H_p \le H$.

For the first case ($0 < H \le H_{c1} + \Delta H$), the distribution of flux density in the sample is

$$B_i(x) \;=\; 0 \qquad (0 \le x \le a), \tag{2.13}$$

leading to the trivial result, $B(H) = 0$.

For the second case ($H_{c1} + \Delta H \le H \le H_{c1} + \Delta H + H_p$), H_{eff} is given as $H_{eff} = H - H_{c1} - \Delta H$ from Eq. (2.2). The distribution of local flux density in the sample is

$$B_i(x) \;=\; 0 \qquad (0 \le x \le x_0), \tag{2.14a}$$

$$B_i(x) \;=\; b_0(x) = \mu_0 H_{eff} + \mu_0 \int_x^a j_0(x')dx' \qquad (x_0 \le x \le a), \tag{2.14b}$$

where $b_0(x)$ is defined by $B_i(x)$ derived using $j_0(x)$. Substituting Eq. (2.10) into Eq. (2.14b), we obtain

$$b_0(x) \;=\; (p_0 x + q_0)^{1/2} - B_0, \tag{2.15}$$

where we used $-2\mu_0 k/p_0 = -1$ and $(p_0 a + q_0)^{1/2} = B_0 + \mu_0 H_{eff}$.

Using Eq. (2.4), the average flux density for this case is

$$\begin{aligned} B(H) &= \frac{2}{a^2}\int_{x_0}^a x b_0(x)dx \\ &= \frac{1}{15(\mu_0 ka)^2}[(3p_0 a - 2q_0)(p_0 a + q_0)^{3/2} - (3p_0 x_0 - 2q_0)(p_0 x_0 + q_0)^{3/2}] \\ &\quad - \frac{B_0}{a^2}(a^2 - x_0^2). \end{aligned} \tag{2.16}$$

Similarly, in the following discussion, we use $j_m(x)$ ($m = 0, 1, 2, \ldots, 9$) which corresponds to $J(x)$ in a specified region of x for each m. Thus, we assign $b_m(x)$ to local flux density $B_i(x)$ derived by substituting $j_m(x)$ into Eq. (2.11).

For simplicity, in the following discussion, we use $H_{eff}(n)$ ($n = 1, 2, 3, 4$) defined below.

$$H_{eff}(1) \;=\; H - H_{c1} - \Delta H, \tag{2.17a}$$

$$H_{eff}(2) \;=\; H - H_{c1} + \Delta H, \tag{2.17b}$$

$$H_{eff}(3) \;=\; H + H_{c1} + \Delta H, \tag{2.17c}$$

$$H_{eff}(4) \;=\; H + H_{c1} - \Delta H. \tag{2.17d}$$

In addition, we define $G_m(x)$ with p_m and q_m involved in $j_m(x)$ as;

$$G_m(x) = \frac{1}{15(\mu_0 ka)^2}(3p_m x - 2q_m)(p_m x + q_m)^{3/2}, \tag{2.18}$$

where

$$p_0 = p_3 = p_6 = p_7 = p_8 = p_9 = 2\mu_0 k, \tag{2.18a}$$

$$p_1 = p_2 = p_4 = p_5 = -2\mu_0 k, \tag{2.18b}$$

$$q_0 = q_6 = q_7 = q_8 = q_9 = [B_0 + \mu_0 H_{eff}(1)]^2 - 2\mu_0 ka, \tag{2.18c}$$

$$q_1 = [B_0 + \mu_0 H_{eff}(2)]^2 + 2\mu_0 ka, \tag{2.18d}$$

$$q_2 = 2B_0^2 - [B_0 - \mu_0 H_{eff}(3)]^2 + 2\mu_0 ka, \tag{2.18e}$$

$$q_3 = [B_0 - \mu_0 H_{eff}(3)]^2 - 2\mu_0 ka, \tag{2.18f}$$

$$q_4 = [B_0 - \mu_0 H_{eff}(4)]^2 + 2\mu_0 ka, \tag{2.18g}$$

$$q_5 = 2B_0^2 - [B_0 + \mu_0 H_{eff}(1)]^2 + 2\mu_0 ka. \tag{2.18h}$$

Using $G_0(x)$ defined by Eq. (2.18), Eq. (2.16) can be rewritten as

$$B(H) = G_0(a) - G_0(x_0) - \frac{B_0}{a^2}(a^2 - x_0^2). \tag{2.19}$$

For the third case ($H_{c1} + \Delta H + H_p \leq H$), $B(H)$ is given by Eq. (2.19) with $x_0 = 0$;

$$B(H) = G_0(a) - G_0(0) - B_0. \tag{2.20}$$

III. FULL-HYSTERESIS LOOPS

To obtain full-hysteresis loops, we consider a period of the applied field $H(\omega t) = H_{\rm dc} + H_{\rm ac}\cos(\omega t)$, where $H_{\rm dc} \geq 0$ and $H_{\rm ac} > 0$. Denoting the maximum and minimum values of H by H_A $(= H_{\rm dc} + H_{\rm ac})$ and H_B $(= H_{\rm dc} - H_{\rm ac})$, respectively, four types of hysteresis loops appear, depending on the magnitude of H_A.

The first case is for $0 < H_A \leq H_{c1} + \Delta H$, where no magnetic field penetrates into the specimen. The second case is for $H_{c1} + \Delta H \leq H_A \leq H_{c1} + \Delta H + H_p$ (low-H_A case), where the specimen is never fully penetrated. The third case is for $H_{c1} + \Delta H + H^* \leq H_A$ (high-H_A case), where the reverse supercurrent penetrates to the center of the specimen before H_{eff} is cycled back to zero. [We give H^* schematically in Fig. 2.1(b), and its expression is derived below.] The fourth case is intermediate, $H_{c1} + \Delta H + H_p \leq H_A \leq H_{c1} + \Delta H + H^*$ (medium-H_A case).

Full-hysteresis loops are derived by decreasing H from H_A to H_B, forming the descending branch of the loops. The ascending branch is then drawn by increasing H from H_B to H_A.

For the first case ($0 < H_A \leq H_{c1} + \Delta H$), full-hysteresis loops have 2 stages, ascending and descending. In both the stages, $B_i(x) = 0$, i.e., $B(H) = 0$.

The average flux density in other three cases are discussed below. Note that when a dc bias field $H_{\rm dc}$ has a nonzero value, each of these cases is further classified into several different cases, depending on the magnitude of H_B.

A. Hysteresis Loops for the Low-H_A Case

The low-H_A case is for $H_{c1} + \Delta H \leq H_A \leq H_{c1} + \Delta H + H_p$. In the initial magnetization process, $B(H)$ for $H = H_A$ is obtained from Eq. (2.19);

$$B(H_A) \;=\; G_{0A}(a) - G_{0A}(x_{0A}) - \frac{B_0}{a^2}(a^2 - x_{0A}^2), \tag{2.21}$$

where an additional subscript A on G_0 and x_0 indicates the function or variable at $H = H_A$. For example, from Eq. (2.11),

$$x_{0A} \;=\; a - \{[B_0 + \mu_0 H_{eff}(1_A)]^2 - B_0^2\}/2\mu_0 k. \tag{2.22}$$

(1) For $H_B \leq -H_{c1} - \Delta H$

According to Dunn and Hlawiczka [34], at the turning point of the applied field $H(|H| > H_{c1})$, the surface sheath current screens the specimen and causes the flux to be completely trapped as H decreases (or increases) over a range $2\Delta H$. This results inevitably in complete flux trapping for applied fields in the range $-H_{c1} \mp \Delta H \leq H \leq H_{c1} \mp \Delta H$ (minus; descending and plus; ascending).

Stage 1: $H_A - 2\Delta H \leq H \leq H_A$ (descending). In this stage, the flux is completely trapped. The supercurrent J (of negative sign) penetrates from the sample surface until $x = x_{0A}$ and the effective field H_{eff} in the region $x_{0A} \leq x \leq a$ is $H_{eff}(1_A)$. The corresponding $j_{0A}(x)$ is expressed by

$$\begin{aligned} j_{0A}(x) &= \frac{-k}{\{[B_0 + \mu_0 H_{eff}(1_A)]^2 - 2\mu_0 k(a-x)\}^{1/2}} \\ &= -k(p_{0A}x + q_{0A})^{-1/2}. \end{aligned} \tag{2.23}$$

The flux density $b_{0A}(x)$ in this region and $B(H)$ are

$$b_{0A}(x) = (p_{0A}x + q_{0A})^{1/2} - B_0, \tag{2.24}$$

$$\begin{aligned} B(H) &= \frac{2}{a^2}\int_{x_{0A}}^{a} x b_{0A}(x)dx \\ &= G_{0A}(a) - G_{0A}(x_{0A}) - \frac{B_0}{a^2}(a^2 - x_{0A}^2). \end{aligned} \tag{2.25}$$

Stage 2: $H_{c1} - \Delta H \leq H \leq H_A - 2\Delta H$ (descending). In this stage, the supercurrent J (of positive sign) penetrates from the sample surface until $x = x_1$ and the effective field H_{eff} in the region $x_1 \leq x \leq a$ is $H_{eff}(2)$. The corresponding $j_1(x)$ is expressed by

$$j_1(x) = \frac{k}{\{[B_0 + \mu_0 H_{eff}(2)]^2 + 2\mu_0 k(a-x)\}^{1/2}} \qquad (x_1 \leq x \leq a), \tag{2.26}$$

where we used the boundary condition $j_1(a) = J_c[\mu_0 H_{eff}(2)]$. Using the boundary condition at $x = x_1$, $j_1(x_1) = -j_{0A}(x_1)$, we obtain

$$x_1 = a - \{[B_0 + \mu_0 H_{eff}(1_A)]^2 - [B_0 + \mu_0 H_{eff}(2)]^2\}/4\mu_0 k. \tag{2.27}$$

Thus, the corresponding flux density $b_1(x)$ in the region $x_1 \leq x \leq a$ and $B(H)$ are

$$b_1(x) = (p_1 x + q_1)^{1/2} - B_0, \tag{2.28}$$

$$B(H) = \frac{2}{a^2}[\int_{x_{0A}}^{x_1} xb_{0A}(x)dx + \int_{x_1}^{a} xb_1(x)dx]$$
$$= [G_1(a) - G_1(x_1)] + [G_{0A}(x_1) - G_{0A}(x_{0A})] - \frac{B_0}{a^2}(a^2 - x_{0A}^2). \quad (2.29)$$

Stage 3: $-H_{c1} - \Delta H \leq H_A \leq H_{c1} - \Delta H$ (descending). In this stage, the flux is completely trapped. The supercurrent J (of positive sign) penetrates from the sample surface until $x = x_{1z}$ where the effective field H_{eff} is zero, and the corresponding $j_{1z}(x)$ is expressed by

$$j_{1z}(x) = \frac{k}{[B_0^2 + 2\mu_0 k(a-x)]^{1/2}} \qquad (x_{1z} \leq x \leq a). \quad (2.30)$$

An additional subscript z on $j_1(x)$ and x_1 indicates the specified value at $H_{eff} = 0$. We used the boundary condition $j_{1z}(a) = J_c(0)$. Using the boundary condition at $x = x_{1z}$, $j_{1z}(x_{1z}) = -j_{0A}(x_{1z})$, we obtain

$$x_{1z} = a - \{[B_0 + \mu_0 H_{eff}(1_A)]^2 - B_0^2\}/4\mu_0 k. \quad (2.31)$$

Thus, the corresponding flux density $b_{1z}(x)$ in the region $x_{1z} \leq x \leq a$ and $B(H)$ are

$$b_{1z}(x) = (p_{1z}x + q_{1z})^{1/2} - B_0, \quad (2.32)$$

$$B(H) = \frac{2}{a^2}[\int_{x_{0A}}^{x_{1z}} xb_{0A}(x)dx + \int_{x_{1z}}^{a} xb_{1z}(x)dx]$$
$$= [G_{1z}(a) - G_{1z}(x_{1z})] + [G_{0A}(x_{1z}) - G_{0A}(x_{0A})] - \frac{B_0}{a^2}(a^2 - x_{0A}^2). \quad (2.33)$$

Stage 4: $H_B \leq H \leq -H_{c1} - \Delta H$ (descending). For $H_{eff} = 0$, $j_1(x)$ takes its maximum value at $x = a$, $j_1(a) = k/B_0$. With decreasing H, x at which the supercurrent becomes maximum [i.e., equivalent to $B_i(x) = 0$] shifts inward until $x = x_3$. In this stage, the effective field H_{eff} is $H_{eff}(3)$ and the supercurrent denoted by $j_3(x)$ is

$$j_3(x) = \frac{k}{\{[B_0 - \mu_0 H_{eff}(3)]^2 - 2\mu_0 k(a-x)\}^{1/2}} \qquad (x_3 \leq x \leq a), \quad (2.34)$$

where we used the boundary condition $j_3(a) = J_c[\mu_0 H_{eff}(3)]$. From the boundary condition $j_3(x_3) = J_c(0)$, we find

$$x_3 = a - \{[B_0 - \mu_0 H_{eff}(3)]^2 - B_0^2\}/2\mu_0 k. \quad (2.35)$$

Assigning x_2 to the point $x = x_{1z}$ at which the supercurrent turns around, and expressing $J(x)$ in the region $x_2 \le x \le x_3$ by $j_2(x)$, we obtain

$$j_2(x) = \frac{k}{\{2B_0^2 - [B_0 - \mu_0 H_{eff}(3)]^2 + 2\mu_0 k(a-x)\}^{1/2}} \qquad (x_2 \le x \le x_3), \tag{2.36}$$

where we used $j_2(x_3) = j_3(x_3)$. From the boundary condition $j_2(x_2) = -j_{0A}(x_2)$, x_2 is given by

$$x_2 = a - \{[B_0 + \mu_0 H_{eff}(1_A)]^2 + [B_0 - \mu_0 H_{eff}(3)]^2 - 2B_0^2\}/4\mu_0 k. \tag{2.37}$$

Thus, we obtain $b_2(x)$, $b_3(x)$, and $B(H)$;

$$b_2(x) = (p_2 x + q_2)^{1/2} - B_0, \tag{2.38}$$

$$b_3(x) = -(p_3 x + q_3)^{1/2} + B_0, \tag{2.39}$$

$$\begin{aligned} B(H) = {} & -[G_3(a) - G_3(x_3)] + [G_2(x_3) - G_2(x_2)] + [G_{0A}(x_2) + G_{0A}(x_{0A})] \\ & + \frac{B_0^2}{a^2}(a^2 + x_{0A}^2 - 2x_3^2). \end{aligned} \tag{2.40}$$

In this stage, x_2 and x_3 for $H = H_B$ are obtained from Eqs. (2.37) and (2.35);

$$x_{2B} = a - \{[B_0 + \mu_0 H_{eff}(1_A)]^2 + [B_0 - \mu_0 H_{eff}(3_B)]^2 - 2B_0^2\}/4\mu_0 k, \tag{2.41}$$

$$x_{3B} = a - \{[B_0 - \mu_0 H_{eff}(3_B)]^2 - B_0^2\}/2\mu_0 k. \tag{2.42}$$

Similar to the subscript A, an additional subscript B indicates the specified variable or function at $H = H_B$.

Stage 5: $H_B \le H \le H_B + 2\Delta H$ (ascending). In this stage, the flux is completely trapped. The supercurrent J (of positive sign) penetrates from the sample surface until $x = x_{2B}$. The corresponding $j_{2B}(x)$ and $j_{3B}(x)$ are expressed by

$$j_{2B}(x) = \frac{k}{\{2B_0^2 - [B_0 - \mu_0 H_{eff}(3_B)]^2 + 2\mu_0 k(a-x)\}^{1/2}} \qquad (x_{2B} \le x \le x_{3B}), \tag{2.43}$$

$$j_{3B}(x) = \frac{k}{\{[B_0 - \mu_0 H_{eff}(3_B)]^2 - 2\mu_0 k(a-x)\}^{1/2}} \qquad (x_{3B} \le x \le a). \tag{2.44}$$

Thus, we obtain $b_{2B}(x)$, $b_{3B}(x)$, and $B(H)$;

$$b_{2B}(x) = (p_2 x + q_2)^{1/2} - B_0, \tag{2.45}$$

$$b_{3B}(x) = -(p_{3B} x + q_{3B})^{1/2} + B_0, \tag{2.46}$$

$$B(H) = -[G_{3B}(a) - G_{3B}(x_{3B})] + [G_{2B}(x_{3B}) - G_{2B}(x_{2B})] + [G_{0A}(x_{2B}) - G_{0A}(x_{0A})] + \frac{B_0}{a^2}(a^2 + x_{0A}^2 - 2x_{3B}^2). \tag{2.47}$$

Stage 6: $H_B + 2\Delta H \leq H \leq -H_{c1} + \Delta H$ (ascending). In this stage, the supercurrent J (of negative sign) circulates in the sample. Supposing the supercurrent penetrates until $x = x_4$, we find the effective field H_{eff} is given by $H_{eff}(4)$. Assigning $j_4(x)$ to $J(x)$ in the region $x_4 \leq x \leq a$, we obtain the following equations in a similar way.

$$j_4(x) = \frac{-k}{\{[B_0 - \mu_0 H_{eff}(4)]^2 + 2\mu_0 k(a-x)\}^{1/2}} \qquad (x_4 \leq x \leq a), \tag{2.48}$$

$$x_4 = a - \{[B_0 - \mu_0 H_{eff}(3_B)]^2 - [B_0 - \mu_0 H_{eff}(4)]^2\}/4\mu_0 k, \tag{2.49}$$

$$b_4(x) = -(p_4 x + q_4)^{1/2} + B_0, \tag{2.50}$$

$$B(H) = -[G_4(a) - G_4(x_4)] - [G_{3B}(x_4) - G_{3B}(x_{3B})] + [G_{2B}(x_{3B}) - G_{2B}(x_{2B})] + [G_{0A}(x_{2B}) - G_{0A}(x_{0A})] + \frac{B_0}{a^2}(a^2 + x_{0A}^2 - 2x_{3B}^2). \tag{2.51}$$

Stage 7: $-H_{c1} + \Delta H \leq H \leq H_{c1} + \Delta H$ (ascending). In this stage, the flux is completely trapped. The supercurrent J (of negative sign) penetrates from the sample surface until $x = x_{4z}$ and in this region the effective field H_{eff} is zero.

$$j_{4z}(x) = \frac{-k}{[B_0^2 + 2\mu_0 k(a-x)]^{1/2}} \qquad (x_{4z} \leq x \leq a), \tag{2.52}$$

$$x_{4z} = a - \{[B_0 - \mu_0 H_{eff}(3_B)]^2 - B_0^2\}/4\mu_0 k, \tag{2.53}$$

$$b_{4z}(x) = -(p_{4z} x + q_{4z})^{1/2} + B_0, \tag{2.54}$$

$$B(H) = -[G_{4z}(a) - G_{4z}(x_{4z})] - [G_{3B}(x_{4z}) - G_{3B}(x_{3B})] + [G_{2B}(x_{3B}) - G_{2B}(x_{2B})] + [G_{0A}(x_{2B}) - G_{0A}(x_{0A})] + \frac{B_0}{a^2}(a^2 + x_{0A}^2 - 2x_{3B}^2). \tag{2.55}$$

Stage 8: $H_{c1} + \Delta H \leq H \leq H_{c1} + \Delta H + H_C$ (ascending). For $H_{eff} = 0$, $j_4(x)$ takes its minimum value at $x = a$, $j_4(a) = -k/B_0$. With increasing H, x at which the supercurrent becomes minimum [i.e., equivalent to $B_i(x) = 0$] shifts inward until $x = x_6$. We assign $j_6(x)$ to $J(x)$ in the region $x_6 \leq x \leq a$. We also assign x_5 ($< x_6$) to the point at which $J(x)$ turns around from negative to positive, and in the region $x_5 \leq x \leq x_6$, we use $j_5(x)$. H_C is defined as $H_{eff}(1)$ for $x_5 = x_{3B}$. Since H_C is positive, we find $H_C = -H_B - H_{c1} - \Delta H$. Thus, by a similar treatment, we obtain

$$j_5(x) = \frac{-k}{\{2B_0^2 - [B_0 + \mu_0 H_{eff}(1)]^2 + 2\mu_0 k(a-x)\}^{1/2}} \qquad (x_5 \leq x \leq x_6), \tag{2.56}$$

$$x_5 = a - \{[B_0 + \mu_0 H_{eff}(1)]^2 + [B_0 - \mu_0 H_{eff}(3_B)]^2 - 2B_0^2\}/4\mu_0 k, \tag{2.57}$$

$$b_5(x) = -(p_5 x + q_5)^{1/2} + B_0, \tag{2.58}$$

$$j_6(x) = \frac{-k}{\{[B_0 + \mu_0 H_{eff}(1)]^2 - 2\mu_0 k(a-x)\}^{1/2}} \qquad (x_6 \leq x \leq a), \tag{2.59}$$

$$x_6 = a - \{[B_0 + \mu_0 H_{eff}(1)]^2 - B_0^2\}/2\mu_0 k, \tag{2.60}$$

$$\begin{aligned} B(H) = {} & [G_6(a) - G_6(x_6)] - [G_5(x_6) - G_5(x_5)] - [G_{3B}(x_5) - G_{3B}(x_{3B})] \\ & + [G_{2B}(x_{3B}) - G_{2B}(x_{2B})] + [G_{0A}(x_{2B}) - G_{0A}(x_{0A})] \\ & - \frac{B_0}{a^2}[a^2 - x_{0A}^2 + 2(x_{3B}^2 - x_6^2)]. \end{aligned} \tag{2.61}$$

Stage 9: $-H_B \leq H \leq H_A$ (ascending). Considering that the supercurrent changes its sign form negative to positive at a certain point, denoted by x_7, we define $J(x)$ in the region $x_7 \leq x \leq a$ as $j_7(x)$;

$$j_7(x) = \frac{-k}{\{[B_0 + \mu_0 H_{eff}(1)]^2 - 2\mu_0 k(a-x)\}^{1/2}} \qquad (x_7 \leq x \leq a), \tag{2.62}$$

$$x_7 = a - \{[B_0 + \mu_0 H_{eff}(1)]^2 + [B_0 - \mu_0 H_{eff}(3_B)]^2 - 2B_0^2\}/4\mu_0 k, \tag{2.63}$$

$$b_7(x) = (p_7 x + q_7)^{1/2} - B_0, \tag{2.64}$$

$$\begin{aligned} B(H) = {} & [G_7(a) - G_7(x_7)] + [G_{2B}(x_7) - G_{2B}(x_{2B})] + [G_{0A}(x_{2B}) - G_{0A}(x_{0A})] \\ & - \frac{B_0}{a^2}(a^2 - x_{0A}^2). \end{aligned} \tag{2.65}$$

(2) For $-H_{c1} - \Delta H \le H_B \le H_{c1} - \Delta H$

Stage 1: $H_A - 2\Delta H \le H \le H_A$ (descending). Same as Eq. (2.25).

Stage 2: $H_{c1} - \Delta H \le H \le H_A - 2\Delta H$ (descending). Same as Eq. (2.29).

Stage 3: $H_B \le H \le H_{c1} - \Delta H$ (descending). This stage is the same as stage 3 of Sec. III A (1) except for the interval of H. $B(H)$ is given by Eq. (2.33).

Stage 4: $H_B \le H \le H_{c1} + \Delta H$ (ascending). This stage is the same as stage 3 of Sec. III A (1) except for the interval of H. $B(H)$ is given by Eq. (2.33).

Stage 5: $H_{c1} + \Delta \le H \le H_A$ (ascending). In this stage, supposing that the supercurrent penetrates until $x = x_8$ with the increase of H, and assigning $j_8(x)$ to $J(x)$ in the region $x_8 \le x \le a$, we obtain

$$j_8(x) = \frac{-k}{\{[B_0 + \mu_0 H_{eff}(1)]^2 - 2\mu_0 k(a-x)\}^{1/2}} \qquad (x_8 \le x \le a), \tag{2.66}$$

$$x_8 = a - \{[B_0 + \mu_0 H_{eff}(1)]^2 - B_0^2\}/4\mu_0 k, \tag{2.67}$$

$$b_8(x) = (p_8 x + q_8)^{1/2} - B_0, \tag{2.68}$$

$$\begin{aligned} B(H) = {} & [G_8(a) - G_8(x_8)] + [G_{1z}(x_8) - G_{1z}(x_{1z})] + [G_{0A}(x_{1z}) - G_{0A}(x_{0A})] \\ & - \frac{B_0}{a^2}(a^2 - x_{0A}^2). \end{aligned} \tag{2.69}$$

(3) For $H_{c1} - \Delta H \le H_B$

Stage 1: $H_A - 2\Delta H \le H \le H_A$ (descending). Same as Eq. (2.25).

Stage 2: $H_B \le H \le H_A - 2\Delta H$ (descending). This stage is the same as stage 2 of Sec. III A (1) except for the interval of H. $B(H)$ is given by Eq. (2.29).

Stage 3: $H_B \le H \le H_B + 2\Delta H$ (ascending). In this stage, the flux is completely trapped. The supercurrent penetrates from the sample surface until $x = x_{1B}$ and in the region $x_{1B} \le x \le a$, the effective field H_{eff} is $H_{eff}(2_B)$. Assigning $j_{1B}(x)$ to $J(x)$ in this region, by a similar treatment, we obtain

$$j_{1B}(x) = \frac{k}{\{[B_0 + \mu_0 H_{eff}(2_B)]^2 + 2\mu_0 k(a-x)\}^{1/2}} \qquad (x_{1B} \le x \le a), \tag{2.70}$$

$$x_{1B} = a - \{[B_0 + \mu_0 H_{eff}(1_A)]^2 - [B_0 + \mu_0 H_{eff}(2_B)]^2\}/4\mu_0 k, \tag{2.71}$$

$$b_{1B}(x) = (p_{1B}x + q_{1B})^{1/2} - B_0, \tag{2.72}$$

$$B(H) = [G_{1B}(a) - G_{1B}(x_{1B})] + [G_{0A}(x_{1B}) - G_{0A}(x_{0A})] - \frac{B_0}{a^2}(a^2 - x_{0A}^2). \tag{2.73}$$

Stage 4: $H_B + 2\Delta H \leq H \leq H_A$ (ascending). In this stage, supposing that the supercurrent penetrates until $x = x_9$ with the increase of H, the effective field H_{eff} in the region $x_9 \leq x \leq a$ is given by $H_{eff}(1)$. Assigning $j_9(x)$ to $J(x)$ in this region, we obtain

$$j_9(x) = \frac{-k}{\{[B_0 + \mu_0 H_{eff}(1)]^2 - 2\mu_0 k(a-x)\}^{1/2}} \qquad (x_9 \leq x \leq a), \tag{2.74}$$

$$x_9 = a - \{[B_0 + \mu_0 H_{eff}(1)]^2 - [B_0 + \mu_0 H_{eff}(2_B)]^2\}/4\mu_0 k, \tag{2.75}$$

$$b_9(x) = (p_9 x + q_9)^{1/2} - B_0, \tag{2.76}$$

$$B(H) = [G_9(a) - G_9(x_9)] + [G_{1B}(x_9) - G_{1B}(x_{1B})] + [G_{0A}(x_{1B}) - G_{0A}(x_{0A})] + \frac{B_0}{a^2}(a^2 - x_{0A}^2). \tag{2.77}$$

B. Hysteresis Loops for the Medium-H_A Case

The medium-H_A case is for $H_{c1} + \Delta H + H_p \leq H_A \leq H_{c1} + \Delta H + H^*$. In this case, there are five cases depending on the magnitude of H_B. To avoid repetition, we give only the final $B(H)$ equations derived by a similar process as described above.

(1) For $H_B \leq -H_{c1} - \Delta H - H_p$

Stage 1: $H_A - 2\Delta H \leq H \leq H_A$ (descending).

$$B(H) = G_{0A}(a) - G_{0A}(x_{0A}) - B_0. \tag{2.78}$$

This equation is the same as Eq. (2.25) with $x_{0A} = 0$. Since $x_1 \doteq 0$ for $H_{eff} = 0$, H^* is expressed as

$$H^* = [(B_0^2 + 4\mu_0 ka)^{1/2} - B_0]/\mu_0. \tag{2.79}$$

Stage 2: $H_{c1} - \Delta H \leq H \leq H_A - 2\Delta H$ (descending).

$$B(H) = [G_1(a) - G_1(x_1)] + [G_{0A}(x_1) - G_{0A}(x_{0A})] - B_0. \tag{2.80}$$

Stage 3: $-H_{c1} - \Delta H \leq H \leq H_A - 2\Delta H$ (descending).

$$B(H) = [G_{1z}(a) - G_{1z}(x_{1z})] + [G_{0A}(x_{1z}) - G_{0A}(x_{0A})] - B_0. \tag{2.81}$$

Stage 4: $-H_{c1} - \Delta H + H_{prm}^- \leq H \leq -H_{c1} - \Delta H$ (descending). H_{prm}^- is the reverse full-penetration field (on the descending branch) for the medium-H_A case, which is represented schematically in Fig. 2.2(a). H_{prm}^- can be determined by taking $x_2 = 0$ in Eq. (2.37);

$$H_{prm}^- = B_0/\mu_0 - \{4\mu_0 ka + 2B_0^2 - [B_0 + \mu_0 H_{eff}(1_A)]^2\}^{1/2}/\mu_0, \tag{2.82}$$

$$\begin{aligned} B(H) = & -[G_3(a) - G_3(x_3)] + [G_2(x_3) - G_2(x_2)] + [G_{0A}(x_2) - G_{0A}(x_{0A})] \\ & + \frac{B_0}{a^2}(a^2 - 2x_3^2). \end{aligned} \tag{2.83}$$

Stage 5: $-H_{c1} - \Delta H - H_p \leq H \leq -H_{c1} - \Delta H + H_{prm}^-$ (descending).

$$B(H) = -[G_3(a) - G_3(x_3)] + [G_2(x_3) - G_2(0)] + \frac{B_0}{a^2}(a^2 - 2x_3^2). \tag{2.84}$$

Stage 6: $H_B \leq H \leq -H_{c1} - \Delta H - H_p$ (descending).

$$B(H) = -[G_3(a) - G_3(0)] + B_0. \tag{2.85}$$

Stage 7: $H_B \leq H \leq H_B + 2\Delta H$ (ascending).

$$B(H) = -[G_{3B}(a) - G_{3B}(0)] + B_0. \tag{2.86}$$

Stage 8: $H_B + 2\Delta H \leq H \leq -H_{c1} + \Delta H$ (ascending).

$$B(H) = -[G_4(a) - G_4(x_4)] - [G_{3B}(x_4) - G_{3B}(0)] + B_0. \tag{2.87}$$

Stage 9: $-H_{c1} + \Delta H \leq H \leq H_{c1} + \Delta H$ (ascending).

$$B(H) = -[G_{4z}(a) - G_{4z}(x_{4z})] - [G_{3B}(x_{4z}) - G_{3B}(0)] + B_0. \tag{2.88}$$

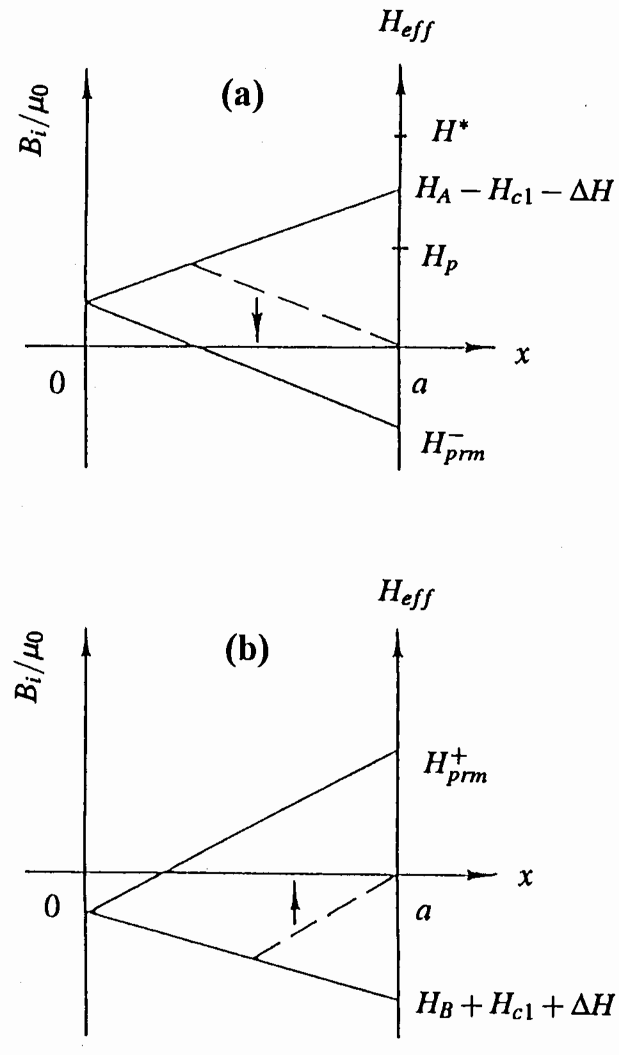

FIG. 2.2. Schematic representations of the reverse full-penetration fields (a) H_{prm}^- in the descending branch where H_{eff} is $H_{eff}(3)$ defined by Eq. (2.17d), and (b) H_{prm}^+ in the ascending branch where H_{eff} is $H_{eff}(1)$ defined by Eq. (2.17b). H_A and H_B are the maximum and minimum values of H, respectively.

Stage 10: $H_{c1}+\Delta H \leq H \leq H_{c1}+\Delta H+H^{+}_{prm}$ (ascending). H^{+}_{prm} is the reverse full-penetration field (on the ascending branch) for the medium-H_A case which is represented schematically in Fig. 2.2(b). H^{+}_{prm} can be determined by taking $x_5=0$ in Eq. (2.57);

$$H^{+}_{prm} = \{4\mu_0 ka+2B_0^2-[B_0-\mu_0 H_{eff}(3_B)]^2\}^{1/2}/\mu_0-B_0/\mu_0, \tag{2.89}$$

$$\begin{aligned} B(H) &= [G_6(a)-G_6(x_6)]-[G_5(x_6)-G_5(x_5)]-[G_{3B}(x_5)-G_{3B}(0)] \\ &\quad -\frac{B_0}{a^2}(a^2-2x_6^2). \end{aligned} \tag{2.90}$$

Stage 11: $H_{c1}+\Delta H+H^{+}_{prm} \leq H \leq H_{c1}+\Delta H+H_p$ (ascending).

$$B(H) = [G_6(a)-G_6(x_6)]-[G_5(x_6)-G_5(0)]-\frac{B_0}{a^2}(a^2-2x_6^2). \tag{2.91}$$

Stage 12: $H_{c1}+\Delta H+H_p \leq H \leq H_A$ (ascending).

$$B(H) = [G_6(a)-G_6(0)]-B_0. \tag{2.92}$$

(2) For $-H_{c1}-\Delta H-H_p \leq H_B \leq -H_{c1}-\Delta H+H^{-}_{prm}$

Stage 1: $H_A-2\Delta H \leq H \leq H_A$ (descending). Same as Eq. (2.78).

Stage 2: $H_{c1}-\Delta H \leq H \leq H_A-2\Delta H$ (descending). Same as Eq. (2.80).

Stage 3: $-H_{c1}-\Delta H \leq H \leq H_{c1}-\Delta H$ (descending). Same as Eq. (2.81).

Stage 4: $-H_{c1}-\Delta H+H^{-}_{prm}$ (descending). Same as Eq. (2.83).

Stage 5: $H_B \leq H \leq -H_{c1}-\Delta H+H^{-}_{prm}$ (descending). This stage is the same as stage 5 of Sec. III B (1) except for the interval of H. $B(H)$ is given by Eq. (2.84).

Stage 6: $H_B \leq H \leq H_B+2\Delta H$ (ascending).

$$B(H) = -[G_{3B}(a)-G_{3B}(x_{3B})]+[G_{2B}(x_{3B})-G_{2B}(0)]+\frac{B_0}{a^2}(a^2-2x_{3B}^2). \tag{2.93}$$

Stage 7: $H_B+2\Delta H \leq H \leq -H_{c1}+\Delta H$ (ascending).

$$\begin{aligned} B(H) &= -[G_4(a)-G_4(x_4)]-[G_{3B}(x_4)-G_{3B}(x_{3B})]+[G_{2B}(x_{3B})-G_{2B}(0)] \\ &\quad +\frac{B_0}{a^2}(a^2-2x_{3B}^2). \end{aligned} \tag{2.94}$$

Stage 8: $-H_{c1}+\Delta H \le H \le H_{c1}+\Delta H$ (ascending).

$$\begin{aligned} B(H) &= -[G_{4z}(a)-G_{4z}(x_{4z})]-[G_{3B}(x_{4z})-G_{3B}(x_{3B})]+[G_{2B}(x_{3B})-G_{2B}(0)] \\ &\quad +\frac{B_0}{a^2}(a^2-2x_{3B}^2). \end{aligned} \tag{2.95}$$

Stage 9: $H_{c1}+\Delta H \le H \le -H_B$ (ascending)

$$\begin{aligned} B(H) &= [G_6(a)-G_6(x_6)]-[G_5(x_6)-G_5(x_5)]-[G_{3B}(x_5)-G_{3B}(x_{3B})] \\ &\quad +[G_{2B}(x_{3B})-G_{2B}(0)]-\frac{B_0}{a^2}(a^2+2x_{3B}^2-2x_6^2). \end{aligned} \tag{2.96}$$

Stage 10: $-H_B \le H \le H_{c1}+\Delta H+H_{prm}^{+}$ (ascending).

$$B(H) = [G_7(a)-G_7(x_7)]+[G_{2B}(x_7)-G_{2B}(0)]-B_0. \tag{2.97}$$

Stage 11: $H_{c1}+\Delta H+H_{prm}^{+} \le H \le H_A$. This stage is the same as stage 12 of Sec. III B (1) except for the interval of H. $B(H)$ is given by Eq. (2.92).

(3) For $-H_{c1}-\Delta H+H_{prm}^{-} \le H_B \le -H_{c1}-\Delta H$

Stage 1: $H_A-2\Delta H \le H \le H_A$ (descending). Same as Eq. (2.78).

Stage 2: $H_{c1}-\Delta H \le H \le H_A-2\Delta H$ (descending). Same as Eq. (2.80).

Stage 3: $-H_{c1}-\Delta H \le H \le H_{c1}-\Delta H$ (descending). Same as Eq. (2.81).

Stage 4: $H_B \le H \le -H_{c1}-\Delta H$ (descending). This stage is the same as stage 4 of Sec. III B (1) except for the interval of H. $B(H)$ is given by Eq. (2.83).

Stage 5: $H_B \le H \le H_B+2\Delta H$ (ascending).

$$\begin{aligned} B(H) &= -[G_{3B}(a)-G_{3B}(x_{3B})]+[G_{2B}(x_{3B})-G_{2B}(x_{2B})]+[G_{0A}(x_{2B})-G_{0A}(0)] \\ &\quad +\frac{B_0}{a^2}(a^2-2x_{3B}^2). \end{aligned} \tag{2.98}$$

Stage 6: $H_B+2\Delta H \le H \le -H_{c1}+\Delta H$ (ascending).

$$\begin{aligned} B(H) &= -[G_4(a)-G_4(x_4)]-[G_{3B}(x_4)-G_{3B}(x_{3B})]+[G_{2B}(x_{3B})-G_{2B}(x_{2B})] \\ &\quad +[G_{0A}(x_{2B})-G_{0A}(0)]+\frac{B_0}{a^2}(a^2-2x_{3B}^2). \end{aligned} \tag{2.99}$$

Stage 7: $-H_{c1}+\Delta H \le H \le H_{c1}+\Delta H$ (ascending).

$$\begin{aligned} B(H) &= -[G_{4z}(a)-G_{4z}(x_{4z})]-[G_{3B}(x_{4z})-G_{3B}(x_{3B})]+[G_{2B}(x_{3B})-G_{2B}(x_{2B})] \\ &\quad +[G_{0A}(x_{2B})-G_{0A}(0)]+\frac{B_0}{a^2}(a^2-2x_{3B}^2). \end{aligned} \tag{2.100}$$

Stage 8: $H_{c1}+\Delta H \le H \le -H_B$ (ascending).

$$\begin{aligned} B(H) &= [G_6(a)-G_6(x_6)]-[G_5(x_6)-G_5(x_5)]-[G_{3B}(x_5)-G_{3B}(x_{3B})] \\ &\quad +[G_{2B}(x_{3B})-G_{2B}(x_{2B})]+[G_{0A}(x_{2B})-G_{0A}(0)] \\ &\quad -\frac{B_0}{a^2}(a^2+2x_{3B}^2-2x_6^2). \end{aligned} \tag{2.101}$$

Stage 9: $-H_B \le H \le H_A$ (ascending).

$$\begin{aligned} B(H) &= [G_7(a)-G_7(x_7)]+[G_{2B}(x_7)-G_{2B}(x_{2B})]+[G_{0A}(x_{2B})-G_{0A}(0)] \\ &\quad -B_0. \end{aligned} \tag{2.102}$$

(4) For $-H_{c1}-\Delta H \le H_B \le H_{c1}-\Delta H$

Stage 1: $H_A-2\Delta H \le H \le H_A$ (descending). Same as Eq. (2.78).

Stage 2: $H_{c1}-\Delta H \le H \le H_A-2\Delta H$ (descending). Same as Eq. (2.80).

Stage 3: $H_B \le H \le H_{c1}-\Delta H$ (descending). This stage is the same as stage 3 of Sec. III B (1) except the interval of H. $B(H)$ is given by Eq. (2.81).

Stage 4: $H_B \le H \le H_{c1}+\Delta H$ (ascending). This stage is the same as stage 3 of Sec. III B (1) except for the interval of H. $B(H)$ is given by Eq. (2.83).

Stage 5: $H_{c1}+\Delta H \le H \le H_A$ (ascending).

$$\begin{aligned} B(H) &= [G_8(a)-G_8(x_8)]+[G_{1z}(x_8)-G_{1z}(x_{1z})]+[G_{0A}(x_{1z})-G_{0A}(0)] \\ &\quad -B_0. \end{aligned} \tag{2.103}$$

(5) For $H_{c1} - \Delta H \leq H_B \leq H_A$

Stage 1: $H_A - 2\Delta H \leq H \leq H_A$ (descending). Same as Eq. (2.78).

Stage 2: $H_B \leq H \leq H_A - 2\Delta H$ (descending). This stage is the same as stage 2 of Sec. III B (1) except for the interval of H. $B(H)$ is given by Eq. (2.80).

Stage 3: $H_B \leq H \leq H_B + 2\Delta H$ (ascending).

$$B(H) = [G_{1B}(a) - G_{1B}(x_{1B})] + [G_{0A}(x_{1B}) - G_{0A}(0)] - B_0. \tag{2.104}$$

Stage 4: $H_B + 2\Delta H \leq H \leq H_A$ (ascending).

$$B(H) = [G_9(a) - G_9(x_9)] + [G_{1B}(x_9) - G_{1B}(x_{1B})] + [G_{0A}(x_{1B}) - G_{0A}(0)] - B_0. \tag{2.105}$$

C. Hysteresis Loops for the High-H_A Case

The high-H_A case is for $H_{c1} + \Delta H + H^* \leq H_A$. In this case, there are six cases depending on the magnitude of H_B. Only the final $B(H)$ equations are given.

(1) For $H_B \leq -H_{c1} - \Delta H - H^*$

Stage 1: $H_A - 2\Delta H \leq H \leq H_A$ (descending). Same as Eq. (2.78).

Stage 2: $H_{c1} - \Delta H + H_{prh}^- \leq H \leq H_A - 2\Delta H$ (descending). H_{prh}^- is the reverse full-penetration field (on the descending branch) for the high-H_A case, which is represented schematically in Fig. 2.3(a). H_{prh}^- can be determined by taking $x_1 = 0$ in Eq. (2.27);

$$H_{prh}^- = \{[B_0 + \mu_0 H_{eff}(1_A)]^2 - 4\mu_0 ka\}^{1/2}/\mu_0 - B_0/\mu_0. \tag{2.106}$$

This stage is the same as stage 2 of Sec. III B (1) except for the interval of H. $B(H)$ is given by Eq. (2.80).

Stage 3: $H_{c1} - \Delta H \leq H \leq H_{c1} - \Delta H + H_{prh}^-$ (descending).

$$B(H) = [G_1(a) - G_1(0)] - B_0. \tag{2.107}$$

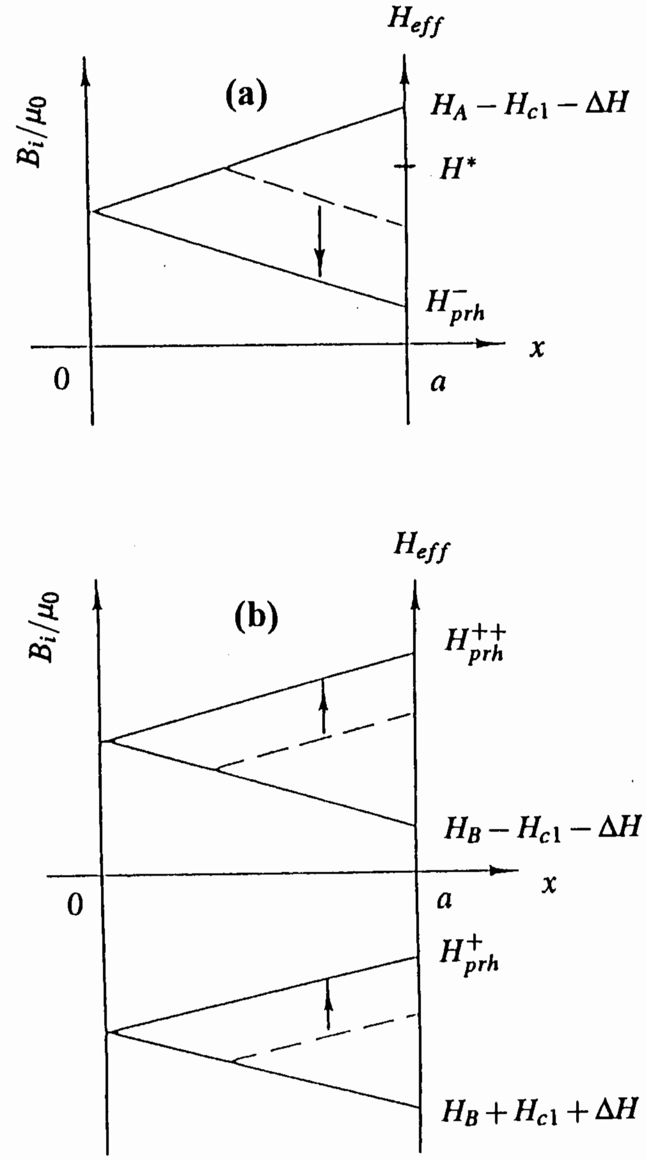

FIG. 2.3. Schematic representations of the reverse full-penetration fields (a) H_{prh}^- in the descending branch where H_{eff} is $H_{eff}(2)$ defined by Eq. (2.17c), and (b) H_{prh}^+ in the ascending branch where H_{eff} is $H_{eff}(4)$ defined by Eq. (2.17d) and H_{prh}^{++} in the ascending branch where H_{eff} is $H_{eff}(1)$ defined by Eq. (2.17b). When H_{eff} is equal to either H_{prh}^- or H_{prh}^+ or H_{prh}^{++}, $B_i(x)$ never crosses over the x axis.

Stage 4: $-H_{c1}-\Delta H \leq H \leq H_{c1}-\Delta H$ (descending).

$$B(H) = [G_{1z}(a)-G_{1z}(0)]-B_0. \tag{2.108}$$

Stage 5: $-H_{c1}-\Delta H-H_p \leq H \leq -H_{c1}-\Delta H$ (descending). This stage is the same as stage 5 of Sec. III B (1) except for the interval of H. $B(H)$ is given by Eq. (2.84).

Stage 6: $H_B \leq H \leq -H_{c1}-\Delta H-H_p$ (descending). Same as Eq. (2.85).

Stage 7: $H_B \leq H \leq H_B+2\Delta H$ (ascending). Same as Eq. (2.86).

Stage 8: $H_B+2\Delta H \leq H \leq -H_{c1}+\Delta H+H^{+}_{prh}$. H^{+}_{prh} is the reverse full-penetration field (on the ascending branch) for the high-H_A case, which is represented schematically in Fig. 2.3(b). H^{+}_{prh} can be determined by taking $x_4=0$ in Eq. (2.49);

$$H^{+}_{prh} = B_0/\mu_0-\{[B_0-\mu_0 H_{eff}(3_B)]^2-4\mu_0 ka\}^{1/2}/\mu_0. \tag{2.109}$$

This stage is the same as stage 8 of Sec. III B (1) except for the interval of H. $B(H)$ is given by Eq. (2.87).

Stage 9: $-H_{c1}+\Delta H+H^{+}_{prh} \leq H \leq -H_{c1}+\Delta H$ (ascending).

$$B(H) = -[G_4(a)-G_4(0)]-B_0. \tag{2.110}$$

Stage 10: $-H_{c1}+\Delta H \leq H \leq H_{c1}+\Delta H$ (ascending).

$$B(H) = -[G_{4z}(a)-G_{4z}(0)]-B_0. \tag{2.111}$$

Stage 11: $H_{c1}+\Delta H \leq H \leq H_{c1}+\Delta H+H_p$ (ascending). This stage is the same as stage 11 of Sec. III B (1) except for the interval of H. $B(H)$ is given by Eq. (2.91).

Stage 12: $H_{c1}+\Delta H+H_p \leq H \leq H_A$ (ascending). Same as Eq. (2.92).

(2) For $-H_{c1}-\Delta H-H^{*} \leq H_B \leq -H_{c1}-\Delta H-H_p$

Stage 1: $H_A-2\Delta H \leq H \leq H_A$ (ascending). Same as Eq. (2.78).

Stage 2: $H_{c1}-\Delta H+H^{-}_{prh} \leq H \leq H_A-2\Delta H$ (descending). This stage is the same as stage 2 of Sec. III B (1) except for the interval of H. $B(H)$ is given by Eq. (2.80).

Stage 3: $H_{c1}-\Delta H \leq H \leq H_{c1}-\Delta H+H^{-}_{prh}$ (descending). Same as Eq. (2.107).

Stage 4: $-H_{c1} - \Delta H \le H \le H_{c1} - \Delta H$ (descending). Same as Eq. (2.108).

Stage 5: $-H_{c1} - \Delta H - H_p \le H \le -H_{c1} - \Delta H$ (descending). This stage is the same as stage 5 of Sec. III B (1) except for the interval of H. $B(H)$ is given by Eq. (2.84).

Stage 6: $H_B \le H \le -H_{c1} - \Delta H - H_p$ (descending). Same as Eq. (2.85).

Stage 7: $H_B \le h \le H_B + 2\Delta H$ (ascending). Same as Eq. (2.86).

Stage 8: $H_B + 2\Delta H \le H \le -H_{c1} + \Delta H$ (ascending). Same as Eq. (2.87).

Stage 9: $-H_{c1} + \Delta H \le H \le H_{c1} + \Delta H$ (ascending). Same as Eq. (2.88).

Stage 10: $H_{c1} + \Delta H \le H \le H_{c1} + \Delta H + H_{prm}^{+}$ (ascending). Same as Eq. (2.90).

Stage 11: $H_{c1} + \Delta H \le H \le H_{c1} + \Delta H + H_p$ (ascending). Same as Eq. (2.91).

Stage 12: $H_{c1} + \Delta H + H_p \le H \le H_A$ (ascending). Same as Eq. (2.92).

(3) For $-H_{c1} - \Delta H - H_p \le H_B \le -H_{c1} - \Delta H$

Stage 1: $H_A - 2\Delta H \le H \le H_A$ (ascending). Same as Eq. (2.78).

Stage 2: $H_{c1} - \Delta H + H_{prh}^{-} \le H \le H_A - 2\Delta H$ (descending). This stage is the same as stage 2 of Sec. III B (1) except for the interval of H. $B(H)$ is given by Eq. (2.80).

Stage 3: $H_{c1} - \Delta H \le H \le H_{c1} - \Delta H + H_{prh}^{-}$ (descending). Same as Eq. (2.107).

Stage 4: $-H_{c1} - \Delta H \le H \le H_{c1} - \Delta H$ (descending). Same as Eq. (2.108).

Stage 5: $H_B \le H \le -H_{c1} - \Delta H$ (descending). This stage is the same as stage 5 of Sec. III B (1) except for the interval of H. $B(H)$ is given by Eq. (2.84).

Stage 6: $H_B \le H \le H_B + 2\Delta H$ (ascending). Same as Eq. (2.93).

Stage 7: $H_B + 2\Delta H \le H \le -H_{c1} + \Delta H$ (ascending). Same as Eq. (2.94).

Stage 8: $-H_{c1} + \Delta H \le H \le H_{c1} + \Delta H$ (ascending). Same as Eq. (2.95).

Stage 9: $H_{c1} + \Delta H \le H \le -H_B$ (ascending). Same as Eq. (2.96).

Stage 10: $-H_B \le H \le H_{c1} + \Delta H + H_{prm}^{+}$ (ascending). Same as Eq. (2.97).

Stage 11: $H_{c1} + \Delta H + H_{prm}^{+} \le H \le H_A$ (ascending). This stage is the same as stage 12 of Sec. III B (1) except for the interval of H. $B(H)$ is given by Eq. (2.92).

(4) For $-H_{c1} - \Delta H \leq H_B \leq H_{c1} - \Delta H$

Stage 1: $H_A - 2\Delta H \leq H \leq H_A$ (ascending). Same as Eq. (2.78).

Stage 2: $H_{c1} - \Delta H + H_{prh}^{-} \leq H \leq H_A - 2\Delta H$ (descending). This stage is the same as stage 2 of Sec. III B (1) except for the interval of H. $B(H)$ is given by Eq. (2.80).

Stage 3: $H_{c1} - \Delta H \leq H \leq H_{c1} - \Delta H + H_{prh}^{-}$ (descending). Same as Eq. (2.107).

Stage 4: $H_B \leq H \leq H_{c1} - \Delta H$ (descending). This stage is the same as stage 4 of Sec. III C (1) except for the interval of H. $B(H)$ is given by Eq. (2.108).

Stage 5: $H_B \leq H \leq H_{c1} + \Delta H$ (ascending). This stage is the same as stage 4 of Sec. III C (1) except for the interval of H. $B(H)$ is given by Eq. (2.108).

Stage 6: $H_{c1} + \Delta H \leq H \leq H_{c1} + \Delta H + H^{*}$ (ascending).

$$B(H) = [G_8(a) - G_8(x_8)] + [G_{1z}(x_8) - G_{1z}(0)] - B_0. \tag{2.112}$$

Stage 7: $H_{c1} + \Delta H \leq H \leq H_{c1} + \Delta H + H^{*}$ (ascending). This stage is the same as stage 12 of Sec. III B (1) except for the interval of H. $B(H)$ is given by Eq. (2.92).

(5) For $H_{c1} - \Delta H \leq H_B \leq H_{c1} + \Delta H + H_{prh}^{-}$

Stage 1: $H_A - 2\Delta H \leq H \leq H_A$ (descending). Same as Eq. (2.78).

Stage 2: $H_{c1} - \Delta H + H_{prh}^{-} \leq H \leq H_A - 2\Delta H$ (descending). This stage is the same as stage 2 of Sec. III B (1) except for the interval of H. $B(H)$ is given by Eq. (2.80).

Stage 3: $H_B \leq H \leq H_{c1} - \Delta H + H_{prh}^{-}$ (descending). This stage is the same as stage 6 of Sec. III C (1) except for the interval of H. $B(H)$ is given by Eq. (2.107).

Stage 4: $H_B \leq H \leq H_B + 2\Delta H$ (ascending).

$$B(H) = [G_{1B}(a) - G_{1B}(0)] - B_0. \tag{2.113}$$

Stage 5: $H_B + 2\Delta H \leq H \leq H_{c1} + \Delta H + H_{prh}^{++}$ (ascending). H_{prh}^{++} is the reverse full-penetration field (on the ascending branch) for the high-H_A, which is represented schematically in Fig. 2.3(b). H_{prh}^{++} can be determined by taking $x_9 = 0$ in Eq. (2.75).

$$H_{prh}^{++} = \{[B_0 + \mu_0 H_{eff}(2_B)]^2 + 4\mu_0 ka\}^{1/2}/\mu_0 - B_0/\mu_0, \tag{2.114}$$

$$B(H) = [G_9(a) - G_9(x_9)] + [G_{1B}(x_9) - G_{1B}(0)] - B_0. \tag{2.115}$$

Stage 6: $H_{c1} + \Delta H + H_{prh}^{++} \leq H \leq H_A$ (ascending). This stage is the same as stage 12 of Sec. III B (1) except for the interval of H. $B(H)$ is given by Eq. (2.92).

(6) For $H_{c1} - \Delta H + H_{prh}^{++} \leq H_B \leq H_A$

Stage 1: $H_A - 2\Delta H \leq H \leq H_A$ (descending). Same as Eq. (2.78).

Stage 2: $H_B \leq H \leq H_A - 2\Delta H$ (descending). This stage is the same as stage 2 of Sec. III B (1) except for the interval of H. $B(H)$ is given by Eq. (2.80).

Stage 3: $H_B \leq H \leq H_B + 2\Delta H$ (ascending). Same as Eq. (2.104).

Stage 4: $H_B + 2\Delta H \leq H \leq H_A$ (ascending). Same as Eq. (2.105).

IV. COMPUTED MAGNETIZATION CURVES

We have analytically tested, for each case in Sec. III, that all the stages are continuous at their end points.. In this section, we give some computed $M(H)$ curves. To reduce the number of variables, we use a parameter, similar to one used by Kim, Hempstead, and Strnad [18] and Chen and Goldfarb [20];

$$p = (2\mu_0 ka)^{1/2}/B_0. \tag{2.116}$$

The parameter p defined by Eq. (2.116) is a convenient quantity for characterization of a sample. When the material parameter B_0 is relatively large ($B_0 \gg B_i$), the initial magnetic flux density B_i in Eq. (2.1) can be practically neglected against B_0, and J_c given by Eq. (2.1) is expected to be a constant. In other words, a sample with a small value of p can be asymptotically treated in the framework of the Bean model. On the contrary, for an extremely large value of p ($B_0 \ll B_i$), J_c sensitively varies depending on B_i.

With this parameter, Eqs. (2.12) and (2.79) can be rewritten as

$$H_p = B_0[(1+p^2)^{1/2} - 1]/\mu_0, \tag{2.117}$$

$$H^* = B_0[(1+2p^2)^{1/2} - 1]/\mu_0. \tag{2.118}$$

Using the $B(H)$ equations in Eq. (2.5), we can draw the computed $M(H)$ curves under any experimental condition of applied fields. To carry out the evaluation, one period of the alternating magnetic field $H(\omega t)$ ($0 \leq \omega t \leq 2\pi$) was divided into 360 regular intervals, and $M(\omega t)$ was numerically obtained at each point.

Figures 2.4 – 2.12 give the initial and hysteresis $M(H)$ curves for three different dc bias field $H_{dc} = 0$, H_p, and $4H_p$; and for each H_{dc}, three different values of $p = 0.3$, 3, and 1000; and for each p, four different sets (a) $\Delta H = 0$, $H_{c1} = 0$, (b) $\Delta H = 0.1H_p$, $H_{c1} = 0$, (c) $\Delta H = 0$, $H_{c1} = 0.15H_p$, and (d) $\Delta H = 0.1H_p$, $H_{c1} = 0.15H_p$. For each case, three $M(H)$ loops are drawn for $H_{ac} = H_p/2$, $(H^* + H_p)/2$, and $4H_p$. For all the loops, M and H are normalized to H_p.

From Figs. 2.4 – 2.12, we note the following aspects:

(1) As seen in the uppermost figures (a) of Figs. 2.4 – 2.12, the $M(H)$ loops for $\Delta H = H_{c1} = 0$ correspond to those presented in Figs. 4 – 6 of Ref. 28, proving the validity of the present derivations.

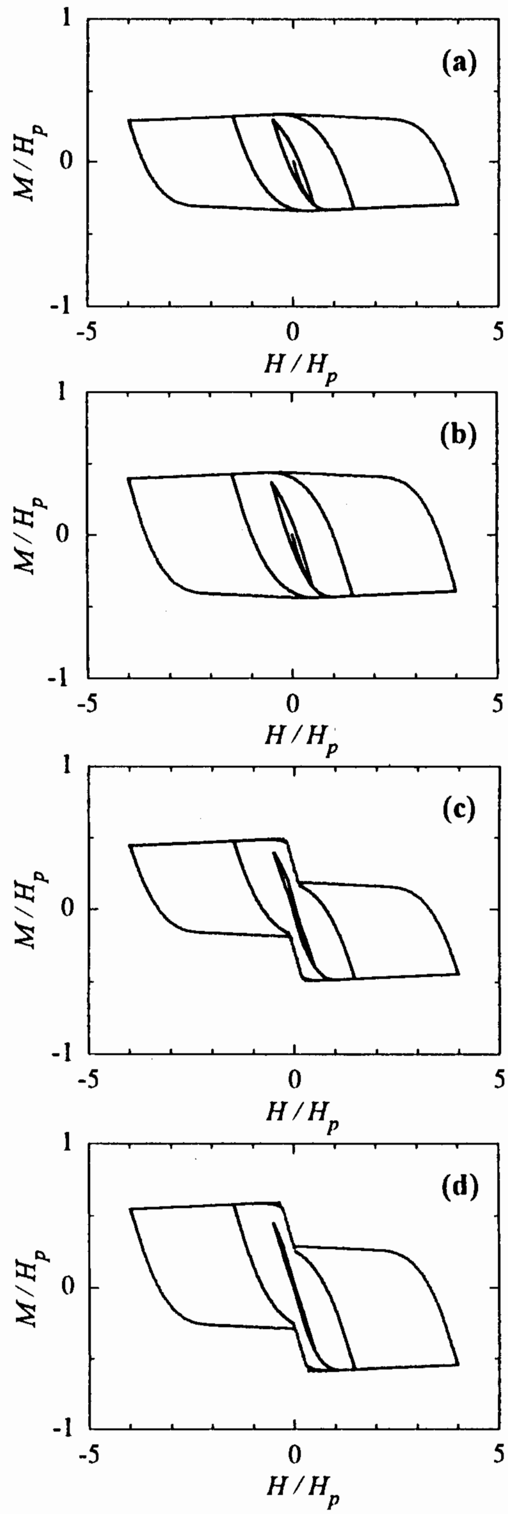

FIG. 2.4. Theoretical $M(H)$ curves, scaled by H_p, for $H_{dc} = 0$ and $p = 0.3$; (a) $\Delta H = 0, H_{c1} = 0$, (b) $\Delta H = 0.1H_p, H_{c1} = 0$, (c) $\Delta H = 0, H_{c1} = 0.15H_p$, and (d) $\Delta H = 0.1H_p$, $H_{c1} = 0.15H_p$. In each figure, loops are shown for $H_{ac} = H_p/2$ (smallest), $(H^* + H_p)/2$, and $4H_p$ (largest).

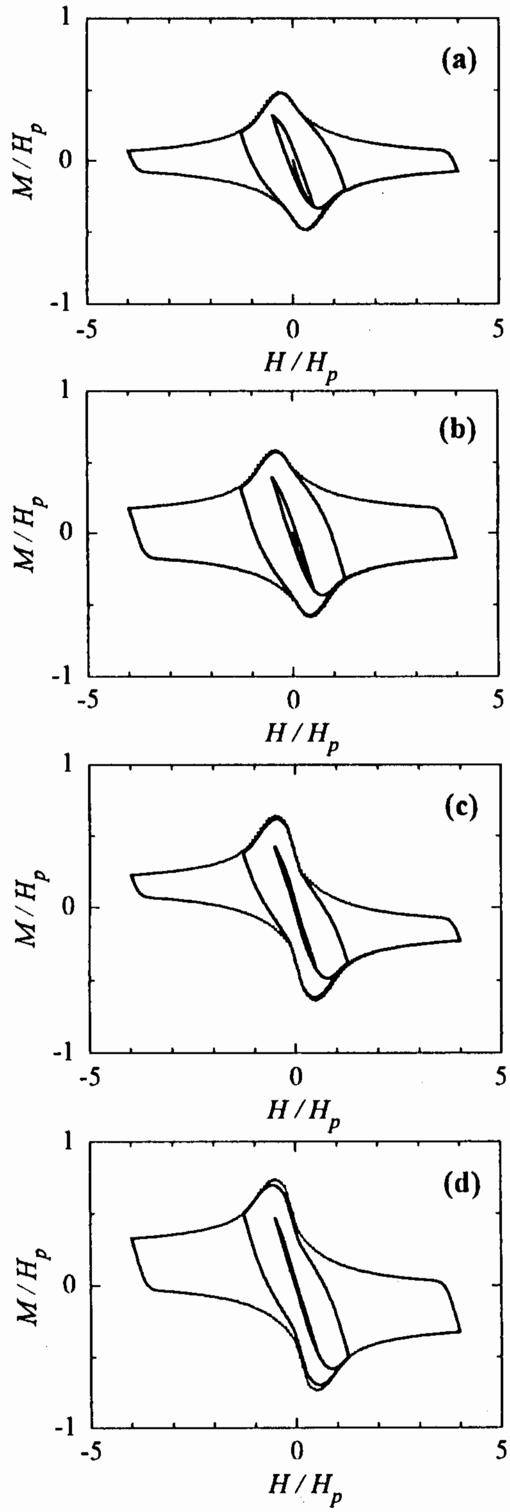

FIG. 2.5. Theoretical $M(H)$ curves, scaled by H_p, for $H_{dc} = 0$ and $p = 3$; (a) $\Delta H = 0$, $H_{c1} = 0$, (b) $\Delta H = 0.1H_p$, $H_{c1} = 0$, (c) $\Delta H = 0$, $H_{c1} = 0.15H_p$, and (d) $\Delta H = 0.1H_p$, $H_{c1} = 0.15H_p$. In each figure, loops are shown for $H_{ac} = H_p/2$ (smallest), $(H^* + H_p)/2$, and $4H_p$ (largest).

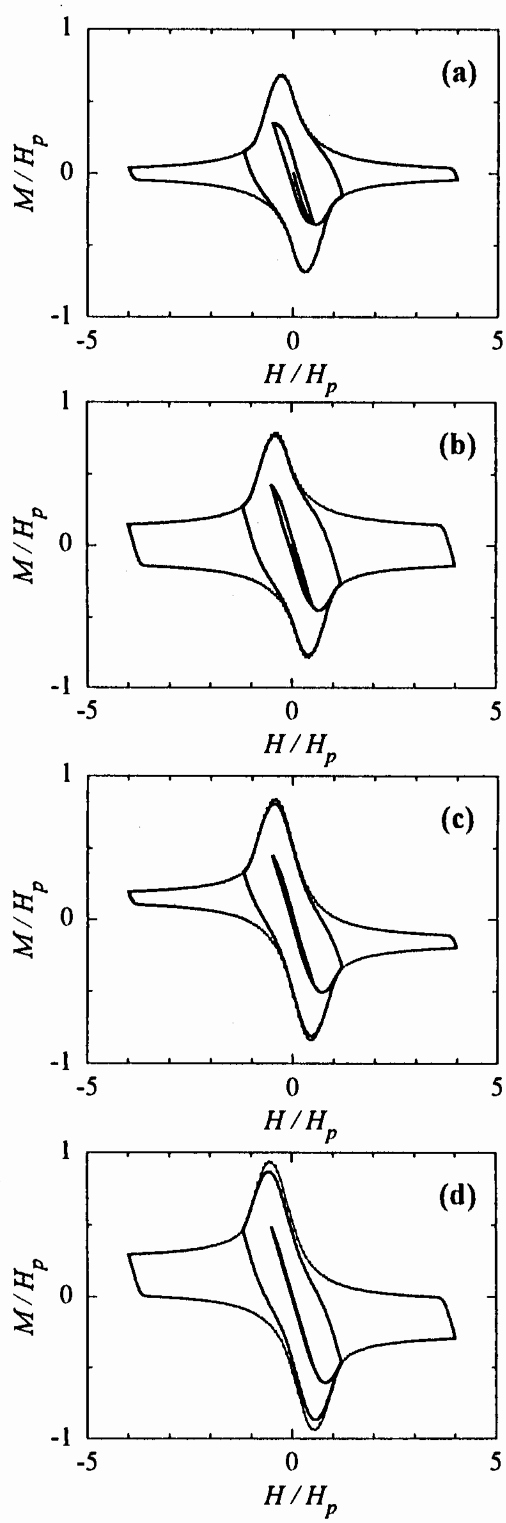

FIG. 2.6. Theoretical $M(H)$ curves, scaled by H_p, $H_{dc} = 0$ and $p = 1000$; (a) $\Delta H = 0$, $H_{c1} = 0$, (b) $\Delta H = 0.1H_p$, $H_{c1} = 0$, (c) $\Delta H = 0$, $H_{c1} = 0.15H_p$, and (d) $\Delta H = 0.1H_p$, $H_{c1} = 0.15H_p$. In each figure, loops are shown for $H_{ac} = H_p/2$ (smallest), $(H^* + H_p)/2$, and $4H_p$ (largest).

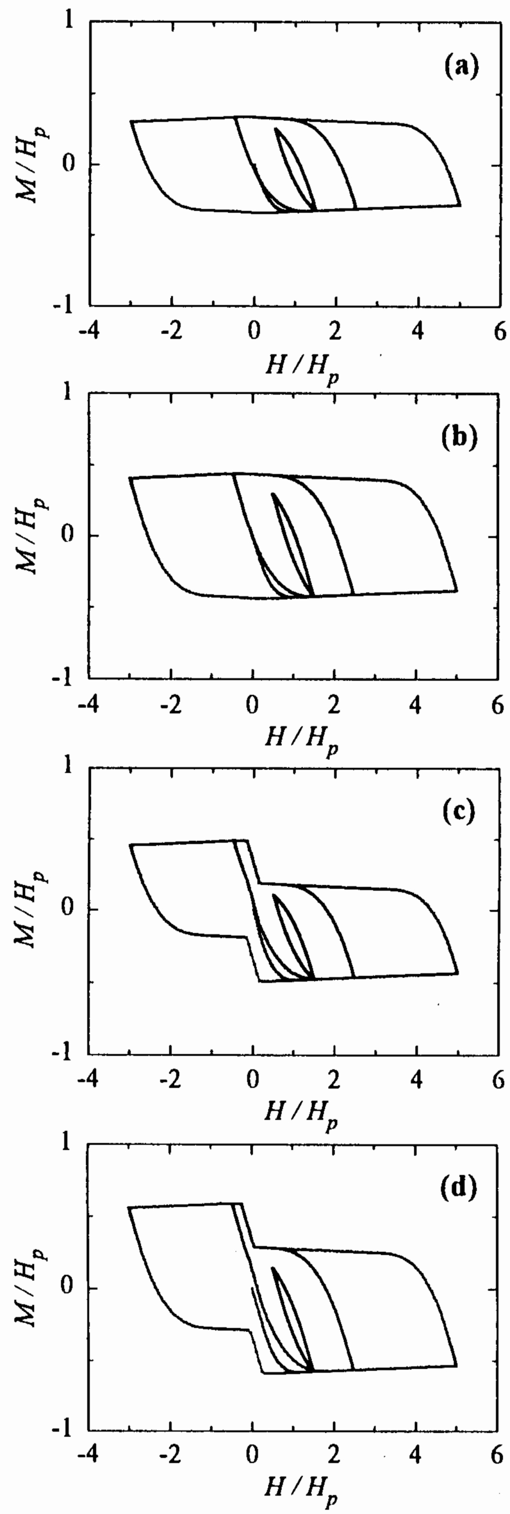

FIG. 2.7. Theoretical $M(H)$ curves, scaled by H_p, for $H_{dc} = H_p$ and $p = 0.3$; (a) $\Delta H = 0, H_{c1} = 0$, (b) $\Delta H = 0.1H_p, H_{c1} = 0$, (c) $\Delta H = 0, H_{c1} = 0.15H_p$, and (d) $\Delta H = 0.1H_p$, $H_{c1} = 0.15H_p$. In each figure, loops are shown for $H_{ac} = H_p/2$ (smallest), $(H^* + H_p)/2$, and $4H_p$ (largest).

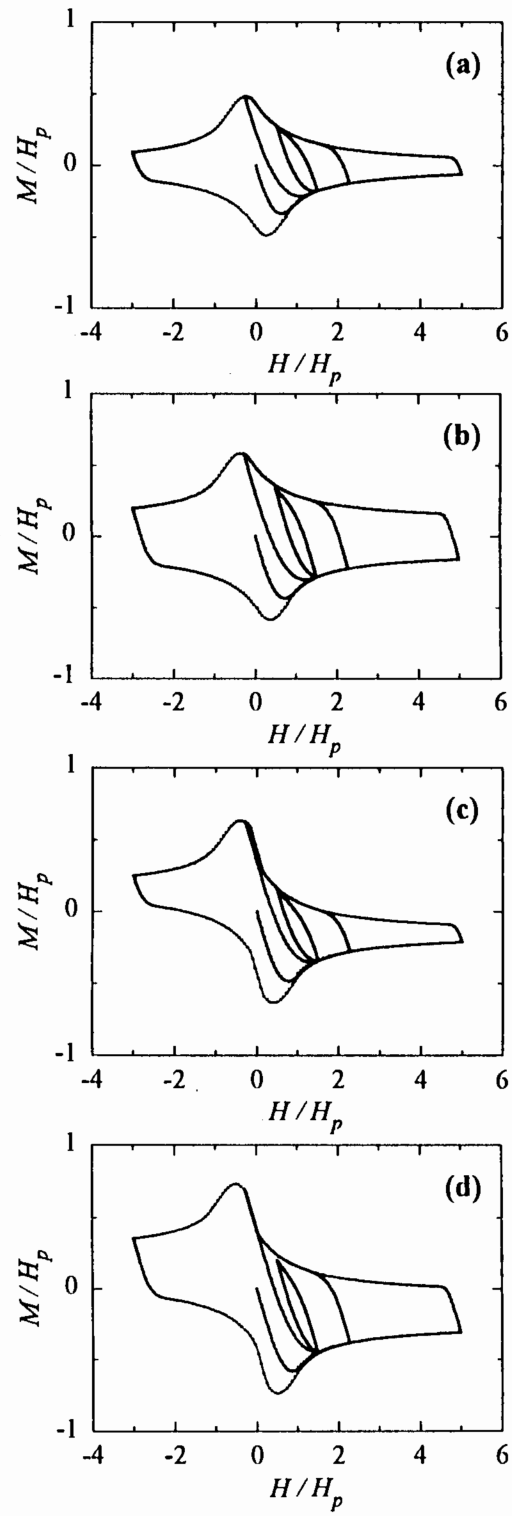

FIG. 2.8. Theoretical $M(H)$ curves, scaled by H_p, for $H_{dc} = H_p$ and $p = 3$; (a) $\Delta H = 0, H_{c1} = 0$, (b) $\Delta H = 0.1H_p$, $H_{c1} = 0$, (c) $\Delta H = 0$, $H_{c1} = 0.15H_p$, and (d) $\Delta H = 0.1H_p$, $H_{c1} = 0.15H_p$. In each figure, loops are shown for $H_{ac} = H_p/2$ (smallest), $(H^* + H_p)/2$, and $4H_p$ (largest).

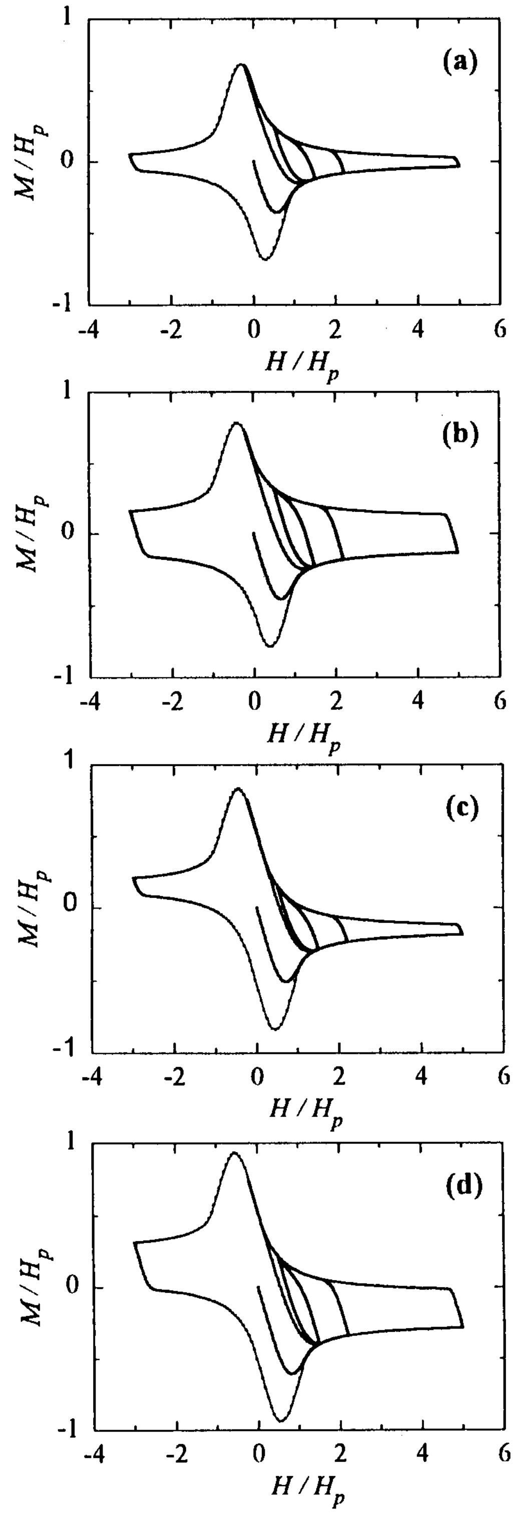

FIG. 2.9. Theoretical $M(H)$ curves, scaled by H_p, for $H_{dc} = H_p$ and $p = 1000$; (a) $\Delta H = 0$, $H_{c1} = 0$, (b) $\Delta H = 0.1H_p$, $H_{c1} = 0$, (c) $\Delta H = 0$, $H_{c1} = 0.15H_p$, and (d) $\Delta H = 0.1H_p$, $H_{c1} = 0.15H_p$. In each figure, loops are shown for $H_{ac} = H_p/2$ (smallest), $(H^* + H_p)/2$, and $4H_p$ (largest).

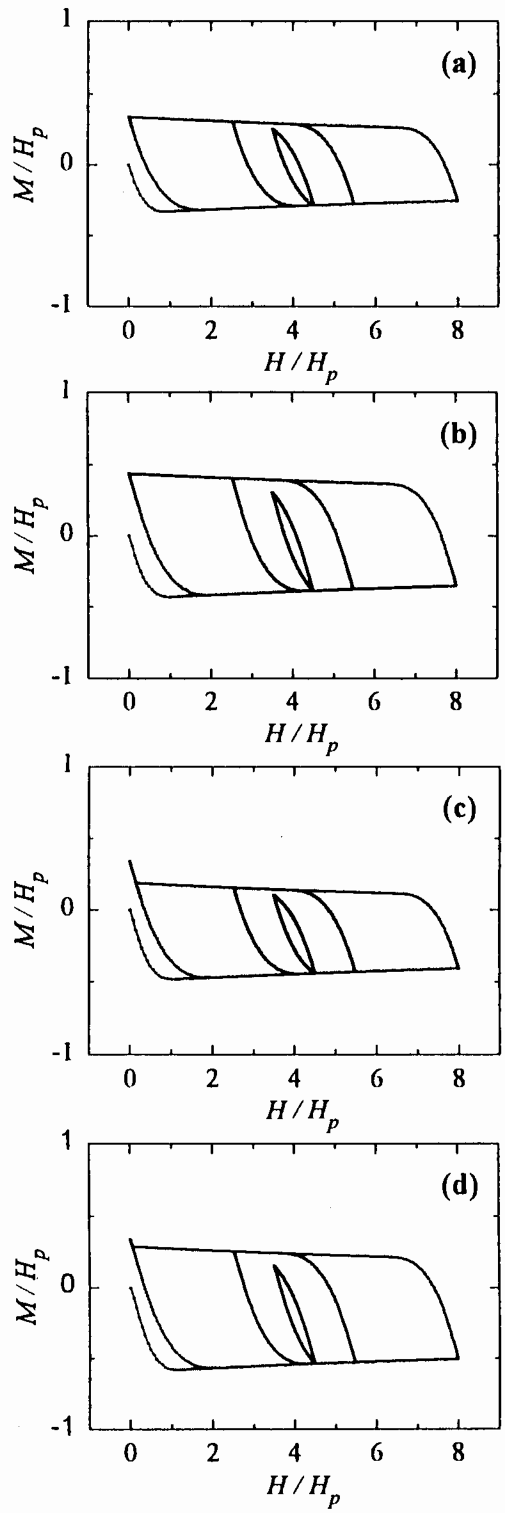

FIG. 2.10. Theoretical $M(H)$ curves, scaled by H_p, for $H_{dc} = 4H_p$ and $p = 0.3$; (a) $\Delta H = 0$, $H_{c1} = 0$, (b) $\Delta H = 0.1H_p$, $H_{c1} = 0$, (c) $\Delta H = 0$, $H_{c1} = 0.15H_p$, and (d) $\Delta H = 0.1H_p$, $H_{c1} = 0.15H_p$. In each figure, loops are shown for $H_{ac} = H_p/2$ (smallest), $(H^* + H_p)/2$, and $4H_p$ (largest).

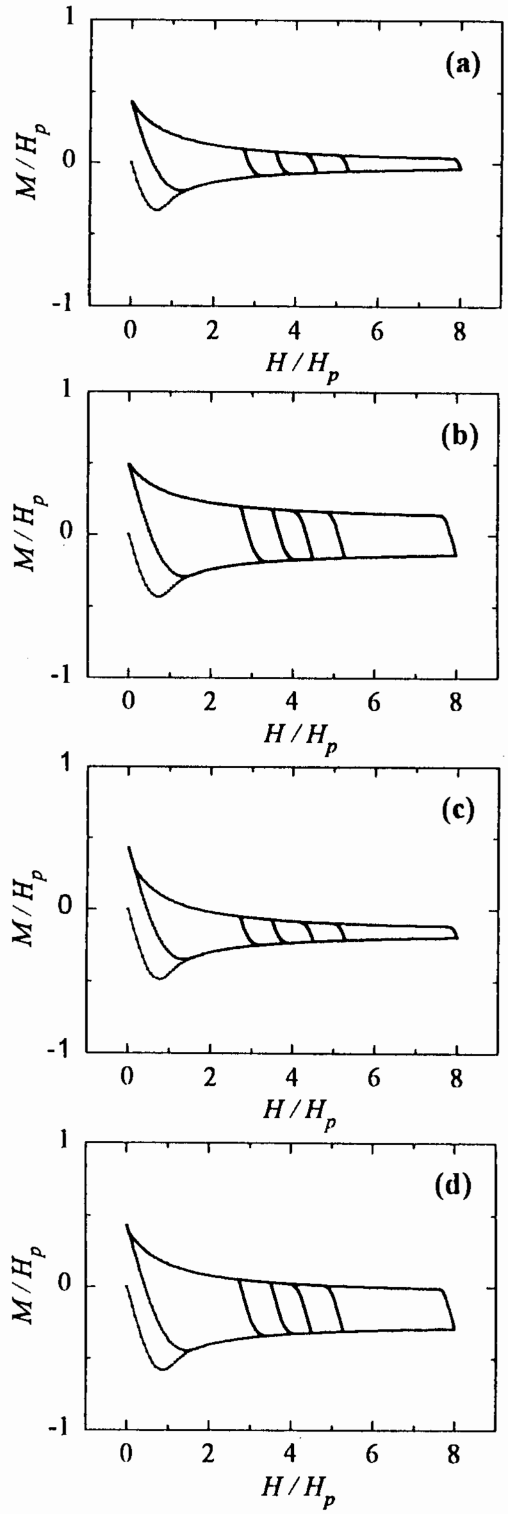

FIG. 2.11. Theoretical $M(H)$ curves, scaled by H_p, for $H_{dc} = 4H_p$ and $p = 3$; (a) $\Delta H = 0, H_{c1} = 0$, (b) $\Delta H = 0.1H_p$, $H_{c1} = 0$, (c) $\Delta H = 0, H_{c1} = 0.15H_p$, and (d) $\Delta H = 0.1H_p$, $H_{c1} = 0.15H_p$. In each figure, loops are shown for $H_{ac} = H_p/2$ (smallest), $(H^* + H_p)/2$, and $4H_p$ (largest).

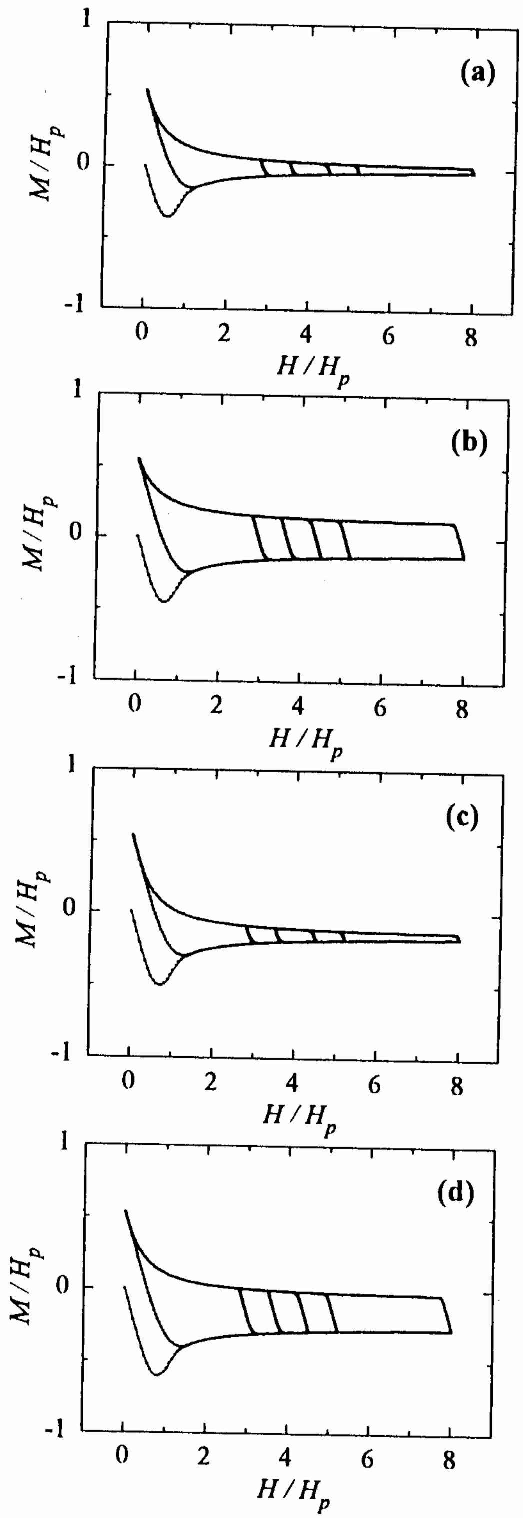

FIG. 2.12. Theoretical $M(H)$ curves, scaled by H_p, for $H_{dc} = 4H_p$ and $p = 1000$; (a) $\Delta H = 0$, $H_{c1} = 0$, (b) $\Delta H = 0.1H_p$, $H_{c1} = 0$, (c) $\Delta H = 0$, $H_{c1} = 0.15H_p$, and (d) $\Delta H = 0.1H_p$, $H_{c1} = 0.15H_p$. In each figure, loops are shown for $H_{ac} = H_p/2$ (smallest), $(H^* + H_p)/2$, and $4H_p$ (largest).

(2) When $\Delta H \neq 0$, the $M(H)$ loops are expanded up and down with the increase of ΔH, but as far as $H_{c1} = 0$ [second figures (b) of Figs. 2.4 – 2.12], the profiles are essentially the same as those of the uppermost figures (a) of Figs. 2.4 – 2.12. This indicates that the effect of ΔH is not easy to see from an individual measurement of the $M(H)$ curves. However, more detailed examination of the curves may reveal the effect of a nonzero value of ΔH. For example, we compare Fig. 2.4(a) ($\Delta H = 0$) and Fig. 2.4(b) ($\Delta H = 0.1H_p$), of which the expanded figures are given in Fig. 2.13. As seen in Fig. 2.13(a), the $M(H)$ curve reversed at $H/H_p = 4$ does not trace the Meissner slope given by a straight-line segment, but draws a curve. On the contrary, in Fig. 2.13(b), the $M(H)$ curve reversed at $H/H_p = 4$ traces well the Meissner slope until $2\Delta H/H_p = 0.2$ and then begins to draw a curve, suggesting that the $M(H)$ profile around the reversed point could be a probe for the surface barrier.

(3) When $H_{c1} \neq 0$, the $M(H)$ loops change the shape drastically. Typically, as seen in Figs. 2.4(c) and (d), for $p = 0.3$ (asymptotically correspond to the Bean model) and $H_{\mathrm{dc}} = 0$, the loops show a sharp step-like feature. It should be noticed that the step width indicated in the figures correctly corresponds to $2H_{c1}$. As seen in Figs. 2.5 and 2.6, the step becomes dull as p increases. Such a step-like feature also occurs for $H_{\mathrm{dc}} = H_p$ [(c) and (d) of Figs. 2.7 – 2.9], but when H_{dc} becomes larger, it tends to disappear even for a nonzero value of H_{c1} [see (c) and (d) of Figs. 2.10 – 2.12].

(4) For a small value of p ($= 0.3$), the $M(H)$ loops are almost symmetrical for any H_{dc}, as far as $H_{c1} = 0$ [see (a) and (b) of Figs. 2.4 – 2.12]. This means that by the Bean model, we cannot produce the asymmetric nature without taking account of the lower critical field. On the contrary, when p becomes larger, the asymmetric nature of the $M(H)$ loops can be brought out by a nonzero value of H_{dc}. This indicates that H_{dc} introduces the asymmetric nature into the $M(H)$ loops only when $B_0 \ll B_i$, i.e., when J_c depends explicitly on the internal magnetic flux density B_i [see, for example, Figs. 2.9(a) and (b)].

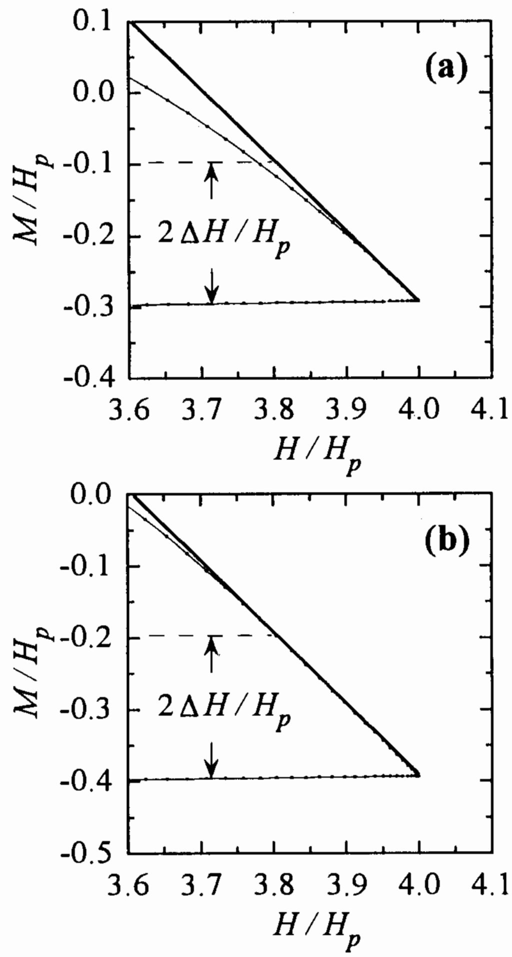

FIG. 2.13. Expanded figures of (a) Fig. 2.4(a) (for $\Delta H = 0$) and (b) Fig. 2.4(b) (for $2\Delta H/H_p = 0.2$). Straight-line segments indicate the Meissner slope.

V. CONCLUSIONS

We have investigated theoretically the effect of surface barriers ΔH and lower critical fields H_{c1} on the magnetization of type-II superconductors. Derivations of the magnetization equations were made within the construct of the modified KA model, in which the effective field H_{eff} involving ΔH and H_{c1} was used for evaluations of the magnetic-flux density in the sample.

We consider an infinitely long cylindrical specimen with the external field applied along the cylinder axis. To obtain full-hysteresis loops, we treat a period of the applied field $H(\omega t) = H_{\rm dc} + H_{\rm ac}\cos(\omega t)$, where $H_{\rm dc} \geq 0$ and $H_{\rm ac} > 0$. Denoting the maximum and minimum values of H by H_A $(= H_{\rm dc} + H_{\rm ac})$ and H_B $(= H_{\rm dc} - H_{\rm ac})$, respectively, four types of hysteresis loops appear, depending on the magnitude of H_A. Among these, three types are further classified into several cases, depending on the magnitude of H_B. To complete the descending and ascending branches of the loops for all the cases, it needs to consider 113 stages of H and all the magnetization equations have been thoroughly derived.

To test our derivations, the equations were confirmed to be continuous at their end points. Further examination of the derivations was made by comparing the equations at the limit $\Delta H \longrightarrow 0$ and $H_{c1} \longrightarrow 0$ with those previously reported for $\Delta H = H_{c1} = 0$ [28].

The hysteresis $M(H)$ curves calculated using the appropriate magnetization equations for various experimental conditions of applied fields have revealed that the roles of ΔH and H_{c1} are implicated with each other, but are distinctive. ΔH does not essentially cause an explicit deformation to the $M(H)$ curves, but merely expands them up and down, while H_{c1} introduces a drastic change in the $M(H)$ profiles, i.e., a step-like feature appears in the $M(H)$ curves and the step width precisely corresponds to $2H_{c1}$.

Present derivations fully cover practical experimental conditions and would be useful for analyses of the magnetic behavior of type-II superconductors.

Chapter 3

Lower Critical Fields of $Bi_2Sr_2CaCu_2O_{8+\delta}$ and $YBa_2Cu_3O_{7-\delta}$ Single Crystals

I. INTRODUCTION

As one of the key quantities of cuprate-based oxide superconductors, the lower critical field H_{c1} has been studied by employing a variety of methods [58–76]. However, in the measurement of H_{c1}, other effects (demagnetization, volume flux pinning, surface barriers etc.) would be involved, and probably for that reason, the results of H_{c1} are still conflicting.

Of particular interest is the temperature dependence of H_{c1}. Some groups have reported a BCS-like saturation in the low temperature region below the critical temperature, while some others observed an anomalous upturn in $H_{c1}(T)$ as temperature decreases. For example, using an electron spin resonance spectrometer, Rettori *et al.* [58] found an anomalous upturn in $H_{c1}(T)$ for polycrystalline $YBa_2Cu_3O_{7-\delta}$ (Y123) in the low temperature region. Their conclusion is that the localized d holes give rise to the signals due to electron spin resonance at low temperatures. From dc-magnetization measurements of single-crystal Y123, for both orientations of the applied field, parallel and perpendicular to the c axis, Adrian *et al.* [63] found a remarkable enhancement of $H_{c1}(T)$ at temperatures below 40 K. To understand this anomalous temperature dependence of H_{c1}, Koyama *et al.* [69] used a model of multilayer structure which is composed of arrays of superconducting and normal layers, and suggested that superconductivity in the normal layers is induced by a proximity effect [77], resulting in the enhancement of H_{c1}.

Meanwhile, Naito *et al.* [66] determined H_{c1} from a procedure based on the Bean critical-state model to pick up the onset of flux penetration in zero-field-cooled magnetization curves in $La_{2-x}Sr_xCuO_4$ single crystals. They found an apparent anisotropic temperature dependence of H_{c1}, but the anomalous upturn in $H_{c1}(T)$ was not observed. Burlachkov *et al.* [73] proposed that the anomalous upturn in $H_{c1}(T)$ can be interpreted by invoking surface barriers which cause retardation in flux pinning, and concluded that this anomaly is an artifact of an inappropriate modeling of the irreversible behavior. Recently, Nideröst *et al.* [76] determined the penetration field of $Bi_2Sr_2CaCu_2O_{8+\delta}$ (Bi2212) crystals from magnetization curves for different sweep rates dH/dt and temperatures. In this work, they found saturated values of the penetration field which they interpreted as the true lower critical field, but any anomalous upturn of $H_{c1}(T)$ was not observed down to about 10 K.

Adopting the fields for first vortex entry and last vortex exit, Chen *et al.* [74] determined H_{c1}

in the presence of surface barriers, where they used a grain-aligned sintered Y123 and analyzed the data using an extended critical-state model. They found a BCS temperature dependence of H_{c1} above 50 K, but below that temperature an enhancement of H_{c1} was observed. Their conclusion is that the anomalous upturn in H_{c1} may be intrinsic and it would be attributed to an increase in the Ginzburg–Landau (GL) parameter κ at low temperatures. Zheng *et al.* [75] studied the anisotropic superconducting properties of the magnetically aligned Y123 powders with low levels of Co and Zn doping. From ac susceptibility, dc magnetization, and critical-current density measurements, the anisotropic nature of the samples was discussed in detail, but their observations did not show any anomalous upturn of $H_{c1}(T)$.

As described in Chap. 2, we have fully derived the magnetization equations of type-II superconductors (an infinite cylindrical specimen) within the framework of the modified Kim–Anderson (KA) critical-state model [27], where H_{c1} and surface barriers ΔH are explicitly taken into consideration. From the calculated initial magnetization curves and full-hysteresis loops, we found that $M(H)$ curves are merely expanded up and down with the increase of ΔH, while H_{c1} introduces a step-like feature into the hysteresis loop. In particular, it has been revealed that this step width correctly corresponds to $2H_{c1}$ without involving surface barriers.

Based on this theoretical prediction, we measured the $M(H)$ curves of Bi2212 and Y123 single crystals, and attempted to determine the temperature dependence of H_{c1} for both orientations of the applied field, parallel and perpendicular to the c axis. We found that the temperature dependence of H_{c1} for the applied field perpendicular to the c axis, $H_{c1,ab}(T)$, of Bi2212 had an anomalous upturn in the low temperature region (below about 40 K), while $H_{c1,ab}(T)$ of Y123 showed no anomalous upturn. For the field parallel to the c axis, $H_{c1,c}(T)$ of Bi2212 also showed a weak anomalous upturn, but $H_{c1,c}(T)$ of Y123 did not show any anomaly down to the lowest temperature used in the present study.

In this chapter, we present details of the measurement of $H_{c1}(T)$ and analyses of the results by the modified KA model.

II. TYPICAL PROFILES OF THEORETICAL $M(H)$ CURVES

In the theoretical treatment in Chap. 2, we used an infinite long cylindrical specimen of radius a immersed in an alternating magnetic field superimposed on a dc field, $H(\omega t) = H_{dc} + H_{ac}\cos(\omega t)$, where $H_{dc} \geq 0$ and $H_{ac} > 0$. However, it is reasonable to apply the theory to a practical fractional bulk superconductor by correcting for the demagnetization effect. Besides, to reduce the number of variables in calculations of $M(H)$ curves, we used a parameter p defined as $p = (2\mu_0 ka)^{1/2}/B_0$, where k and B_0 are the material parameters used in the modified KA model. This parameter p is, as mentioned before, a convenient quantity for characterization of a sample. When the material parameter B_0 is relatively large ($B_0 \gg B_i$), the local magnetic flux density B_i in Eq. (2.1) can be practically neglected against B_0, and J_c given by Eq. (2.1) is expected to be a constant. In other words, a sample with a small value of p can be asymptotically treated in the framework of the Bean model. On the contrary, for an extremely large value of p ($B_0 \ll B_i$), J_c sensitively varies depending on B_i.

To reveal the role of H_{c1} and ΔH in magnetization, we demonstrate in Fig. 3.1 typical initial and hysteresis $M(H)$ curves calculated using the appropriate magnetization equations for $H_{dc} = 0$, $H_{ac} = 4H_p$, and $p = 3$, where M and H are normalized to H_p and H_p is given by Eq. (2.12). First, we compare the $M(H)$ curves for $H_{c1} = 0$ and $0.15H_p$, in both cases $\Delta H = 0$ [Fig. 3.1(a)]. As seen in the figure, the hysteresis curve for $H_{c1} = 0$ (solid loop) is distorted when $H_{c1} = 0.15H_p$ and a step-like structure appears in the loop (dashed loop), where the central line of the loop ($M/H_p = 0$ at $H_{c1} = 0$) shifts up (left-hand side of the loop) and down (right-hand side of the loop), and the difference becomes 0.3 ($= 2H_{c1}/H_p$). This means the step width caused by a nonzero value of H_{c1} gives $2H_{c1}$.

Therefore, by measuring the shift of the central line in the distorted hysteresis loop, we can determine H_{c1}. Note that measurements of *full*-hysteresis loops are not always necessary, because the up and down deviations of the central line for a nonzero value of H_{c1} are equal.

In Fig. 3.1(b), we compare the cases of $\Delta H = 0$ and $0.1H_p$, where in both cases, $H_{c1} = 0.15H_p$. The effect of ΔH is not easy to see from an individual measurement because a distinctive change in the profile is not caused by ΔH. However, as seen in the figure, comparison of

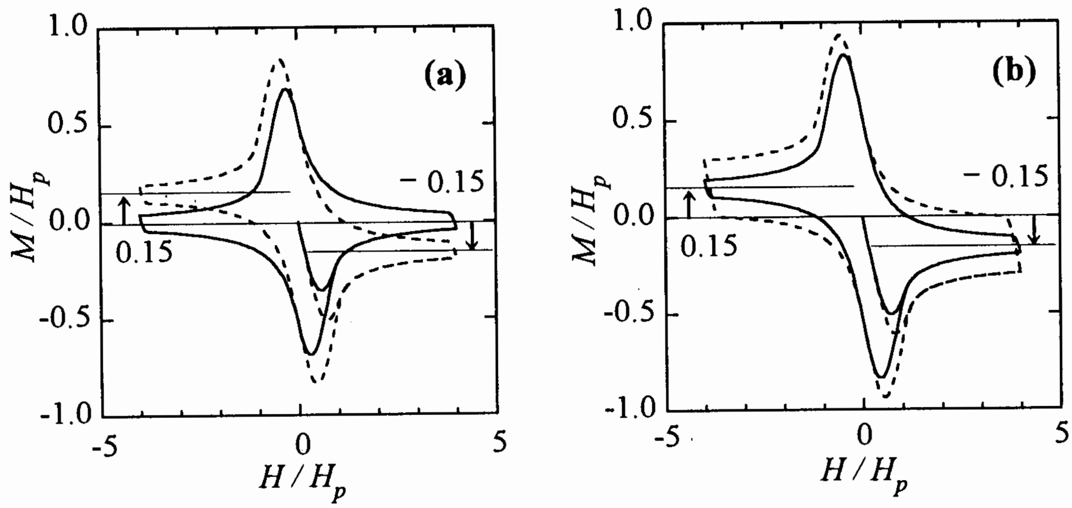

FIG. 3.1. Theoretical $M(H)$ curves, scaled by H_p, for $H_{dc} = 0$, $H_{ac} = 4H_p$, and $p = 3$. (a) Solid loop is for $\Delta H = H_{c1} = 0$ and dashed loop is for $\Delta H = 0$, $H_{c1} = 0.15H_p$. (b) Solid loop is for $\Delta H = 0$, $H_{c1} = 0.15H_p$ and dashed loop is for $\Delta H = 0.1H_p$, $H_{c1} = 0.15H_p$.

the loop for $\Delta H = 0$ (solid loop) with that for $\Delta H = 0.1H_p$ (dashed loop) reveals that the loop is expanded up and down when ΔH has a nonzero value. Noteworthy is that the deviation of the central line for $\Delta H = 0.1H_p$ from the initial position ($M/H_p = 0$) is the same with that for $\Delta H = 0$. This implies that in the present method for determinations of H_{c1}, the effect of surface barriers is completely excluded.

At this stage, we would like to comment on the widely applied conventional method for determinations of H_{c1}; observations of a deviation of $M(H)$ from the Meissner slope in the initial magnetization. In Fig. 3.2(a), we show the expanded initial $M(H)$ curve of Fig. 3.1(a). When $\Delta H = H_{c1} = 0$, the $M(H)$ curve begins to deviate from the Meissner slope at the very beginning of the applied field (solid curve). When $\Delta H = 0$ and $H_{c1} = 0.15H_p$, linearity of the $M(H)$ curve holds until $|M/H_p| = 0.15$ and then the magnetization begins to deviate from the straight Meissner line (dashed curve), suggesting this conventional method gives a correct value of H_{c1}.

On the contrary, as shown in Fig. 3.2(b) [the expanded figure of Fig. 3.1(b)], the initial magnetization curve for $\Delta H = 0.1H_p$ and $H_{c1} = 0.15H_p$ holds its linearity up to $|M/H_p| =$

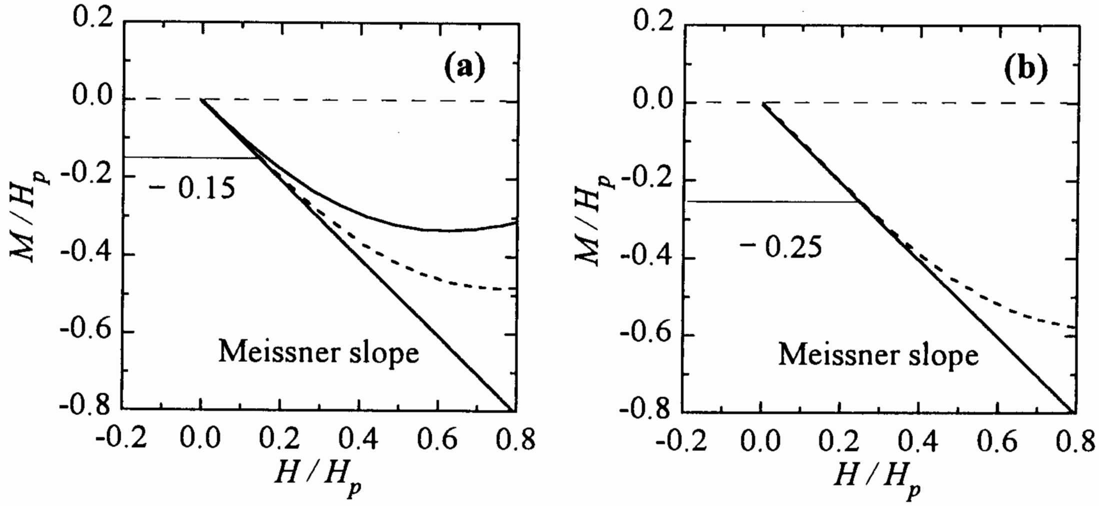

FIG. 3.2. (a) Expanded figure of Fig. 3.1(a); solid curve is for $\Delta H = H_{c1} = 0$ and dashed curve is for $\Delta H = 0$, $H_{c1} = 0.15H_p$. (b) Expanded figure of Fig. 3.1(b); dashed curve is for $\Delta H = 0.1H_p$, $H_{c1} = 0.15H_p$. Straight-line segments indicate the Meissner slope.

$|(\Delta H + H_{c1})/H_p)| = 0.25$ (dashed curve). If one adopts this value as H_{c1}, it is apparently overestimated. Accordingly, H_{c1} determined from the deviation of the initial magnetization line should be corrected when surface barriers exist.

It should be noticed that the magnetization equations $M(H)$ used here do not involve any contribution of intrinsic paramagnetism due to some magnetic ions such as lanthanide elements, Gd^{+3}, Dy^{+3}, Ho^{+3}, and Er^{+3}, because the present theoretical treatments concern only the superconducting-state $M(H)$. However, the paramagnetic element contained in a sample, if any, certainly slopes the magnetization $M(H)$ [78]. Therefore, for such a sample, the normal-state $M(H)$ should be evaluated as a correction term for the observed superconducting-state $M(H)$ curve.

III. EXPERIMENTAL

A. Sample Preparation

The Bi2212 single crystal was grown by the self-flux method. The axes of the crystal were determined by the x-ray diffraction; $a = b = 0.541$ nm and $c = 3.088$ nm. Raman scattering and electron probe microanalysis could not detect any impurity phase and revealed a very good lateral and vertical homogeneity of the stoichiometry of the crystal. The onset temperature of the superconducting transition T_c determined in terms of complex susceptibilities is 80.0 K. The reason of adopting T_c here is that it can be precisely determined from the measurement of complex susceptibilities. More details of the sample preparation and structural characterizations were previously reported [14].

The Y123 single crystal was also grown by the self-flux method. The axes determined by the x-ray diffraction measurement were $a = 0.381$ nm, $b = 0.388$ nm, and $c = 1.167$ nm. A high crystallinity was confirmed by Raman scattering and electron probe microanalysis, and no impurity phase was detected. T_c is 89.0 K. More details of the sample preparation and structural characterizations were previously reported [79].

B. Measurements of Magnetization Curves

Magnetization curves were measured at various temperatures below T_c using SQUID, where the applied field $\mu_0 H$ was parallel and perpendicular to the c axis of the specimen and ranged from zero up to 1 T at maximum, giving half of the hysteresis loop at each temperature.

In Fig. 3.3, we show typical initial and hysteresis curves of Bi2212 at 17.5 and 42.5 K, where the applied field is parallel to the c axis. The observed $M(H)$ curves were carefully corrected for the effect of a gelatin capsule in which the sample was mounted. At each temperature, we find the specific step-like structure and it is evident that at 42.5 K, the applied field exceeds the irreversibility field. As discussed before, the observed step width $H'_{c1,c}$ from the base line ($\mu_0 M = 0$) certainly corresponds to the lower critical field. However, the sample is not an infinite cylinder

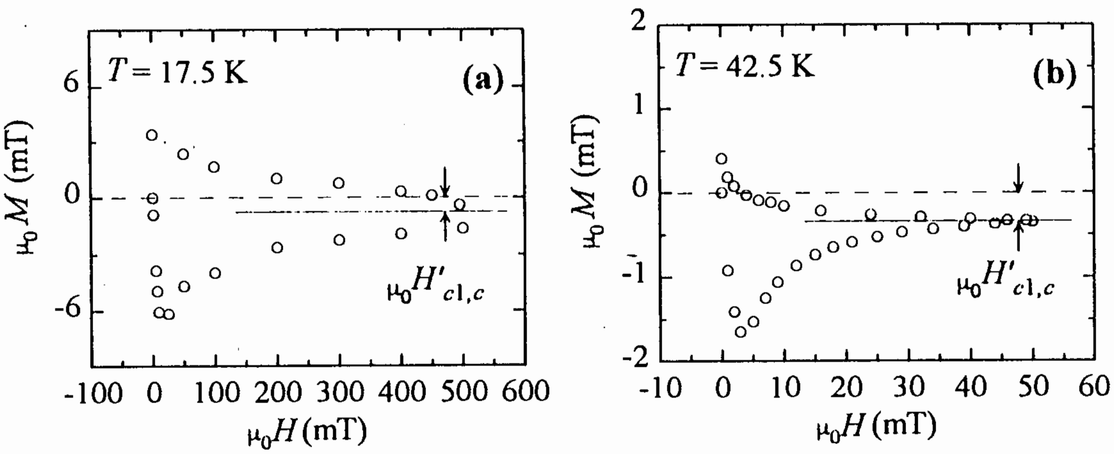

FIG. 3.3. Initial and hysteresis curves of single-crystal Bi2212 (a) at 17.5 K and (b) at 42.5 K, where the magnetic field is parallel to the c axis.

treated in the calculation, and therefore $H'_{c1,c}$ should be corrected for the demagnetization effect. Since the form of the specimen is a thin platelet, of which the dimensions are 1, 1, and 0.1 mm, the demagnetization coefficient for the direction in question, N_c, was approximately estimated to be 0.87 [80, 81]. Using $H_{c1,c} = H'_{c1,c}/(1 - N_c)$, we can obtain $H_{c1,c}$, the lower critical field for the applied field parallel to the c axis. In Fig. 3.4, are shown $M(H)$ curves of Bi2212 at 32.5 and 55.0 K, where the applied field is perpendicular to the c axis. Similar to the above case, we determined $H'_{c1,ab}$ as the step width from the base line ($\mu_0 M = 0$). Since the sample thickness is 0.1 mm, the demagnetization coefficient is quite small, $N_{ab} = 0.06$. We obtained $H_{c1,ab}$ for the applied field perpendicular to the c axis using $H_{c1,ab} = H'_{c1,ab}/(1 - N_{ab})$.

In Fig. 3.5, we show typical initial and hysteresis curves of Y123 at 10.0 and 45.0 K, where the applied field is parallel to the c axis. Since the specimen has the dimensions, 0.3, 0.3, and 0.1 mm, the demagnetization coefficient for the direction in question, N_c, was approximately estimated to be 0.58 and using this value, we obtained $H_{c1,c}$. In Fig. 3.6, we show $M(H)$ curves of Y123 at 30.0 and 55.0 K, where the applied field is perpendicular to the c axis. $H'_{c1,ab}$ determined as the step width from the base line ($\mu_0 M = 0$) was corrected using the demagnetization coefficient $N_{ab} = 0.21$.

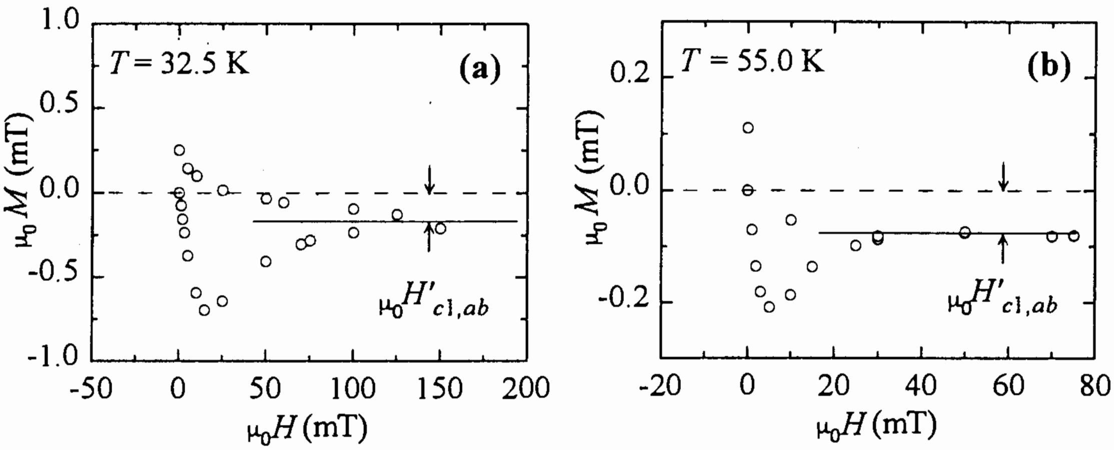

FIG. 3.4. Initial and hysteresis curves of single-crystal Bi2212 (a) at 32.5 K and (b) at 55.0 K, where the magnetic field is perpendicular to the c axis.

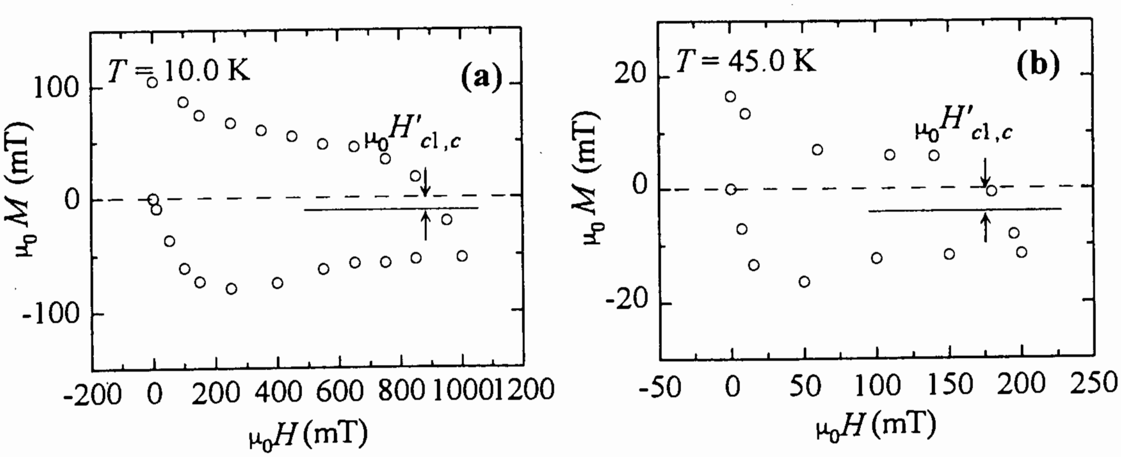

FIG. 3.5. Initial and hysteresis curves of single-crystal Y123 (a) at 10.0 K and (b) at 45.0 K, where the magnetic field is parallel to the c axis.

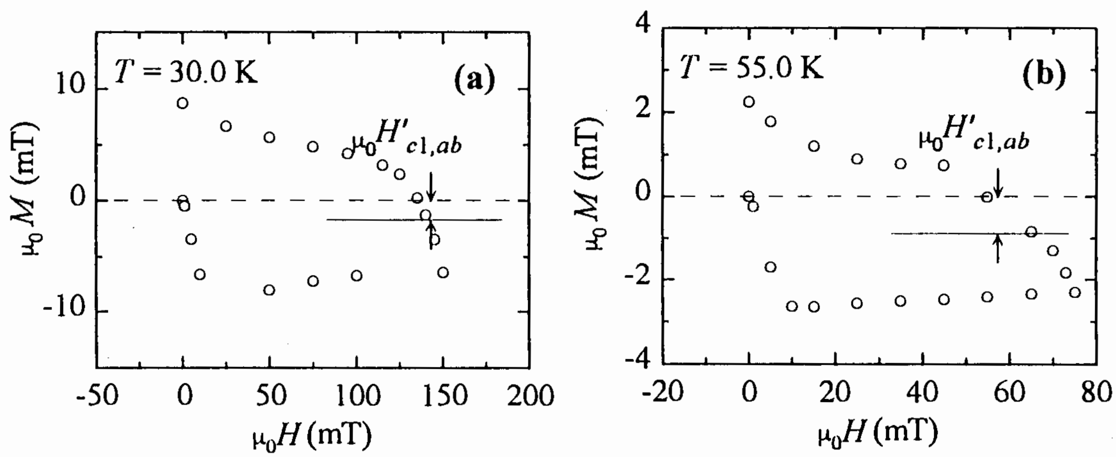

FIG. 3.6. Initial and hysteresis curves of single-crystal Y123 (a) at 30.0 K and (b) at 55.0 K, where the magnetic field is parallel to the c axis.

IV. RESULTS AND DISCUSSION

In Figs. 3.7(a) and (b) and Figs. 3.8(a) and (b), we plot $\mu_0 H_{c1,c}$, $\mu_0 H_{c1,ab}$ versus T obtained from the observed $M(H)$ curves of Bi2212 and Y123, respectively. From the figures, we find the following features.

(1) A least-squares fitting of $\mu_0 H_{c1,c}$ and $\mu_0 H_{c1,ab}$ of Bi2212 in the temperature region 40 K $< T < T_c$ and that of Y123 below T_c give

$$H_{c1,c}(T) \quad = \quad H_{c1,c}(0)[1-(T/T_c)^{2.6}] \qquad (H \parallel c \text{ axis of Bi2212}), \tag{3.1a}$$

$$H_{c1,ab}(T) \quad = \quad H_{c1,ab}(0)[1-(T/T_c)^{4.1}] \quad (H \perp c \text{ axis of Bi2212}), \tag{3.1b}$$

$$H_{c1,c}(T) \quad = \quad H_{c1,c}(0)[1-(T/T_c)^{1.0}] \qquad (H \parallel c \text{ axis of Y123}), \tag{3.2a}$$

$$H_{c1,ab}(T) \quad = \quad H_{c1,ab}(0)[1-(T/T_c)^{1.3}] \quad (H \perp c \text{ axis of Y123}), \tag{3.2b}$$

where $\mu_0 H_{c1,c}(0)$ and $\mu_0 H_{c1,ab}(0)$ determined by extrapolating the fitting curves are 3.7 and 0.1 mT for Bi2212, and 18.0 and 2.7 mT for Y123, respectively.

(2) In Fig. 3.7, both $\mu_0 H_{c1,c}$ and $\mu_0 H_{c1,ab}$ for Bi2212 show an anomalous upturn in the temperature region below about 40 K. Especially, the enhancement of $\mu_0 H_{c1,ab}$ is remarkable, while deviations of $\mu_0 H_{c1,c}$ from Eq. (3.1a) is relatively small. On the contrary, both $\mu_0 H_{c1,c}$ and $\mu_0 H_{c1,ab}$ for Y123 have no anomalous upturn, as shown in Fig. 3.8.

We first discuss about Eqs. (3.1) and (3.2) deduced from observed H_{c1}. In the GL theory [4], the formulas for anisotropic H_{c1} and the GL parameter κ are given as [75]

$$\mu_0 H_{c1,c} \quad = \quad \frac{\phi_0}{4\pi\lambda_{ab}^2}(\ln\kappa_c + 0.5), \tag{3.3}$$

$$\mu_0 H_{c1,ab} \quad = \quad \frac{\phi_0}{4\pi\lambda_{ab}\lambda_c}(\ln\kappa_{ab} + 0.5), \tag{3.4}$$

$$\kappa_c \quad = \quad \frac{\lambda_{ab}}{\xi_{ab}}, \tag{3.5}$$

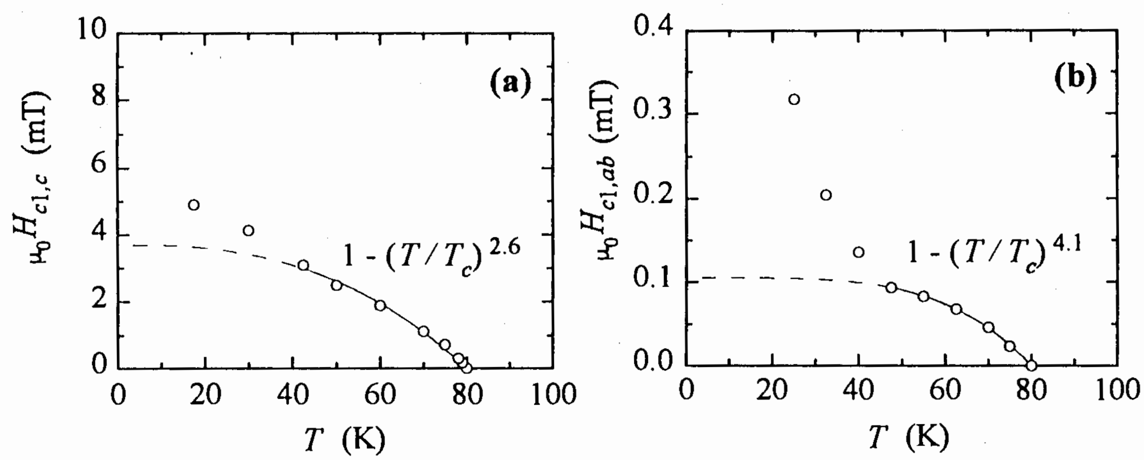

FIG. 3.7. Temperature dependence of lower critical fields (a) $H_{c1,c}(T)$ and (b) $H_{c1,ab}(T)$ for single-crystal Bi2212.

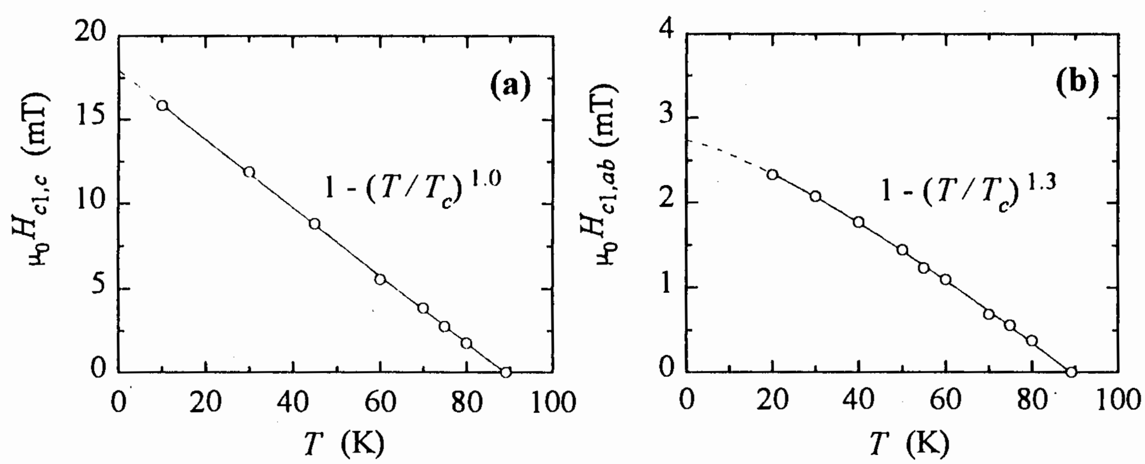

FIG. 3.8. Temperature dependence of lower critical fields (a) $H_{c1,c}(T)$ and (b) $H_{c1,ab}(T)$ for single-crystal Y123.

$$\kappa_{ab} = \frac{\lambda_c}{\xi_{ab}} = [\frac{\lambda_c}{\xi_c} \cdot \frac{\lambda_{ab}}{\xi_{ab}}]^{1/2}, \quad (3.6)$$

where ϕ_0 is the flux quantum, λ is the penetration depth, and ξ is the coherence length. The subscripts c and ab on κ denote the direction of the applied field, and these on λ and ξ denote the direction of the current.

Substituting $\lambda_{ab}(0) = 0.42\ \mu$m and $\kappa_c(0) \approx 100$ for Bi2212 [59, 82], and $\lambda_{ab}(0) = 0.14\ \mu$m and $\kappa_c(0) = 89$ for Y123 [83, 84] into Eq. (3.3), we obtain $\mu_0 H_{c1,c}(0) \approx 4.8$ and 40.0 mT, which are comparable to the present result, 3.7 and 18.0 mT. From Eqs. (3.3) and (3.4), the anisotropy γ defined as $\gamma = \lambda_c/\lambda_{ab}$ can be expressed by

$$\gamma = \frac{H_{c1,c}(0)}{H_{c1,ab}(0)} \cdot \frac{\ln \kappa_{ab}(0) + 0.5}{\ln \kappa_c(0) + 0.5}. \quad (3.7)$$

Using $\ln \kappa_c(0) \approx 4.5$ [59], $\ln \kappa_{ab}(0) = \ln[\lambda_c(0)/\xi_{ab}(0)] \approx 9.5$ [59, 85], $\mu_0 H_{c1,c}(0) \approx 3.7$ mT, and $\mu_0 H_{c1,ab}(0) \approx 0.1$ mT in Eq. (3.7), we obtain $\gamma \approx 74$ for Bi2212. Similarly, using $\ln \kappa_c(0) \approx 4.5$ [83], $\ln \kappa_{ab}(0) = \ln[\lambda_c(0)/\xi_{ab}(0)] \approx 6.1$ [84], $\mu_0 H_{c1,c}(0) = 18.0$ mT, and $\mu_0 H_{c1,ab}(0) = 2.8$ mT in Eq. (3.7), we obtain $\gamma \approx 8.5$ for Y123.

The anisotropic nature of the present Bi2212 was also examined by means of the polarized micro-Raman spectra at room temperature [14]. The symmetric A_{1g} modes were detected under the $x(zz)\bar{x}$ (parallel to the c axis) and $z(xx)\bar{z}$ (perpendicular to the c axis) scattering configurations (see Fig. 3.9). The most prominent result is that the phonons at ~ 630 cm^{-1} are strongly c-axis polarized, as is evident in the $x(zz)\bar{x}$ spectrum. The intensity is approximately 60 times higher than that observed under $z(xx)\bar{z}$ scattering configuration. It is worth notice that the structural anisotropy found from the Raman spectra, $x(zz)\bar{x}/z(xx)\bar{z} \approx 60$, roughly coincides with $\gamma \approx 74$ estimated from our H_{c1} measurements. Furthermore, the anisotropy found for Y123 by Clem [72], $\gamma \approx 5$, has also the same order with $\gamma \approx 8.5$ estimated from our H_{c1} measurements. The correspondence could be an indirect support for the present results.

Recently, Radtke *et al.* [86] proposed a theory based on incoherent quasiparticle hopping between the CuO_2 layers of the cuprate-based superconductor and demonstrated that the experimental evidence for the London penetration-depth tensor with a weak temperature dependence along the c axis is not in contradiction with d-wave pairing deduced from in-plane measurements. In their work (see Fig. 3.10), it has been revealed that for materials like Bi2212 with c-axis mean-free paths much less than the lattice spacing, the c-axis penetration-depth ratio

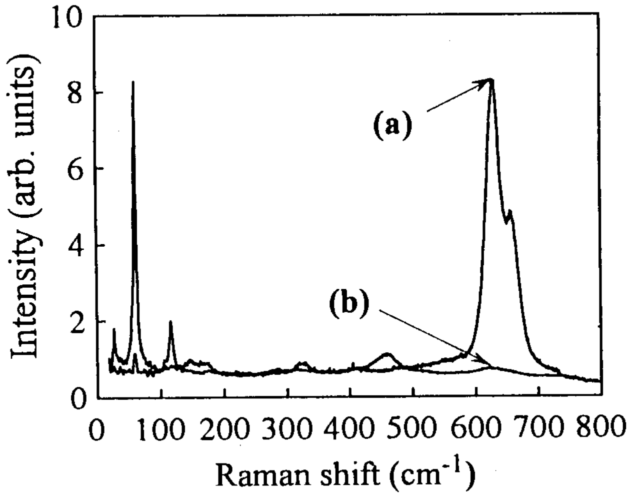

FIG. 3.9. Polarized micro-Raman spectra of single-crystal Bi2212 from two main scattering configurations, (a) $x(zz)\bar{x}$ and (b) $z(xx)\bar{z}$ [14]. Comparing the polarized spectra (a) and (b), one notes that the apical-oxygen phonon at $\sim$ 630 cm^{-1} has clearly dominating Raman tensor component zz.

$\lambda_c^2(0)/\lambda_c^2(T)$ is larger than the ab-plane penetration-depth ratio $\lambda_{ab}^2(0)/\lambda_{ab}^2(T)$ at all temperatures. They also pointed out that the d-wave $\lambda_c^2(0)/\lambda_c^2(T)$ resembles the s-wave case, but the difference between c-axis and in-plane penetration-depth ratios is much more pronounced for d-wave pairing. Meanwhile, for materials like Y123, the behavior of $\lambda_c^2(0)/\lambda_c^2(T)$ and $\lambda_{ab}^2(0)/\lambda_{ab}^2(T)$ depends on the oxygen content. When the oxygen content is very close to 7 ($\delta \approx 0$ in $YBa_2Cu_3O_{7-\delta}$), the c-axis and ab-plane penetration-depth ratios are the same when the direct hopping is present. On the contrary, in underdoped compounds with $\delta > 0$, the profiles of $\lambda_c^2(0)/\lambda_c^2(T)$ and $\lambda_{ab}^2(0)/\lambda_{ab}^2(T)$ become more or less similar to the case for materials like Bi2212.

Motivated by their prediction, we derived $\lambda_c^2(0)/\lambda_c^2(T)$ and $\lambda_{ab}^2(0)/\lambda_{ab}^2(T)$ from Eqs. (3.1) – (3.6), and calculated the penetration-depth ratios as a function of the reduced temperature T/T_c, where the GL parameter κ was tentatively assumed to be constant [87]. As shown in Fig. 3.11, the calculated penetration-depth ratios drawn (a) for Bi2212 without taking account of the anomalous upturn of H_{c1} and (b) for Y123 reproduce pretty well the prediction by the hopping model, although the exponent in Eq. (3.1) for Bi2212 seems to be larger than that given in their

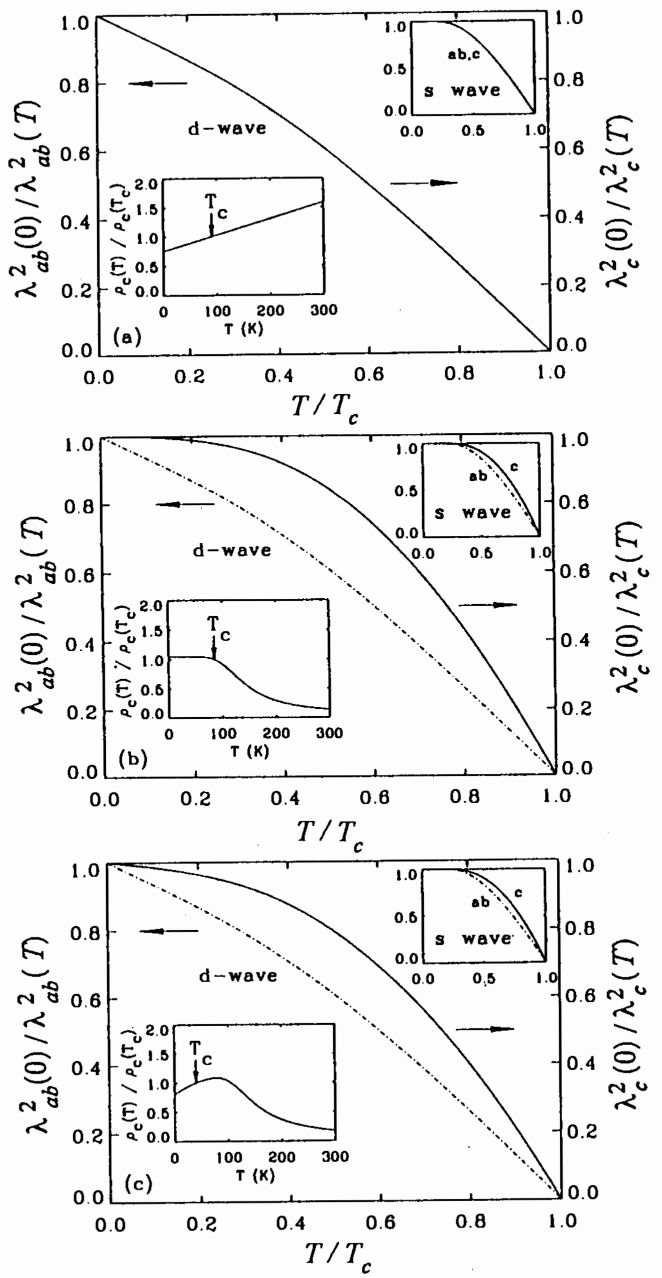

FIG. 3.10. Penetration depth ratios $\lambda_{ab}^2(0)/\lambda_{ab}^2(T)$ (dot-dashed line) and $\lambda_c^2(0)/\lambda_c^2(T)$ (solid line) as a function of the reduced temperature T/T_c for both d-wave (main figure) and s-wave (upper-right inset) pairing in different limits of the incoherent hopping model described by Radtke *et al.* [86]. The corresponding c-axis resistivity ρ_c is shown in the lower-left inset normalized to its value at T_c as a function of temperature. The limits illustrated are (a) direct hopping, which may be relevant for $YBa_2Cu_3O_{6.9}$, (b) assisted hopping, which may be the case in Bi2212, and (c) a combination of these processes, which may be obtained in underdoped compounds like $YBa_2Cu_3O_{6.4}$. Note in (a) that both the ab- and c-axis penetration-depth ratios are the same when only direct hopping is present.

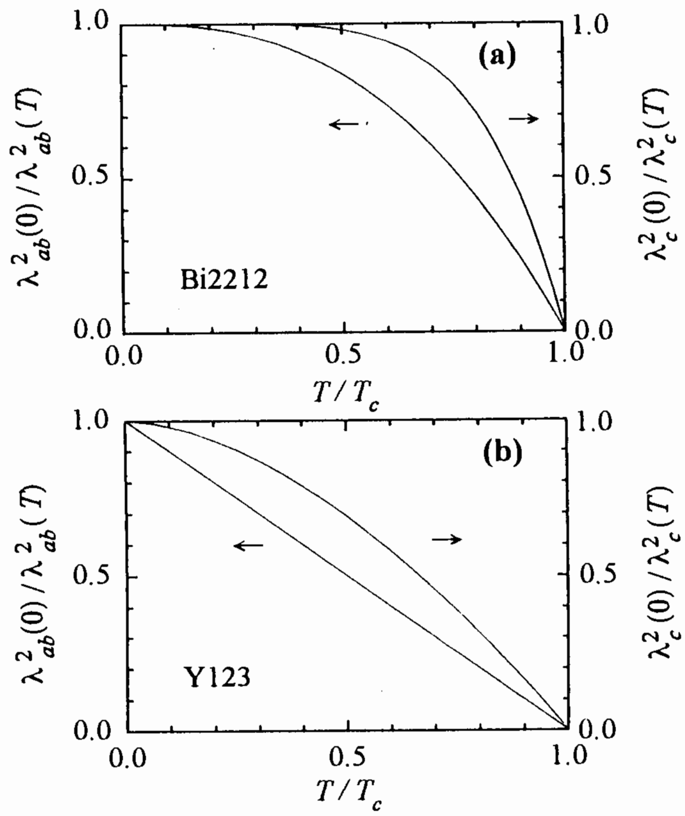

FIG. 3.11. Penetration-depth ratios $\lambda_{ab}^2(0)/\lambda_{ab}^2(T)$ and $\lambda_c^2(0)/\lambda_c^2(T)$ versus reduced temperature T/T_c derived from Eqs. (3.1) – (3.6).

calculations, indicating that the nature of Bi2212 would lie between *s*- and *d*-wave pairings. Referring the value of T_c of the present Y123, we assign the content δ in $YBa_2Cu_3O_{7-\delta}$ to approximately 0.3 [88]. The calculated ratios demonstrated in Fig. 3.11(b) lie between Figs. 3.10(a) and (c), but still seem to show the characteristic of *d*-wave pairing. Unfortunately, reliable resistivity measurements along the *c* axis were not successful.

Concerning the anomalous enhancement of H_{c1}, it has been pointed out that experimental ambiguities possibly give rise to the anomaly [58–61, 63, 69, 74]. However, from theoretical predictions discussed in Sec. II of this chapter, we may insist that in the present measurement, surface barriers are not involved in H_{c1}'. Besides, volume flux pinning which may bother precise determinations of H_{c1} from the initial magnetization curve does not practically affect the result in the present method.

There are some ambiguities in the demagnetization coefficients N_c and N_{ab} given in the previous section. However, a differing demagnetization cannot change the exponents of Eqs.

(3.1) and (3.2). It can only modestly vary $H_{c1}(0)$.

From Eqs. (3.3) – (3.6), we may say that the anomalous upturn of H_{c1} should be caused by either $\lambda(T)$ or $\xi(T)$. In fact, Chen *et al.* [74] reported that the variation of the GL parameter κ in the low temperature region, if any, causes the anomalous upturn in $H_{c1}(T)$. The temperature dependence of λ has been studied by many workers [86, 89–96]. However, to the author's knowledge, anomalous temperature dependence of λ has not so far been published. If λ does not participate in the anomaly of H_{c1}, it is reasonable to assume that $\xi(T)$ gives rise to the anomaly of $H_{c1}(T)$. As shown in Figs. 3.5(a) and (b) for Bi2212, the anomaly of $H_{c1,ab}$ is much more remarkable than that of $H_{c1,c}$. This suggests that $\xi_c(T)$ rather than $\xi_{ab}(T)$ plays an essential role in the anomalous enhancement of $H_{c1,ab}$, although a weaker anomalous enhancement of $H_{c1,c}$ remains to be resolved. On the contrary, both $H_{c1,c}$ and $H_{c1,ab}$ for Y123 do not show any anomalous upturn. The values of $\xi_c(0)$ for Bi2212 [97] and for Y123 [84] are reported as 0.28 and 0.30 nm, respectively, being nearly the same. Meanwhile, the lattice spacing of the CuO_2 planes is approximately 3 nm in Bi2212 [98] and 0.3 nm in Y123 [79, 99].

As mentioned before, Koyama *et al.* [69] used a model of multilayer structure which is composed of arrays of superconducting and normal layers, and found that the superconducting order parameter on the normal layers is much enhanced at low temperatures. To calculate H_{c1} of a multilayer superconductor, they considered the GL free energy functional in terms of the order parameters. The order parameter on the normal layers is much smaller than that on the superconducting layers at high temperatures near T_c. Thus the superconducting order is maintained mostly by the superconducting layers in this temperature region. However, the superconducting order on the normal layers rapidly grows with decreasing temperature, so that both the superconducting and normal layers participate in forming the superconducting state in the low temperature region. Therefore, the superconducting condensation energy rapidly increases with decreasing temperature. They concluded the drastically enhanced H_{c1} at low temperatures is due to a proximity effect. Their theoretical prediction seems to be applicable for interpretation of the present results, i.e., the ten-times larger lattice spacing of Bi2212 could be a source of the anomalous enhancement of H_{c1}.

It is worthwhile to note about the work on the upper critical field of a V/Ag multilayered system (non-oxide superconductor). Kanoda *et al.* [100, 101] investigated the upper criti-

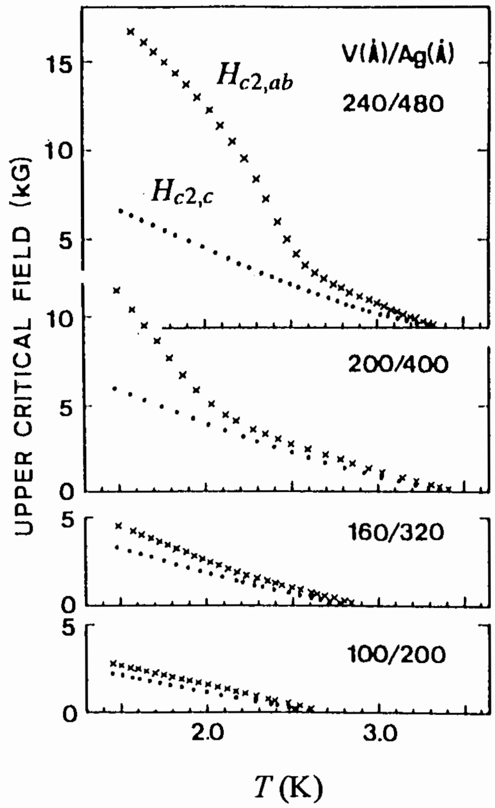

FIG. 3.12. Dimensional crossover of upper critical fields for V-Ag proximity-coupled superconducting multilayer structures. The thickness ratio of V and Ag is 1:2 [100].

cal fields ($H_{c2,c}$ and $H_{c2,ab}$) of a proximity-coupled superconducting multilayer composed of V (superconducting layers) and Ag (normal layers), where the subscripts c and ab on H_{c2} denote the direction of the applied field. They observed a drastic upturn of $H_{c2,ab}$ $(= \phi_0/2\pi\mu_0\xi_{ab}\xi_c)$ at low temperatures when the thickness of the normal layer (Ag) exceeds a certain limit (see Fig. 3.12). Their investigation of the coherence length has revealed that two types of anomalies in the temperature dependence of $H_{c2,ab}$ are tightly concerned with the commensurability between the vortex lattice and the multilayer structure. From the standpoint of dimensionality, the commensurability involved in the former anomaly eventually leads to a crossover from three- to two-dimensions, by which the upturn is greatly enhanced. An apparent resemblance between the dimensional crossover for a V/Ag multilayer and the anomalous upturn of $H_{c1,ab}$ of the present single-crystal Bi2212 with large lattice spacing is suggestive.

V. CONCLUSIONS

Using the magnetization equations of type-II superconductors derived within the framework of the modified KA critical-state model, it has been revealed that hysteresis loops are distorted when the lower critical field H_{c1} has a nonzero value and a step-like structure is induced in the loop. In addition, it has been proved that this step width correctly corresponds to $2H_{c1}$ without involving the effect of surface barriers.

Based on this theoretical prediction, we measured $M(H)$ curves of Bi2212 and Y123 single crystals by SQUID at various temperatures below the onset temperature T_c of the superconducting transition. The observed step widths in the hysteresis loops for both orientations of the applied fieldCparallel and perpendicular to the c axis, were corrected for the demagnetization coefficients, and $H_{c1,c}$ ($H \parallel c$ axis), $H_{c1,ab}$ ($H \perp c$ axis) thus obtained were plotted as a function of temperature. From the results, we find that $H_{c1,c}(T)$ and $H_{c1,ab}(T)$ for Bi2212 show an anomalous upturn below about 40 K (especially, the enhancement of $H_{c1,ab}$ is remarkable), but those for Y123 do not show any anomaly.

A least-squares fitting of $\mu_0 H_{c1,c}$ and $\mu_0 H_{c1,ab}$ for Bi2212 in the temperature region 40 K $< T < T_c$ gave $H_{c1,c}(T) = H_{c1,c}(0)[1-(T/T_c)^{2.6}]$ and $H_{c1,ab}(T) = H_{c1,ab}(0)[1-(T/T_c)^{4.1}]$, where $\mu_0 H_{c1,c}(0) = 3.7$ mT and $\mu_0 H_{c1,ab}(0) = 0.1$ mT. The fitting for Y123 below T_c gave $H_{c1,c}(T) = H_{c1,c}(0)[1-(T/T_c)^{1.0}]$ and $H_{c1,ab}(T) = H_{c1,ab}(0)[1-(T/T_c)^{1.3}]$, where $\mu_0 H_{c1,c}(0) = 18.0$ mT and $\mu_0 H_{c1,ab}(0) = 2.7$ mT. The values of $\mu_0 H_{c1,c}(0)$ are comparable to that calculated using the formulas for anisotropic H_{c1} in the GL theory. Analyses of the observed data by a theory based on incoherent quasiparticle hopping between the CuO_2 layers were also attempted. In accordance with the work by Radtke *et al.* [86], we calculated the penetration-depth ratios $\lambda_c^2(0)/\lambda_c^2(T)$ and $\lambda_{ab}^2(0)/\lambda_{ab}^2(T)$. Plots of the ratios as a function of the reduced temperature T/T_c qualitatively reproduce the prediction from the hopping model, and suggest that both Bi2212 and Y123 seem to possess the nature of d-wave pairing.

As to the anomalous upturn, we dilate qualitative discussion with the aid of the formulas for anisotropic H_{c1} in the GL theory. Analyses of the observed remarkable anomaly of $H_{c1,ab}(T)$ for Bi2212 suggest that the temperature dependence of the coherence length in the direction of the current, ξ_c, plays an essential role. The notable difference of the $H_{c1}(T)$ behavior between

Bi2212 and Y123 could be interpreted by a proximity effect when we consider the ten-times larger lattice spacing of Bi2212 compared to that of Y123.

Chapter 4

Complex Susceptibilities and Material Parameters in the Kim–Anderson Model

I. INTRODUCTION

The time-dependent magnetization $M(\omega t)$ of a specimen for a magnetic field $H(\omega t) = H_{dc} + H_{ac}\cos(\omega t)$ can be generally expressed in the form of a Fourier expansion:

$$M(\omega t) \;=\; \chi_0 H_{dc} + H_{ac}\sum_{n=1}^{\infty}\mathrm{Re}[\chi_n \exp(in\omega t)]. \tag{4.1}$$

Re[ ] denotes the real part of a complex variable and $\omega = 2\pi f$, where f is the fundamental frequency. The first term $\chi_0 H_{dc}$ is a time-independent contribution or "offset" which is due to the dc magnetic field H_{dc}. The second term is the time-dependent component associated with the ac magnetic field $H_{ac}\cos(\omega t)$. Here we define the Fourier coefficients of the magnetization $\chi_n = \chi_n' - i\chi_n''$ $(n = 1, 2, 3, \ldots)$ as the harmonic ac susceptibilities, where χ_1 is the fundamental susceptibility and the others are the higher-harmonic susceptibilities.

Physically, the fundamental susceptibility $\chi_1 = \chi_1' - i\chi_1''$ is well understood. For a superconducting sample, it is evident that the sharp change in χ_1' with respect to temperature is caused by the shielding effect of the sample against the applied magnetic field. Meanwhile, χ_1'' is proportional to the energy dissipation in the sample located in a periodically varying magnetic field. The reason for this is as followings: The time-averaged variation of free energy in a material located in a magnetic field is given by

$$Q \;=\; \langle -MdH/dt\rangle_t, \tag{4.2}$$

where Q is the mean energy dissipation per unit time per unit volume, M is the magnetization, and H is a uniform external magnetic field. Substituting $H = H_{ac}\exp(i\omega t)$ in Eq. (4.2), Q becomes

$$Q \;=\; -\frac{1}{2}\mathrm{Re}[i\omega MH^*] = \frac{1}{2}\omega \mathrm{Im}[MH^*], \tag{4.3}$$

where Im[ ] denotes the imaginary part. Since magnetization is given as $M = (\chi_1' - i\chi_1'')H$, one gets

$$Q \;=\; \frac{1}{2}\omega\chi_1'' H_{ac}^2. \tag{4.4}$$

As the energy dissipation in the sample directly depends on the structure, the proportionality between Q and χ_1'' is useful for searching structural characteristics of the sample.

To elucidate the generation of higher-harmonic components χ_n ($n \geq 2$) for superconductors, several models have been proposed. These are roughly divided into two categories. One is based on the critical-state model, introduced by Bean on the assumption that the critical-current density is independent of the local magnetic field in the sample [16, 22, 23]. In his model the existence of odd-n harmonic susceptibilities can be derived. Bean's approach was extended by Kim, Hempstead, and Strnad [17, 18] and Anderson [19], who assumed that every region of the sample carries a critical-current density determined by the local magnetic field. In this model one can derive only odd-n harmonics when a pure ac field is applied to a superconductor. But if a dc field is superimposed on the ac field, even-n harmonics are generated.

The second category is the so-called weak-link model, which was proposed by Ishida and Mazaki for a multiconnected microbridge network of low-temperature superconductors [102]. The expressions derived from this model are equivalent to those of Rollins and Silcox [103]. The weak-link model can prove the existence of odd-n harmonic susceptibilities and qualitatively explains the profile of χ_n versus temperature observed for weakly coupled networks. However, the weak-link model cannot generate even-n harmonic terms even under a superimposed dc field. Therefore, in the present work, the use of the Kim–Anderson (KA) critical-state model seems to be appropriate.

A widely applied technique for the measurement of complex susceptibilities is the Hartshorn-type mutual inductance bridge which was first introduced by Hartshorn [104]. Using this bridge, we measured χ_n for variety of cuprate-based oxide superconductors and attempted to test the superconducting quality of the samples used. Analyses of the observed χ_n were carried out using the KA model [28], where we used the material parameters k and B_0 involved in the model as the fitting parameters. From these treatments, we determined the temperature dependence of k and B_0 [105].

In this chapter, we present the details of the measurement of χ_n and then develop analyses of the results within the construct of the KA model. Measurements of χ_n together with the magnetization curves can be applied to determine the temperature dependence of the material parameters k and B_0.

II. COMPLEX SUSCEPTIBILITIES

A. Measuring System

As shown in Fig. 4.1, the measuring system for the fundamental susceptibility χ_1 essentially consists of two coils M_1 and M_2, and the phase-shift potentiometer R [106]. The cryostat coil M_2, in which a sample is located, consists of two coaxial cylindrical coils. The inner coil (primary) is 7735 turns (in 8 layers and 155 mm in length) of Cu wire (0.14 mm in diameter) coated by polyvinyl formal (PVF). The inner diameter of the Lucite (polymethyl methacrylate) bobbin of the primary coil is 29 mm and the total resistance of the coil is 860 Ω at room temperature. The outer coil (secondary) is divided into two sections. Each section has 4880 turns of PVF wire (in 9 layers and 44 mm in length) in opposite direction to each other. The inner diameter of the secondary-coil bobbin is 35 mm and the total resistance of the coil is 700 Ω at room temperature. As a variable standard mutual inductance M_1, Tinsley type 4229 is used, of which the working range is 0.1 μH – 1.111 mH with the sensitivity of 0.01 μH. The phase-shift potentiometer is composed of a manganin wire (1 mm in diameter and 1 m in length) and of a slide contact. An alternating field is supplied from a function generator F. To achieve sufficient signal/noise ratios, a two-phase lock-in amplifier Ithaco 393 is used. The correction factor for calibration of the ac field from the supplied ac current was calculated assuming that the length of the inner cryostat coil is infinite. To avoid the bridge imbalance during the experiment, the cryostat coil was directly immersed in a liquid-N_2 or liquid-He bath. Phase setting of the lock-in amplifier was carefully made so as to give variation only to the in-phase signals, against the change in the bridge inductance.

Using the above system, we can measure the real and imaginary components of χ_1 continuously and simultaneously as a function of temperature T. The sample is placed inside a vacuum-tight Pyrex glass chamber which is then inserted into the cryostat coil (see Fig. 4.2). The sample chamber is set at the fixed place so that the sample to be measured is located at the upper section of the secondary coil. After evacuation of the sample chamber, the sample temperature is controlled by changing the pressure of He exchange gas (10^{-2} – 10^{-3} Torr). Since the thermal conductivity of oxide superconductors is rather poor compared to that of usual metallic

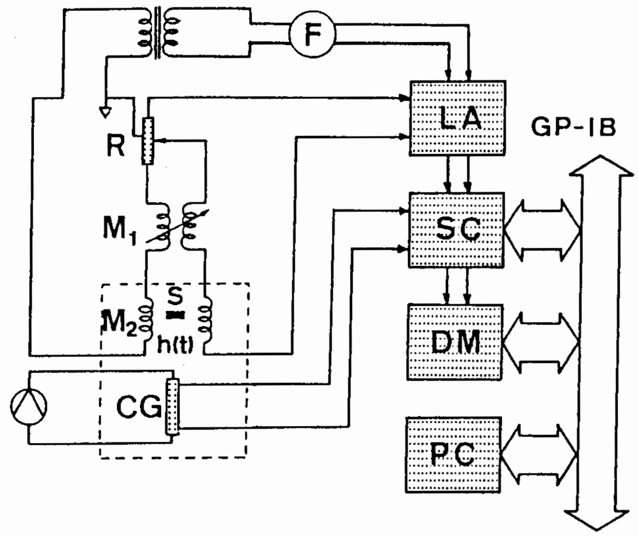

FIG. 4.1. The measuring system of the fundamental susceptibility [106]. M_1: variable standard mutual inductance, M_2: cryostat coil, R: phase-shift potentiometer, S: sample, CG: carbon-glass thermometer, LA: two-phase lock-in amplifier, SC: universal scanner, DM: computing digital multimeter, and PC: personal computer.

superconductors, one has to be very careful in the temperature control. In order to minimize the temperature gradient in the sample (or between the sample and the thermometer), the temperature should be changed quite slowly. Empirically, the temperature variation of 0.3 K/min is sufficient to eliminate the temperature gradient, and below this rate, the reproducibility of data is satisfactory. A null adjustment of the Hartshorn bridge is made at a sample temperature just above the critical temperature T_c. Temperature is measured with a calibrated carbon-glass thermometer. In this experiment, magnetic shielding was not used, and so the applied ac field was superimposed on the Earth's field $\mu_0 H_{dc} = 0.03$ mT [107].

The measuring system for the higher-harmonic susceptibilities χ_n ($n \geq 2$) is schematically shown in Fig. 4.3, where two function generators are used to extract the higher-harmonic components [106]. The ac magnetic field is applied to the sample using the function generator F-1 and the second generator F-2 is used to supply the nth-harmonic sinusoidal wave synchronized with F-1. By means of the Lissajous figure on an oscilloscope, we monitor the phase shift throughout one run of the measurement.

Since the bridge is balanced at the sample temperature just above T_c, the off-balance signal

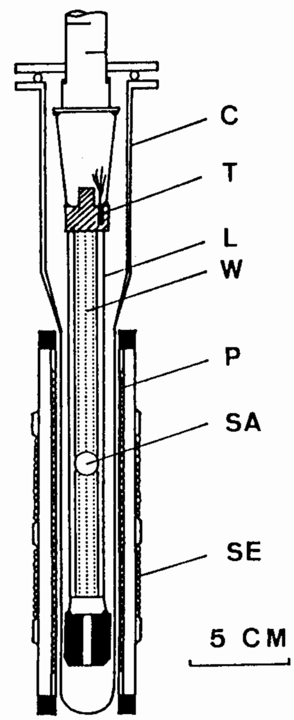

FIG. 4.2. Details of the sample holder and the adiabatic cell [106]. C: adiabatic cell, T: carbon-glass thermometer mounted in a Cu block, L: Lucite pipe, W: bundle of Cu wires, P: primary coil, SA: sample, and SE: secondary coil.

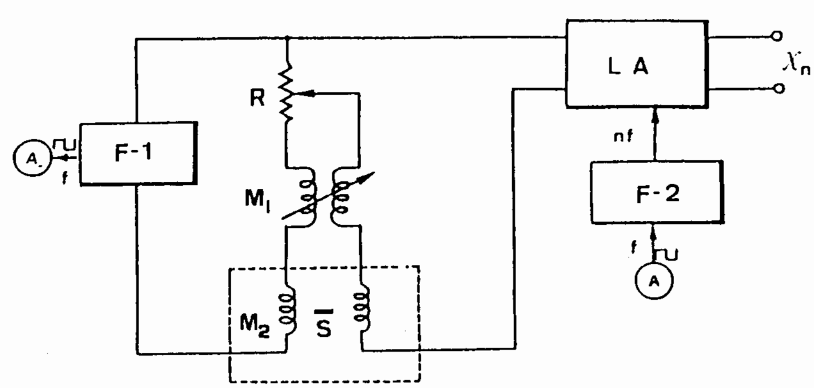

FIG. 4.3. Schematic diagram of the measuring system of higher-harmonic susceptibility [106]. M_1: variable standard mutual inductance, M_2: cryostat coil, R: phase-shift potentiometer, S: sample, F-1: function generator 1, F-2: function generator 2, and LA: two-phase lock-in amplifier.

$\upsilon(\omega t)$, induced in the secondary circuit by decreasing temperature, is directly proportional to the time derivative of the sample magnetization $M(\omega t)$. Using Eq. (4.1), one gets

$$\begin{aligned} \upsilon(\omega t) &= -\gamma\frac{dM(\omega t)}{dt} = -\gamma H_{ac}\sum_{n=1}^{\infty}\mathrm{Re}[in\omega\chi_n\exp(in\omega t)] \\ &= -\gamma H_{ac}\sum_{n=1}^{\infty}nw[-\chi_n'\sin(n\omega t)+\chi_n''\cos(n\omega t)], \end{aligned} \tag{4.5}$$

where γ is a constant which depends on the turn number of coils, on the volume and shape of the sample, as well as on its position in the coil.

Meanwhile, $\upsilon(\omega t)$ can be generally expressed in the form of a Fourier expansion

$$\upsilon(\omega t) = \sum_{n=1}^{\infty}\mathrm{Re}[a_n\exp(in\omega t)], \tag{4.6}$$

where $a_n = a_n' - ia_n''$ are the Fourier coefficients which are determined experimentally. From Eqs. (4.5) and (4.6), we get the real and imaginary components of the nth-harmonic susceptibilities as $\chi_n' = a_n''/\gamma n\omega H_{ac}$ and $\chi_n'' = -a_n'/\gamma n\omega H_{ac}$. In the present case, the Fourier coefficients a_n' and a_n'' were determined with the two-phase lock-in amplifier with which the nth-harmonic terms of $\upsilon(\omega t)$ were obtained. The reference signal $\upsilon_n \propto \cos(n\omega t)$ was input from F-2. Ideally, to obtain an absolute value of χ_n, γ should be determined by calibrating the susceptometer with a standard sample which has the same volume and shape as the specimen in question. In our case we normalized χ_n to the saturated value of $|\chi_1'|$ in a weak magnetic field, and γ was determined from $\chi_1' = -1$.

B. Typical Profiles of χ_n

Soon after the discovery of high-T_c superconductors, careful measurements of χ_1 for sintered $La_{1.9}Sr_{0.1}CuO_4$ were carried out by Mazaki *et al.* [108]. In the report, they pointed out that the superconducting transition in terms of the real component χ_1' has two phases; one phase observed in the temperature region $T_2 < T < T_1$ (see Fig. 4.4) does not depend on the ac field amplitude, but the other in the lower temperature region ($T < T_2$) sensitively varies depending on the amplitude. Besides, in the temperature region $T_2 < T < T_1$, χ_1'' does not appear (or may be quite small). When temperature is lowered further, χ_1'' begins to form a single peak. From the

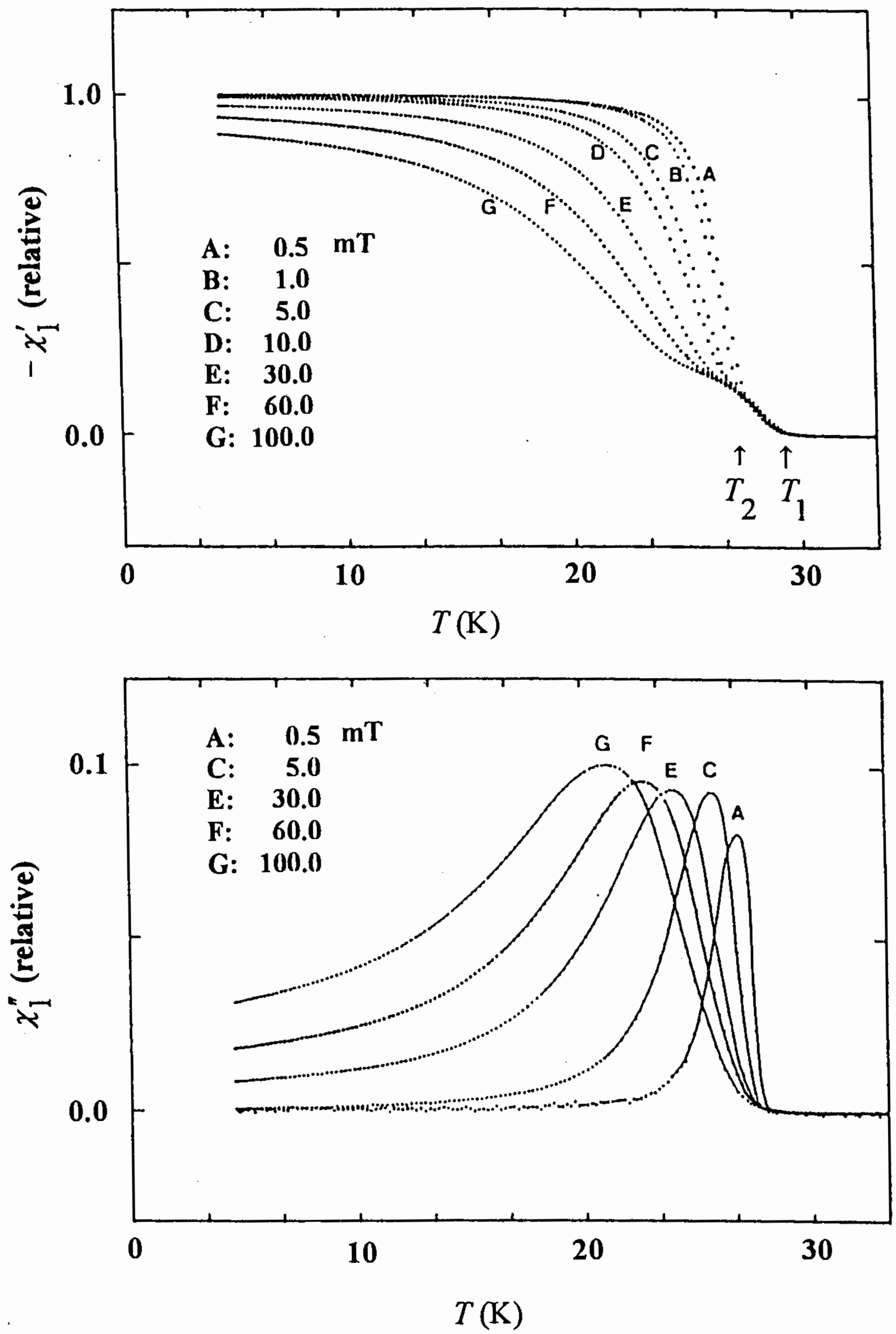

FIG. 4.4. Typical temperature dependence of the fundamental susceptibility (a) $-\chi_1'$ and (b) χ_1'' of sintered $La_{1.9}Sr_{0.1}CuO_4$, where $f = 132$ Hz [108].

results, they suggested that with decreasing temperature a fairly solid superconducting phase first appears at $T = T_1$. Then, at $T = T_2$, these superconducting grains begin to couple through any kind of weak-link junctions. If so, χ_1'' in the region $T_2 < T < T_1$ should have a nonzero value due to the eddy current loss in the grains, and the peak of χ_1'' at $T < T_2$ is certainly caused by the hysteresis loss. In fact, by expanding the data, they confirmed very small signals of χ_1'' due to the eddy current loss in the region $T_2 < T < T_1$. These findings are now well known as the *intragrain* component and the *intergrain coupling* component.

In Fig. 4.5, we show another typical $\chi_1 - T$ profile observed for sintered $Y_{0.8}Ca_{0.2}Ba_2Cu_3$-$O_{7-\delta}$ [109]. As seen in the figure, the real component χ_1' draws somehow distorted curve. The profile is apparently reflected on the imaginary component χ_1'' which shows several peaks. This example evidently tells us that the sample contains plural superconducting phases, which are very difficult to distinguish from resistivity measurements.

Different from sintered samples, single-crystal specimens do not involve the intergrain coupling phase. Therefore, χ_1'' due to the coupling phase does not appear. Note that in this case, the onset temperatures of χ_1' and χ_1'' are the same (see Fig. 4.6).

As demonstrated above, the measurement of χ_1 is a very effective tool for examinations of the sample quality. Noteworthy is that χ_1' can determine precisely the onset temperature of the superconducting transition, which is rather undefined from resistive measurements. All the samples used in the present work were previously examined in terms of χ_1.

In contrast to χ_1, the temperature dependence of higher-harmonic susceptibilities generally show very complicated profiles reflecting a slight distortion of the magnetization curve, but their physical meanings are scarcely illuminated. However, due to this complexity, they could be applicable, for example, for examinations of the material parameters k and B_0 involved in the KA model. Details on this topic will be discussed in Sec. III of this chapter.

Here, we first show some typical $\chi_n - T$ curves for sintered and single-crystal samples. In Fig. 4.7, are shown χ_2, χ_3, χ_5, and χ_7 versus T observed for sintered $YBa_2Cu_3O_{7-\delta}$ (Y123) [109]. The figures demonstrate that in the temperature region above 40 K, there exists apparently nonlinearity in the $M(\omega t)$ curves and especially nonzero signals of χ_2 indicate that $M(\omega t)$ has the asymmetric nature caused by H_{dc}.

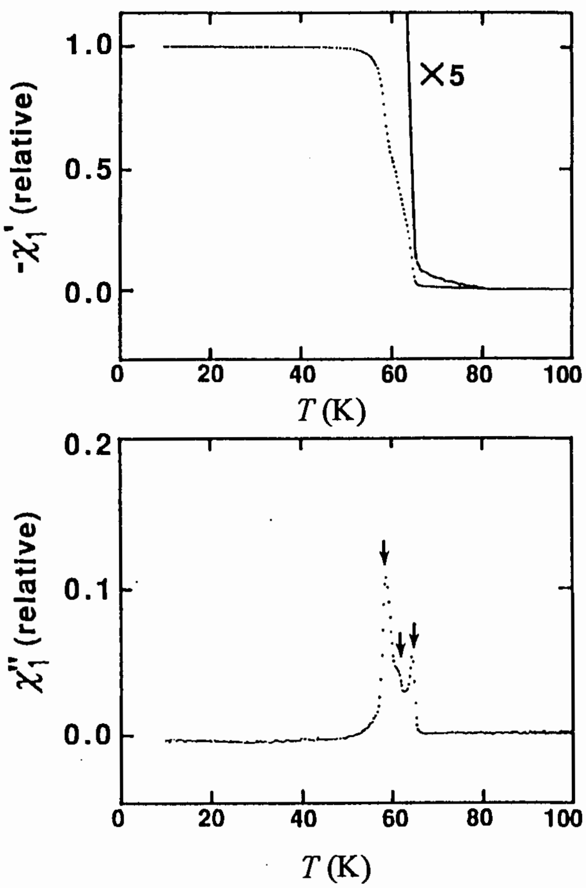

FIG. 4.5. Real ($-\chi_1'$) and imaginary (χ_1'') components of χ_1 versus temperature T for a Ca-substituted superconductor with a nominal composition $Y_{0.8}Ca_{0.2}Ba_2Cu_3O_{7-\delta}$, where $\mu_0 H_{ac} = 0.01$ mT and $f = 132$ Hz [109]. The sample contains superconducting impurity phases as is evident by plural peaks in χ_1'' (indicated by arrows).

The profiles of $\chi_n - T$ for a single-crystal specimen is somehow different from Fig. 4.7. In Fig. 4.8, we show χ_1, χ_3, χ_5, and χ_7 versus T of a single-crystal Y123 thin film [111]. The behaviors of χ_5 and χ_7 are very peculiar compared with those of the sintered Y123. Detailed discussion on this topic are presented in Chap. 5.

By analyzing these $\chi_n - T$ profiles with an appropriate model, one can extract various interesting informations on the sample used.

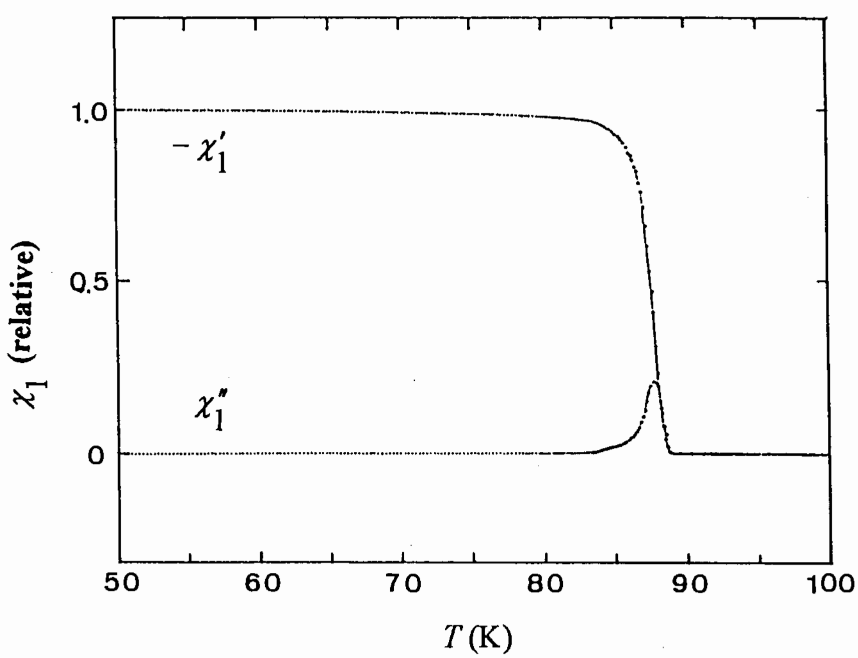

FIG. 4.6. Typical temperature dependence of the fundamental susceptibility of a single-crystal Y123 thin film in an applied field perpendicular to the film surface, where $\mu_0 H_{ac} = 0.01$ mT and $f = 132$ Hz [110].

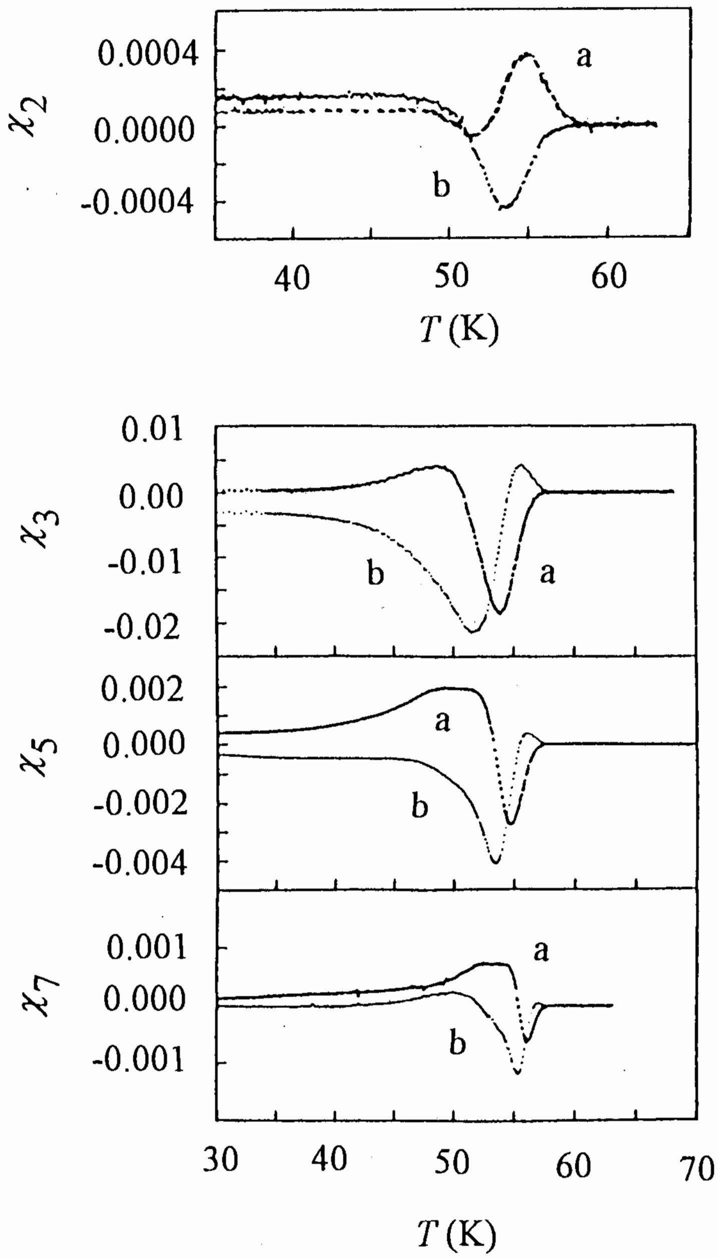

FIG. 4.7. χ_n ($n = 2, 3, 5, 7$) versus T of Fe-doped Y123 prepared by sintering. $\mu_0 H_{ac} = 0.01$ mT and $f = 132$ Hz [29, 106]. (a) is the real component and (b) is the imaginary component.

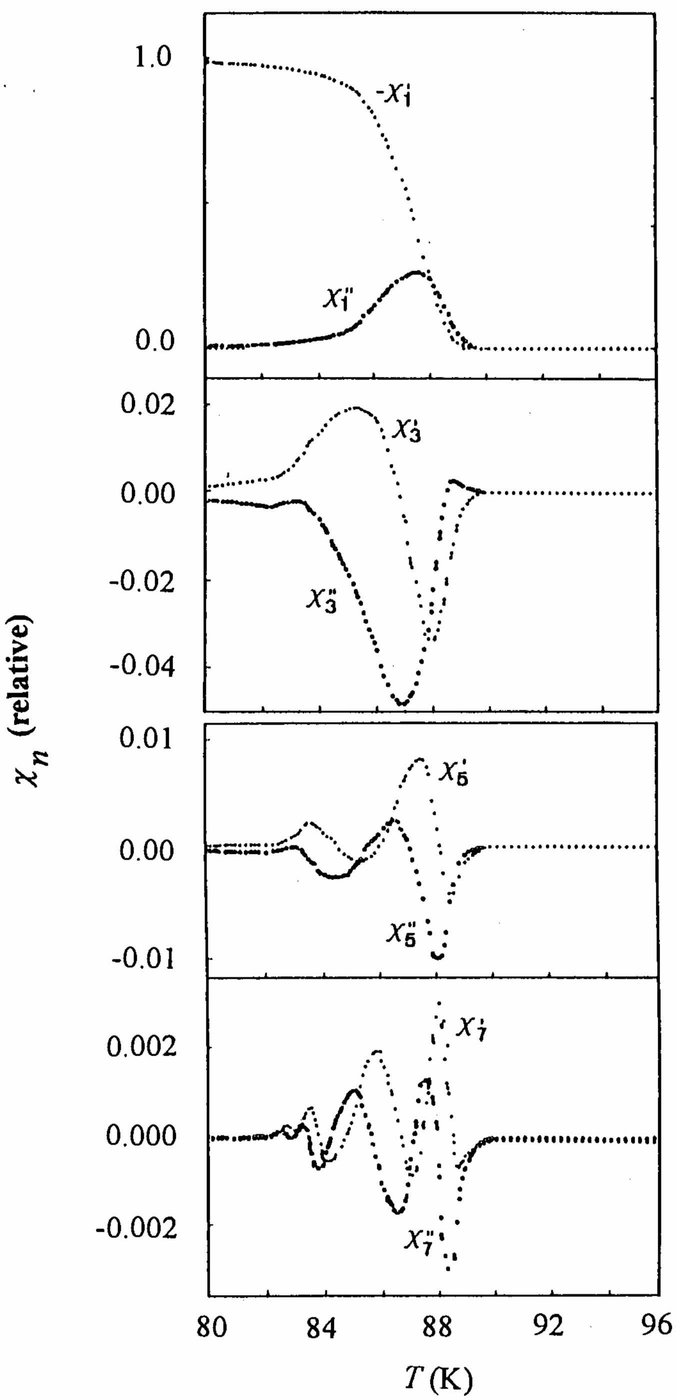

FIG. 4.8. χ_n ($n = 1, 3, 5, 7$) versus T of a single-crystal Y123 thin film, where $\mu_0 H_{ac} = 0.1$ mT and $f = 132$ Hz [111].

C. Analyses of χ_n by the Kim–Anderson Model

When the sample magnetization $M(\omega t)$ is expressed by Eq. (4.1), the real and imaginary components of χ_n can be calculated by

$$\chi_n' = \frac{1}{\pi H_{ac}} \int_0^{2\pi} M(\omega t)\cos(n\omega t)d(\omega t), \tag{4.7}$$

$$\chi_n'' = \frac{1}{\pi H_{ac}} \int_0^{2\pi} M(\omega t)\sin(n\omega t)d(\omega t). \tag{4.8}$$

Therefore, using the appropriate magnetization equation $M(\omega t)$, we can evaluate χ_n' and χ_n''.

In a series of investigations of magnetic properties of polycrystal oxide superconductors immersed in an ac magnetic field superimposed on a dc field, Yamamoto *et al.* [29–31] extensively applied the KA model and found that the magnetization equations based on this model can qualitatively well reproduce the observations.

However, since no clear expressions for the temperature-dependent material parameters k and B_0 involved in the KA model have been reported, in their previous studies [29, 30], it is assumed that $k(T/T_c) = k(0)(1 - T/T_c)^{3/2}$ and B_0 is a constant. The expression for $k(T/T_c)$, which is considered to reflect the pinning force in a specimen [112, 113] is based on the fact that when $B_i = 0$, k is proportional to the critical-current density, and for a tunnel junction, $J_c \propto (1 - T/T_c)^{3/2}$ at temperatures near T_c. As to B_0, several interpretations have been reported [18, 19, 113]. Phenomenologically, B_0 is supposed to be the self-field in zero applied field [113]. From observed magnetization curves, Kim, Hempstead, and Strnad [112] suggested that B_0 coincides approximately with the thermodynamic critical field. According to Anderson [19], B_0 is ascribed to the fact that the bundle of flux lines cannot contain less than a flux quantum ϕ_0, implying that B_0 would be assigned to an average flux density of a single vortex [19]. Under these indefinite circumstances, Yamamoto *et al.* tentatively treated B_0 as a constant [29, 30].

It should be noticed that in their study, the effects of surface barriers ΔH and lower critical fields H_{c1} were not taken into consideration. This approximation would be reasonable because both ΔH and H_{c1} are practically neglected for polycrystalline samples [31]. Successful simulations by Yamamoto *et al.* [29–31] using the KA model ($\Delta H = H_{c1} = 0$) indirectly justify this approximation. Therefore, in the following discussion for a melt-processed polycrystalline sample, we use the magnetization equations derived from the KA model. More details on the contribution of ΔH and H_{c1} on χ_n profiles will be discussed in Chap. 5.

III. MATERIAL PARAMETERS IN THE KIM–ANDERSON MODEL

For more elaborate applications of the KA model, it is desired to find reasonable forms of $k(T)$ and $B_0(T)$. The most pertinent method to determine the expressions is to measure the magnetization curves of a specimen at various temperatures below T_c and to search appropriate values of k and B_0 at each temperature so as to give the best fit to the observed full-hysteresis curves. This method is certainly effective at T far below T_c, because the magnetization curves $M(H)$ show a large hysteresis in that temperature region. On the contrary, at T very near T_c, derivations of $k(T)$ and $B_0(T)$ from the magnetization curves become difficult due to the small hysteresis. Therefore, at temperatures near T_c, it is preferable to employ any other quantity which is sensitive against a change in temperature.

As one of such candidates, higher-harmonic susceptibilities $\chi_n = \chi_n' - i\chi_n''$ $(n \geq 2)$ seem to be useful, because they exhibit complicated but very sensitive variations in the temperature region of the superconducting transition. By means of a Fourier analysis of observed χ_n, we can extract the isothermal magnetization curves near T_c.

To determine the forms of $k(T)$ and $B_0(T)$, we carry out two kinds of measurements. First is the direct measurement of $M(H)$ at relatively low temperatures below T_c. Second is measurements of χ_n at temperatures very near T_c and then $M(H)$ is evaluated from the Fourier series of χ_n. The samples used are *melt-processed* Y123 [114–118]. The reason for choosing the melt-processed Y123 samples is that Y123 fabricated by this method contains very few weak links and shows typical characteristics of a type-II superconductor. Theoretical reproduction of the magnetization curves is carried out using k and B_0 as the fitting parameters. Discussions on the origin of these parameters are also given.

A. Experimental

(1) Sample Preparation

For examinations of the critical state of the specimen, the importance is a homogeneous dispersion of the pinning centers in the sample. Murakami *et al.* [116, 117] reported the magnetization of Y123 prepared by the quench and melt growth (QMG) process obeys the Bean model. In fact, they found that the difference between the magnetization in the increasing and decreasing magnetic fields is proportional to the sample thickness. By means of a transmission electron microscope, they also confirmed that in the melt-textured samples, very few weak links were contained and the normal Y_2BaCuO_5 (Y211) phase which acts as the pinning center was finely and homogeneously distributed in the whole sample [116].

In the QMG process, to achieve a homogeneous distribution of the Y211 phase, the quenching temperature should be as high as 1200 – 1500 °C. As a more convenient method without the quenching treatment at such high temperatures, the platinum-doped melt-growth (PDMG) method has been proposed [26]. In this method, Pt doping (less than 1 wt.%) causes a homogeneous distribution of the submicron Y211 particles. Since the reproducibility of the sample quality was satisfactory, in this section, we adopted the PDMG method.

Y_2O_3, $BaCO_3$, and CuO powders were mixed in the ratio of Y:Ba:Cu=1.2:2.1:3.1 and the mixture was calcined at 900 °C for 12 h in air. It was ground and mixed with Pt powder of 1 wt.%. The pelletized mixture (3.5 mm × 3.0 mm × 1.0 mm) was quenched from 1150 °C. Then it was kept at 1100 °C for 20 min and was cooled down from 1000 °C to 940 °C in the rate of 2 °C/h in air. Finally, it was annealed at 600 °C for 24 h in flowing oxygen. We prepared four samples by the same procedure. The superconducting transition of these samples was carefully examined in terms of χ_1. T_c (onset temperature) of samples 1 – 4 were 92.8, 91.9, 92.9, and 91.5 K, respectively. The structural quality was examined by means of scanning electron microscope and powder x-ray diffraction patterns. From the results, we found the superconducting and structural characteristics of samples 1 – 4 were practically very similar to each other. Therefore, to carry out two kinds of measurements with different instruments, we used samples 1 – 3 for direct measurements of the $M(H)$ curves and sample 4 for measurements of χ_n as a function of temperature.

(2) Measurements of χ_n and Fourier Analysis

At temperatures $T/T_c \leq 0.98$, conventional measurements of $M(H)$ curves were made for samples 1 – 3 with a superconducting quantum interference device (SQUID). To mount the sample in a capsule of SQUID, it was cracked to pieces less than 1 mm in diameter.

At temperature $T/T_c > 0.98$, indirect derivations of the magnetization curves were carried out for sample 4 through analyses of complex susceptibilities χ_n ($n = 1, 2, 3, 5$). Here the relative values of χ_4 and χ_n for $n \geq 6$ were so small that we neglected them. The amplitude of the ac magnetic field $\mu_0 H_{ac}$ in units of teslas was in the range 0.1 – 0.2 mT and the fundamental frequency f was in the range 55 – 268 Hz, where $\mu_0 = 4\pi \times 10^{-7}$ H/m.

Substituting the observed values of χ_n' and χ_n'' at a specified temperature into Eq. (4.1), we obtain $M(\omega t)$ at that temperature. To trace $M(\omega t)$ as a function of the applied ac field, one period of $H_{ac}\cos(\omega t)$ $(0 \leq \omega t \leq 2\pi)$ was divided into 360 regular intervals, and $M(\omega t)$ was numerically obtained at each point. Thus we can draw the isothermal $M(H)$ loop derived from the χ_n series.

B. Results and Discussion

(1) Magnetization Curves

In Fig. 4.9, we show typical $M(H)$ curves of sample 1 measured by SQUID at $T/T_c = 0.22$ (20 K), 0.43 (40 K), and 0.65 (60 K). The hysteretic behavior evidently comes from flux pinning [116, 119, 120] and the decrease of the magnetization becomes remarkable at higher temperatures. Simulations of the observed $M(H)$ curves given in Fig. 4.9 were made using the appropriate magnetization equations derived within the construct of the KA model, where $k(T/T_c)$ and $B_0(T/T_c)$ were used as the fitting parameters. We found that the calculated magnetizations were about 1.6 times larger than the observed ones at any temperature, probably due to the demag-

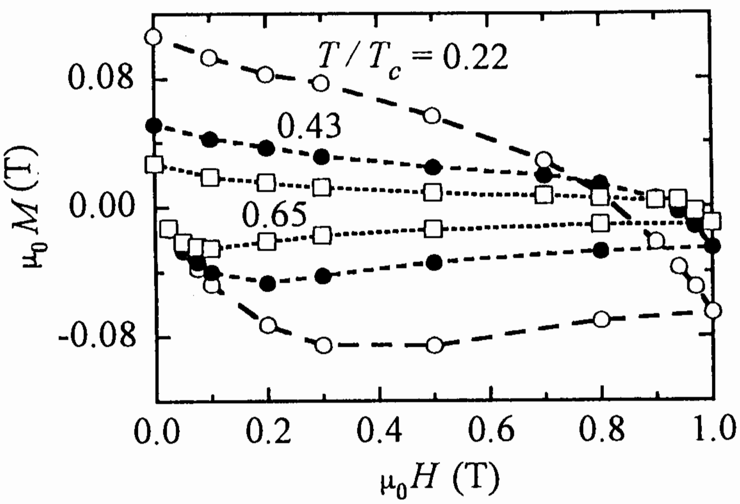

FIG. 4.9. Magnetization curves of sample 1 at $T/T_c = 0.22$ (open circles), 0.43 (closed circles), and 0.65 (open squares) measured by SQUID.

netization effect of the fractional sample. Therefore, the calculated results were corrected by a factor of 1/1.6. Assuming that this factor is simply caused by the demagnetization effect, the demagnetization factor of sample 1 is estimated to be 0.38. The calculated results thus obtained are shown in Figs. 4.10(a) – (c). The open circles in the figures are experimental points. The values of k and B_0 adopted are $k = 1.15 \times 10^9$ N/m^3 and $B_0 = 0.77$ T in Fig. 4.10(a), 2.8×10^8 N/m^3 and 0.347 T in Fig. 4.10(b), and 7.9×10^7 N/m^3 and 0.18 T in Fig. 4.10(c). We find the theoretical curves reproduce the data pretty well.

When the sample temperature further increases, the magnetization profile appears in somehow different manner. For example, as shown in Fig. 4.11, the $M(H)$ curve of the sample 3 at $T/T_c = 0.92$ (85 K), shows no hysteresis any more above $\mu_0 H = 0.48$ T, implying that J_c is almost zero due to the flux creep or the vortex-lattice melting or the vortex glass-liquid transition in that field region [121–123]. From this result, we find the irreversibility field $\mu_0 H_{irr}$ is 0.48 T for $T/T_c = 0.92$. For such a partially reversible $M(H)$ curve observed at higher temperatures, simulations were made only in the low field region where the irreversibility remains sufficient. The irreversibility properties are discussed below. Table 4.1 lists the values of k and B_0 for samples 1 – 3 thus determined from the $M(H)$ curves measured by SQUID in the temperature region $T/T_c = 0.05 - 0.98$.

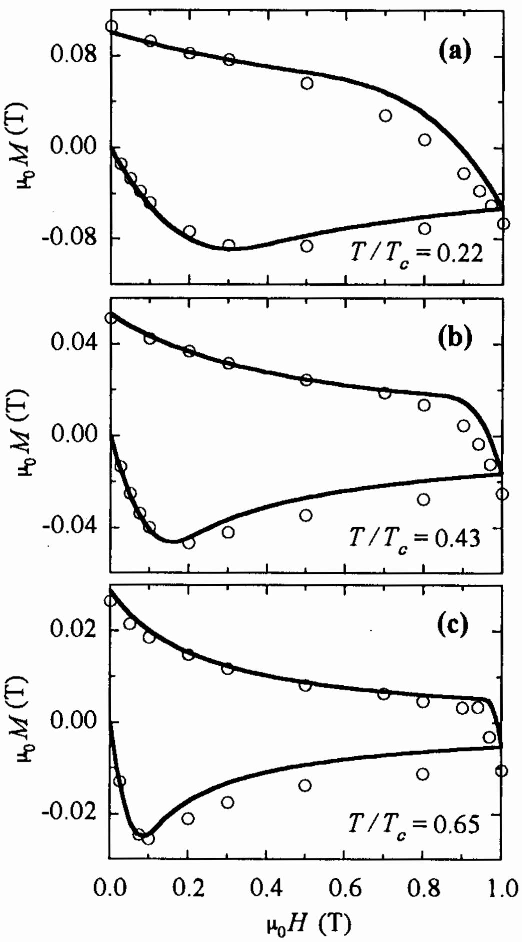

FIG. 4.10. Magnetization curves of sample 1 at (a) $T/T_c = 0.22$, (b) 0.43, and (c) 0.65. Solid lines represent the calculated results and open circles are the observed data.

TABLE 4.1. Material parameters k and B_0 of samples 1, 2, and 3.

T (K)	T/T_c	k (10^8 N/m^3)			B_0 (T)		
		Sample 1	Sample 2	Sample 3	Sample 1	Sample 2	Sample 3
4.2	0.05		30	60		3.0	3.7
20	0.22	11.5	5.0		0.77	0.7	
30	0.32	5.9		3.8	0.52		0.3
40	0.43	2.8	2.0	2.2	0.347	0.52	0.19
50	0.54	1.45		1.8	0.245		0.38
60	0.65	0.79	0.75		0.18	0.26	
70	0.75		0.4	0.5		0.225	0.18
77	0.84		0.15			0.11	
80	0.86			0.18			0.073
85	0.92			0.04			0.027
90	0.97			0.003			0.0105
91	0.98			0.0007			0.0045

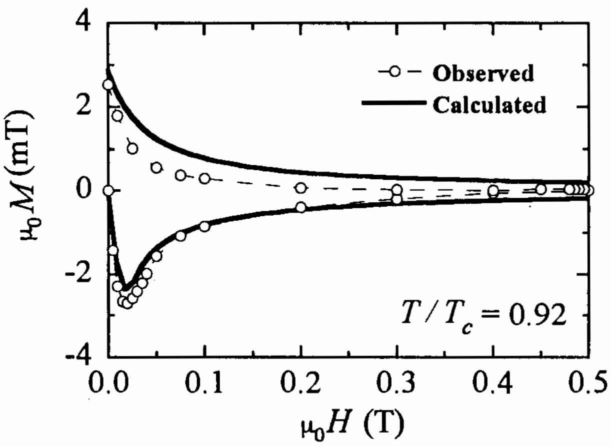

FIG. 4.11. Magnetization curves of sample 3 at $T/T_c = 0.92$. Solid line is the calculated results and open circles are the observed data.

For temperatures $T/T_c > 0.98$, it is difficult to determine $k(T/T_c)$ and $B_0(T/T_c)$ from direct measurements of the $M(H)$ curves by SQUID. For this reason, at $T/T_c > 0.98$, we measured the fundamental and higher-harmonic susceptibilities χ_n as a function of temperature and then deduced $M(H)$ by the Fourier analysis. Using sample 4, the frequency dependence of χ_n was first examined for the applied field $H(\omega t) = H_{dc} + H_{ac}\cos(\omega t)$ with $f\ (= \omega/2\pi) = 55$, 132, and 268 Hz, but no appreciable dependence of χ_n on f was found within the limit of experimental errors. This result suggests that a flux flow and/or a flux creep by thermal activation expected near T_c cannot be observed under such a small applied field used here. Further measurements were therefore carried out using $f = 132$ Hz. As typical observations, in Figs. 4.12(a) – (d), we show χ_n ($n = 1, 2, 3, 5$) as a function of temperature, where $\mu_0 H_{ac} = 0.2$ mT and $f = 132$ Hz.

In Figs. 4.13(a) – (d), the open circles represent the $M - H$ relations of sample 4 at $T/T_c = 0.992, 0.993, 0.994$, and 0.995, respectively, deduced by using observed χ_n in Eq. (4.1). Theoretical simulations of the $M(H)$ profiles were performed, and the parameters k and B_0 for the sample at each temperature were selected so as to give the best fit to the deduced $M(H)$. We found that the correction factor due to the demagnetization effect is 1/1.4 for sample 4. The solid lines shown in Figs. 4.13(a) – (d) are the calculated loops thus obtained, where χ_0 in Eq. (4.1) was tentatively replaced by χ_1', the real part of the fundamental susceptibility. This replacement seems to be pertinent because χ_1' empirically agrees very well with the dc susceptibility measured by SQUID in the zero-field cooling process.

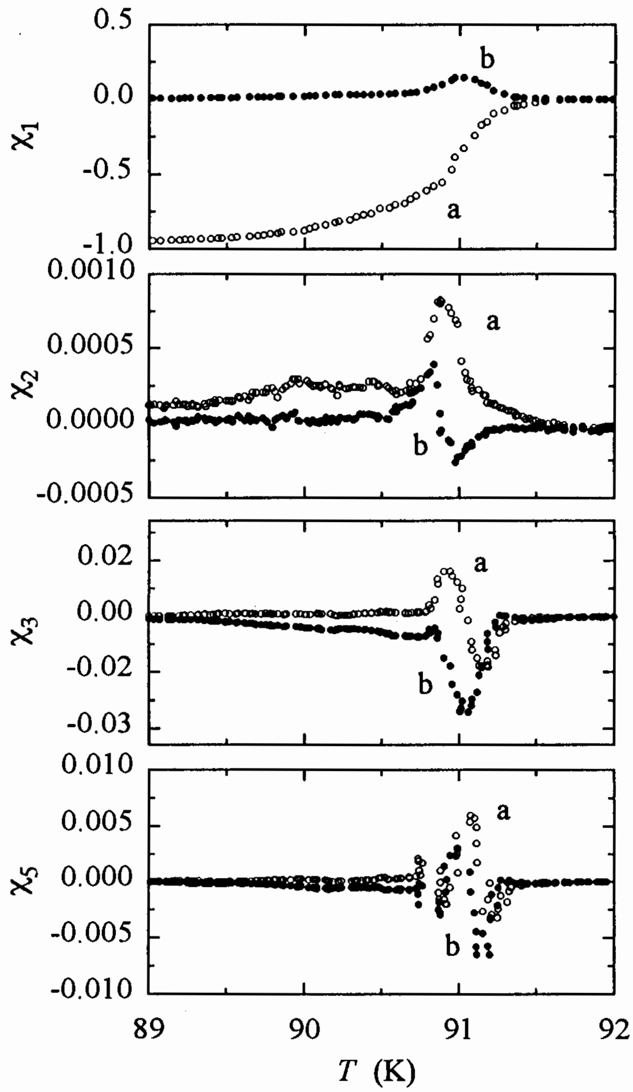

FIG. 4.12. Observed χ_n ($n = 1, 2, 3, 5$) versus T for sample 4, where $\mu_0 H_{ac} = 0.2$ mT and $f = 132$ Hz. (a) is the real component and (b) is the imaginary component. Data are normalized to the saturated value of $|\chi_1'|$.

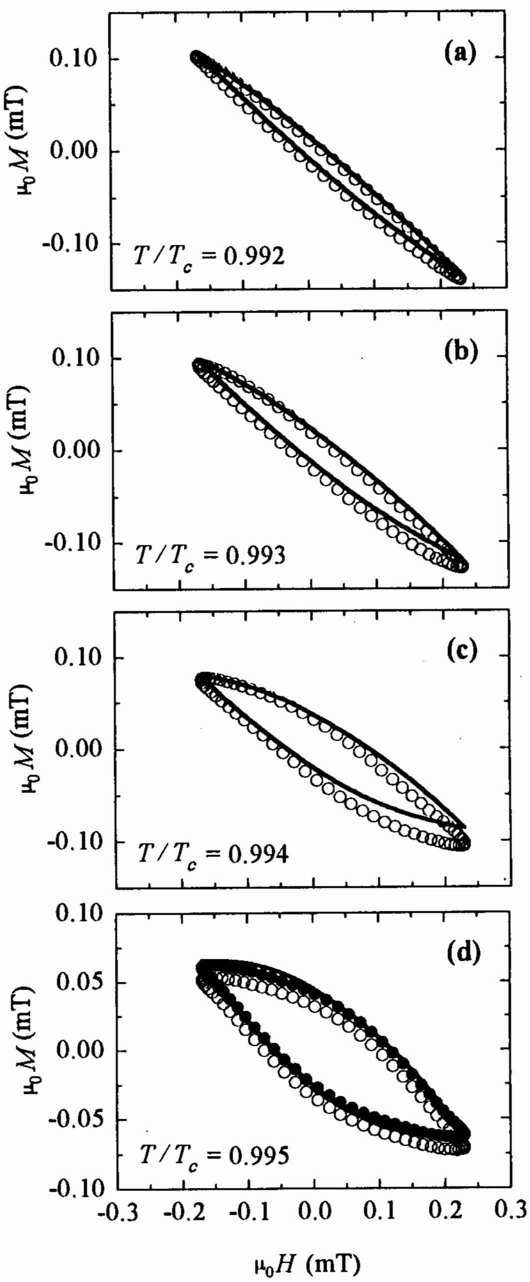

FIG. 4.13. Experimental and calculated magnetization curves at (a) $T/T_c = 0.992$, (b) 0.993, (c) 0.994, and (d) 0.995. Open circles represent the experimental results obtained from observed χ_n ($n = 1, 2, 3, 5$) using Eq. (4.1). Solid lines are the results calculated by the KA model. Closed circles in (d) represent the experimental loop estimated for $\chi_0 = 0$.

TABLE 4.2. Material parameters k and B_0, and full-penetration fields H_p of sample 4.

T (K)	T/T_c	k (N/m^3)	B_0 (mT)	$\mu_0 H_p$ (mT)
90.77	0.992	500	0.70	0.84
90.86	0.993	300	0.65	0.60
90.95	0.994	150	0.59	0.34
91.04	0.995	100	0.55	0.27

However, as seen in Fig. 4.13, when temperature increases, some up-down discrepancy appears between the observed loop (open circles) and the calculated loop (solid lines). This discrepancy probably comes from the replacement of χ_0 by χ_1'. As a matter of fact, χ_0 varies depending on the relative magnitude of the full-penetration field $H_p(T/T_c)$ and the applied field H. When $H \gg H_p$, χ_0 tends to become zero because $|M|$ has the maximum value at $|H| \leq H_p$ in the initial magnetization curves [20, 28]. As listed in Table 4.2, $\mu_0 H_p$ becomes smaller as temperature increases and in this region, χ_0 should be much smaller than χ_1' [124]. In fact, as shown in Fig. 4.13(d), if we use $\chi_0 = 0$ at $T/T_c = 0.995$, the discrepancy between the observed loop (closed circles) and the calculated loop (solid lines) almost vanishes.

(2) Parameter k

In the critical-state model, the Lorentz force $\boldsymbol{J} \times \boldsymbol{B}$ imposed on a flux quantum is assumed to be balanced with the pinning force inside the specimen. Therefore, the material parameter k involved in Eq. (2.1) is considered to represent the pinning-force density. As listed in Tables 4.1 and 4.2, the temperature dependence of k determined by simulating the magnetization curves indicates that the pinning-force density becomes weaker with the ascent of temperature. We show in Fig. 4.14 double logarithm plot of k as a function of $1 - T/T_c$ for samples 1 – 4. In the wide region, we find

$$k(T/T_c) = k(0)(1 - T/T_c)^3. \quad (4.9)$$

Possible elements for the pinning center in oxide superconductors are normal-state particles, twin boundaries, oxygen vacancies, and dislocations. Among these, it has been pointed out that the normal-state Y211 particles act as one of the predominant pinning center for a melt-

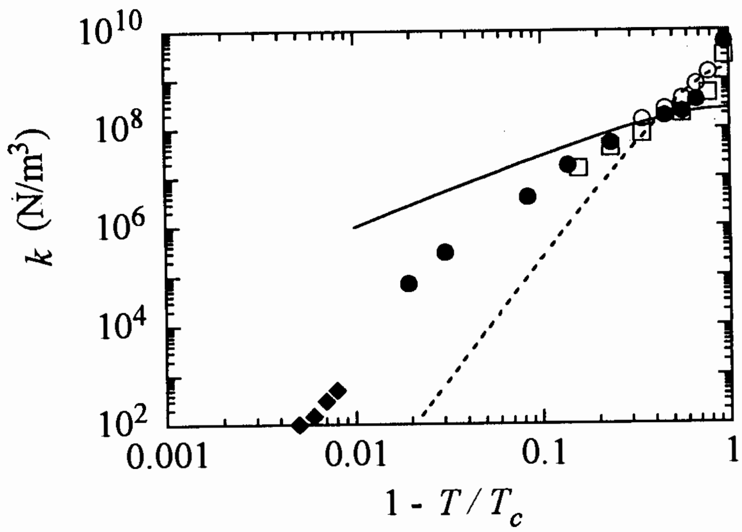

FIG. 4.14. Parameter k determined by fitting the $M(H)$ curves versus $1 - T/T_c$. Open circles, open squares, closed circles, and closed squares give k for samples 1, 2, 3, and 4, respectively. Solid line is the calculated k due to the normal-state pinning. Dashed line is the calculated k due to the weak and small defects.

processed Y123 [116, 125, 126]. The pinning-force density F_1 due to the normal-state particles of which radius is larger than the Ginzburg–Landau (GL) coherence length ξ can be approximately derived from the free-energy difference between the flux in the superconducting state and that in the normal state [127–129]. As far as the imposed magnetic field is low enough, F_1 is approximately given by

$$F_1 \quad = \quad N_1 B_c^2(T/T_c)\pi\xi(T/T_c)D/4\mu_0, \tag{4.10}$$

where N_1 is the density of the pinning centers, $B_c(T/T_c)$ is the thermodynamic critical flux density, and D is the radius of the normal-state particles. Assuming $B_c(T/T_c) \propto 1-(T/T_c)^2$ and $\xi(T/T_c) \propto (1-T/T_c)^{-1/2}$ [127], we evaluated F_1. The result is given by a solid line in Fig. 4.14.

Another important pinning center in oxide superconductors is the randomly distributed weak defects [130], for example, oxygen vacancies. When the radius of the vacancies r is much smaller than the GL coherence length in the CuO_2 layers $\xi_{ab}(0)$, the pinning-force density F_2 is given as

$$F_2 \quad \propto \quad N_2 B_c^4(T/T_c) r^4 \xi_{ab}^2(0)/16\xi_{ab}^2(T/T_c), \tag{4.11}$$

where N_2 is the density of vacancies [131–134]. Evaluated F_2 with the same temperature dependence of $B_c(T/T_c)$ and $\xi_{ab}(T/T_c)$ as in Eq. (4.10) is demonstrated by a dashed line in Fig. 4.14.

From Fig. 4.14, we see in the temperature region $0.2 < T/T_c < 0.6$ ($0.4 < 1 - T/T_c < 0.8$), k determined in the present study mostly lies around the dashed curve, suggesting that in that temperature region, the weak point defects play a predominant role as the pinning center. This trend is qualitatively consistent with the result by Matsushita *et al.* [135] who reported that from the critical current characteristics in a melt-processed Y123, the small point defects are the dominant pinning center in the low temperature region 25 K $< T <$ 60 K.

On the contrary, in the temperature region $T/T_c > 0.6$ ($1 - T/T_c < 0.4$), k has the values between the solid and dashed lines. This suggests that in the higher temperature region, the pinning-force density k may be enhanced due to an additional contribution from the normal-state Y211 particles. The pinning properties discussed here are consistent with the results reported by other groups [126, 128, 135].

(3) Parameter B_0

The temperature dependence of B_0 listed in Tables 4.1 and 4.2 shows that the quantity decreases with the increase of temperature. This implies that the field dependence of J_c becomes sensitive at higher temperatures. In Fig. 4.15, we show double logarithm plots of B_0 for samples $1-4$ as a function of $1 - T/T_c$. The straight line in the figure gives

$$B_0(T/T_c) = B_0(0)(1 - T/T_c)^{3/2}. \tag{4.12}$$

The temperature dependence of B_0 has been discussed by several groups. Anderson [19] proposed that B_0 corresponds to the minimum magnetic flux density of a flux bundle, although the bundle size possibly fluctuates and this makes difficult to confirm his proposal. Yamamoto *et al.* [136] considered that the bundle radius can be approximated by the London penetration depth $\lambda(T/T_c)$ and attempted to reproduce the temperature dependence of higher-harmonic complex susceptibilities of a single-crystal Y123 bulk sample, where they assumed $B_0(T/T_c) = \phi_0/\pi\lambda^2(T/T_c) = B_0(0)[1 - (T/T_c)^4]$ from two-fluid approximation. However, the

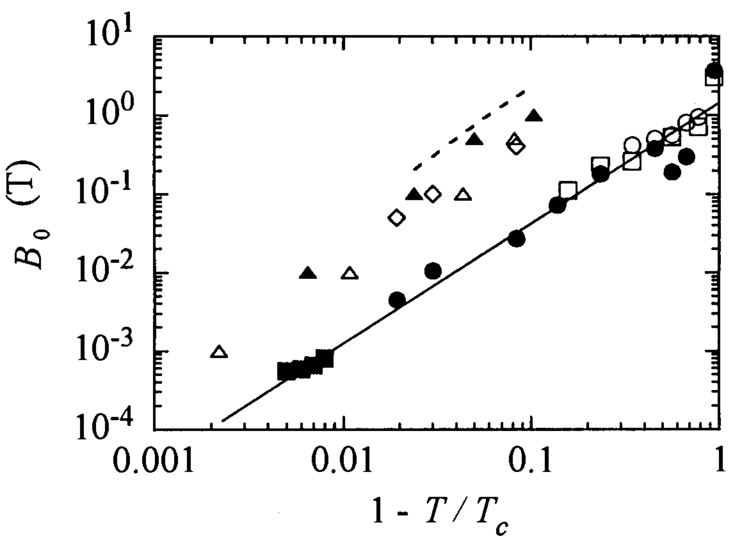

FIG. 4.15. Parameter B_0 determined by fitting the $M(H)$ curves versus $1 - T/T_c$. Open circles, open squares, closed circles, and closed squares represent B_0 for samples 1, 2, 3, and 4, respectively. Open triangles, closed triangles, and open diamonds are the irreversibility flux density B_{irr} of samples 1, 2, and 3, respectively. Dashed line represents the depinning flux density B_d taken from Ref. 140. Solid line represents the power relation $B_0 \propto (1 - T/T_c)^{3/2}$.

observed temperature dependence is different from their assumption. Besides, if the bundle radius corresponds to $\lambda(T/T_c)$, B_0 should be of the order of the lower critical field $\mu_0 H_{c1}$, because H_{c1} is related to $\lambda(T/T_c)$ as $\mu_0 H_{c1} = (\phi_0/4\pi\lambda^2)(\ln\kappa + 0.5)$, where κ is the GL parameter and for Y123, κ is of the order of 10^2 [75]. Empirically, $\mu_0 H_{c1}$ for polycrystal Y123 at 4.4 K is about 0.05 T [37], and this value is apparently much smaller than B_0 (4.2 K) given in Table 4.1.

It is interesting to note that the temperature dependence found here is similar to that of the irreversibility field $\mu_0 H_{irr}$. Many workers reported that $\mu_0 H_{irr}$ of a Y123 bulk specimen is approximately proportional to $(1 - T/T_c)^{3/2}$ [20, 121, 137–139]. Gupta *et al.* [140] directly observed the depinning field $\mu_0 H_d$, being proportional to $(1 - T/T_c)^{3/2}$ (shown by a dashed line in Fig. 4.15). Thereupon, we plotted $\mu_0 H_{irr}$ of the present samples 1 – 3 obtained from the $M(H)$ hysteresis curves in Fig. 4.15. The results show a similar temperature dependence to B_0, although the value of $\mu_0 H_{irr}$ is about tenfold of B_0. These findings strongly suggest that B_0 used as a material parameter in the KA model physically correlates to $\mu_0 H_{irr}$. In fact, in an extreme case of the KA model with $B_0 \gg |B_i|$, the so-called linear model, Eq. (2.1) can be approximately given by $J_c(B_i) = k/B_0 - (k/B_0^2)|B_i|$, and in this case, from the definition of $\mu_0 H_{irr}$ ($J_c = 0$ at $|B_i| = \mu_0 H_{irr}$), B_0 becomes equal to $\mu_0 H_{irr}$ [141].

The irreversibility line is interpreted by the several ways; a flux creep, a vortex-lattice melting, and a vortex glass-liquid transition. In each model the boundary field H_b is deduced with the approximate relation $H_b \propto (1 - T/T_c)^n$ near T_c. Yeshurun and Malozemoff [121] and Malozemoff *et al.* [137] derived $n = 3/2$ using the thermally activated flux-creep model [19, 142]. Houghton *et al.* [143] gave $n = 2$ for the melting line using the Lindemann criterion [144] in the framework of the vortex lattice model [145] for elastic moduli [146–149]. Fisher [150] pointed out that a vortex glass-liquid transition occurs in the sample including weak random point defects which are used in the present work. For that transition $n = 4/3$ was reported [151]. As far as the value of n is concerned, the present result supports the flux creep model. However, this we may not conclude with confidence because the above theoretical values of n are derived for temperatures near T_c.

The correlation between the irreversibility field and the pinning property is interesting. Worthington *et al.* [152] pointed out that the irreversibility comes from the vortex-lattice melting since the irreversibility line is not affected by the defect density introduced by heavy ion

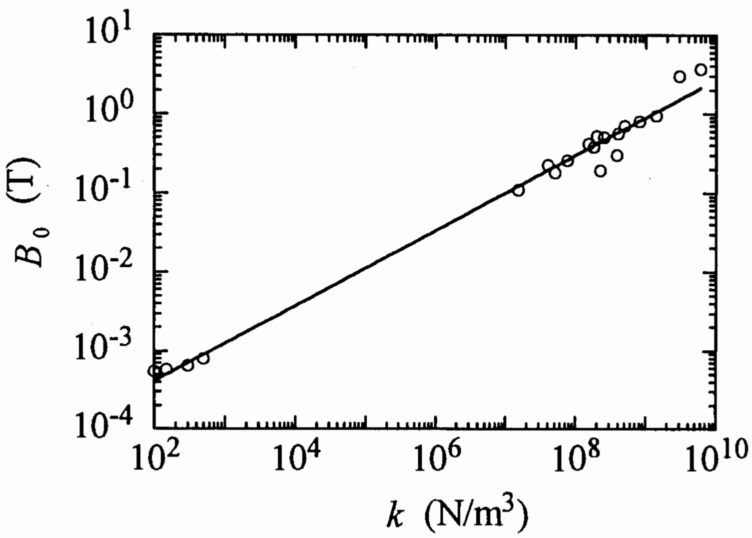

FIG. 4.16. B_0 versus k. Solid line represents the power relation $B_0 \propto k^{1/2}$.

irradiation. On the contrary, a strong enhancement of the irreversibility field has been reported for the sample containing columnar defects [153–155]. Upon this we plot B_0 ($\propto \mu_0 H_{irr}$) as a function of k as shown in Fig. 4.16. From the figure, we find the relation $B_0 \propto k^{1/2}$ over the wide temperature region. This relation was also reported by Cody and Cullen [156]. The result suggests that the irreversibility nature is affected by the pinning properties. Further studies of the $k - B_0$ relation for various samples are needed.

IV. CONCLUSIONS

We have presented the details of the measurement of complex ac susceptibilities χ_n ($n = 1,2,3,\ldots$). The measurement of the fundamental susceptibility χ_1 is a very effective tool for examinations of the sample quality. The temperature dependence of higher-harmonics susceptibilities χ_n ($n \geq 2$) generally show very complicated profiles reflecting a slight distortion of the magnetization curve, but their physical meanings are scarcely illuminated. By analyzing these $\chi_n - T$ profiles with the critical-state model, one can extract various interesting informations on the sample.

The isothermal magnetization curves of melt-processed Y123 were measured in the temperature region 4.2 K$-T_c$. By fitting the observed curves using the magnetization equations based on the KA critical-state model, the temperature dependence of the material parameters k and B_0 were obtained. The $k(T)$ behavior indicates that at lower temperatures below T_c, the weak point defect (oxygen vacancies) plays a predominant role as the pinning center, but at higher temperatures near T_c, the normal-state Y211 particles take part in the contribution to pinning. The parameter B_0 of which the physical meaning has been ambiguous, showed a very similar temperature-dependence to that of the irreversibility field $\mu_0 H_{irr}$. In fact, in an extreme case $B_0 \gg |B_i|$, B_0 becomes equal to $\mu_0 H_{irr}$. This strongly suggests that B_0 is a closely correlated quantity to the irreversibility phenomenon.

Chapter 5

Surface Barriers of $Bi_2Sr_2CaCu_2O_{8+\delta}$ and $YBa_2Cu_3O_{7-\delta}$ Single Crystals

I. INTRODUCTION

In the initial magnetization of type-II superconductors, we realize that the applied magnetic field is completely excluded due to the Meissner effect, as far as the field does not exceed the lower critical field H_{c1} of the specimen involved. When the applied field exceeds H_{c1}, flux penetration begins in the form of quantized vortices. Magnetization curves predicted by Abrikosov [9] on the basis of this concept have been largely verified by experimental results on bulk samples [157–159]. However, some of the results have shown a low-field hysteresis in the magnetization curve, suggesting the influence from the specimen surface [160]. This effect is called "*surface barriers*".

It has been known that there are two different physical origins of surface barriers ΔH; the geometrical barrier [36] and the Bean–Livingston (BL) barrier [33]. As briefly reviewed by Benkraouda and Clem [57], the geometrical barrier has been shown to delay the first penetration of magnetic flux into a flat superconducting strip subjected to a perpendicular magnetic field. A consequence of this effect is that such a strip exhibits hysteretic behavior even if the vortices in the interior of the strip are completely unpinned, i.e., even if the bulk critical current density J_c is zero. The geometrical barrier is due solely to the nonellipticity of the sample's cross section, being similar to the barrier observed in type-I superconductors of rectangular cross section. Meanwhile, the BL barrier, first introduced by Bean and Livingston [33], arises from the competing effects of an attractive interaction of the Abrikosov vortex to its "*mirror image*" near the surface and the repulsive interaction on the vortex from the applied field.

The understanding of vortex dynamics for cuprate-based oxide superconductors is undoubtedly very important and interesting, from both the viewpoints of fundamental researches and applications. Therefore, active investigations of ΔH for these materials have been carried out by employing a variety of methods [33–57]. For example, Zeldov *et al.* [48] have made theoretical description of vortex dynamics in the flat samples and have revealed that in perpendicular applied magnetic field the vortex penetration is delayed significantly due to the presence of a potential barrier of the geometrical origin. They argue that this geometrical-barrier effect results in hysteretic magnetization and in the existence of an irreversibility line in the absence of bulk pinning. In addition, to confirm this theoretical prediction, they observed field profiles in a $Bi_2Sr_2CaCu_2O_{8+\delta}$ (Bi2212) single crystal at various temperatures and added support to the predicted geometrical barrier which governs vortex penetration and dynamics.

Konczykowski *et al.* [70] measured the lowest field for flux penetration of untwined YBa_2-$Cu_3O_{7-\delta}$ (Y123) crystals near the transition temperature. They found that this field decreases linearly with increasing temperature but exhibits an anomalous change in the slope in close vicinity of the transition temperature. They also found that low-dose electron irradiation reduces drastically the field for flux penetration. To interpret these observations, they discussed the results in terms of the BL barrier which was proposed to be the origin for retardation in flux entry and for irreversible phenomena in the unirradiated crystals.

Generally speaking, experimental evaluations of ΔH from magnetization curves are not easy, because ΔH does not cause a notable distortion to magnetization curves but merely expands them up and down (see Chap. 2).

The time-dependent magnetization $M(\omega t)$ of a specimen for a magnetic field $H(\omega t) = H_{dc} + H_{ac}\cos(\omega t)$ can be generally expressed in the form of a Fourier expansion;

$$M(\omega t) = \chi_0 H_{dc} + H_{ac}\sum_{n=1}^{\infty} \mathrm{Re}[\chi_n \exp(in\omega t)]. \tag{5.1}$$

Re[ ] denotes the real part of a complex variable. H_{dc} is the dc magnetic field and H_{ac} is the ac field amplitude. Here we define the Fourier coefficients of the magnetization $\chi_n = \chi_n' - i\chi_n''$ $(n = 1,2,3,\ldots)$ as the harmonic ac susceptibilities, where χ_1 is the fundamental susceptibility and the others are the higher-harmonic susceptibilities. As described in Chap. 4, the higher-harmonic susceptibilities χ_n $(n \geq 2)$ show very complicated profiles, sensitively reflecting a non-linearity of magnetization curves.

The above discussion indicates that analyses of experimental χ_n using appropriate magnetization equations involving ΔH would provide a useful technique for evaluation of ΔH.

In fact, Yamamoto *et al.* [111] have studied the magnetic response of thin-film Y123 single crystals in terms of χ_n (n = 1, 3, 5, 7) and have analyzed the observed χ_n using the modified Bean model which includes ΔH. From the results, they suggest that ΔH plays an essential role in the magnetic response of these films.

Motivated by these previous investigations of ΔH, in this chapter, we attempt to measure ΔH of cuprate superconductors and to establish a research technique for ΔH in terms of higher-harmonic susceptibilities. Samples used for this purpose are Bi2212 and Y123 single crystals (thin film and bulk). We measured χ_n ($n = 1, 2, 3, 5, 7$) for these samples and analyzed observed χ_n using the magnetization equations derived from the modified Kim–Anderson (KA) model. In the analysis, we used the material parameters k and B_0, lower critical fields H_{c1}, and surface barriers ΔH as fitting parameters. Notable differences between ΔH's of the present samples have been revealed. Discussion about the origin of ΔH for each sample is also given.

II. EXPERIMENTAL

A. Sample Preparation

A thin-film Bi2212 single crystal (10 mm $\times$ 10 mm $\times$ 40 nm) was prepared by the radio-frequency magnetron spattering method [107] and T_c was 76.0 K. The film epitaxially grew with [0 0 1] axis normal to the (1 0 0) surface of the MgO single crystal. A thin-film Y123 single crystal (10 mm $\times$ 10 mm $\times$ 200 nm) was prepared by the activated evaporation method [110] and T_c was 88.9 K. A bulk Bi2212 single crystal (3.0 mm $\times$ 1.0 mm $\times$ 0.1 mm) was prepared by the self-flux method [14] and T_c was 85.0 K. A bulk Y123 single crystal (2.5 mm $\times$ 2.5 mm $\times$ 0.3 mm) was prepared by the flux method [136] and T_c was 92.0 K.

Details of sample preparations and their structural characterizations were previously reported [14, 107, 110, 136].

B. Measurements of χ_n

The measuring system of χ_n consisted of the Hartshorn bridge and the temperature control system. To avoid the bridge imbalance during one run of the experiment, the sample coil was directly immersed in a liquid-N_2 or liquid-He bath. Phase setting of the lock-in amplifier was carefully made so as to give variation only to the in-phase signals, against the change in the bridge inductance. The ac magnetic field $H_{ac}\cos(\omega t)$ was applied to the sample using a function generator, where the applied ac field is parallel to the c axis.

For measurements of higher-harmonic susceptibilities χ_n ($n \geq 2$), the device was modified, where two function generators were used. The ac magnetic field was applied using one generator F-1 and the other generator F-2 was used to supply the nth-harmonic sinusoidal wave synchronized with F-1. In this experiment, magnetic shielding was not used, and so the applied ac field was superimposed on the Earth's field $\mu_0 H_{dc} = 0.03$ mT, where $\mu_0 = 4\pi \times 10^{-7}$ H/m. We used $\mu_0 H_{ac} = 0.01 - 0.18$ mT and $f = 132$ Hz. Details of the measuring system were described in Sec. II of Chap. 4.

In Fig. 5.1, we show χ_1 as a function of temperature T. The onset of the real and imaginary components begins at the same temperature. This means that very few weak couplings are involved in the samples. Besides, a single peak of χ_1'' with a narrow width guarantees that each sample was successfully fabricated as a single crystal.

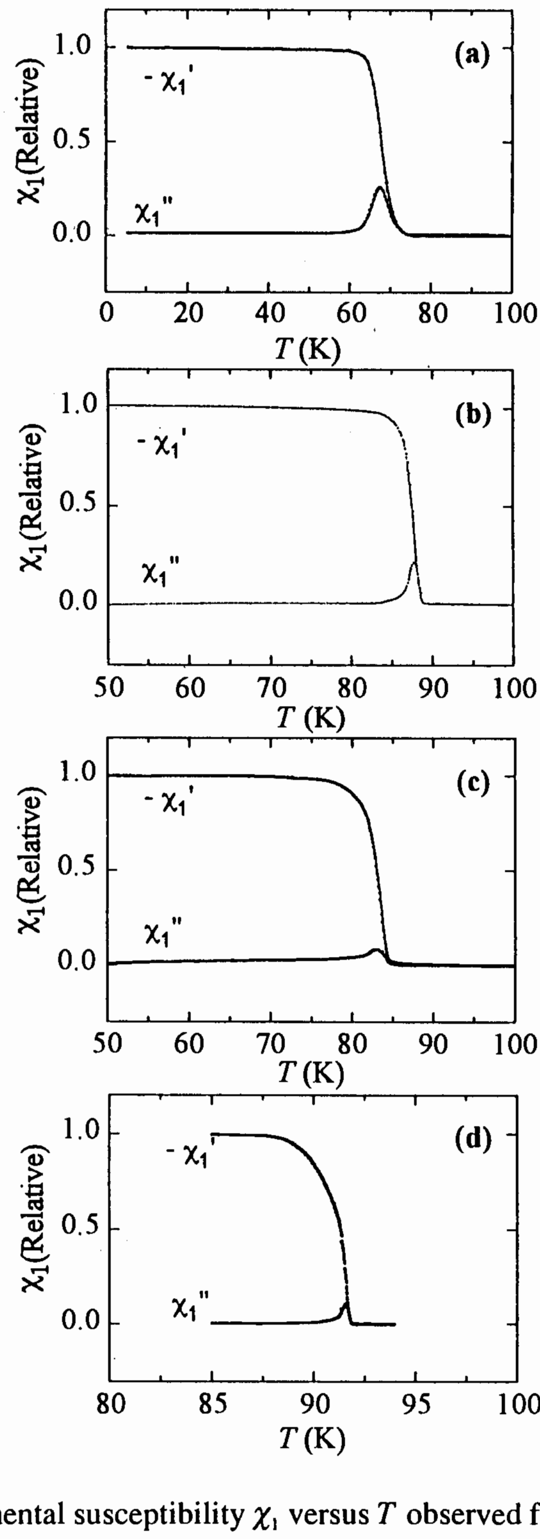

FIG. 5.1. Fundamental susceptibility χ_1 versus T observed for (a) thin-film Bi2212, (b) thin-film Y123, (c) bulk Bi2212, and (d) bulk Y123, where $\mu_0 H_{ac} = 0.01$ mT and $f = 132$ Hz.

III. RESULTS

A. Simulation of Observed χ_n

As have been described in Sec. II of Chap. 4, when the sample magnetization $M(\omega t)$ is expressed by Eq. (5.1), the real and imaginary components of χ_n can be obtained as

$$\chi_n' = \frac{1}{\pi H_{\mathrm{ac}}} \int_0^{2\pi} M(\omega t) \cos(n\omega t) d(\omega t), \tag{5.2}$$

$$\chi_n'' = \frac{1}{\pi H_{\mathrm{ac}}} \int_0^{2\pi} M(\omega t) \sin(n\omega t) d(\omega t). \tag{5.3}$$

Therefore, using the appropriate magnetization equations $M(\omega t)$ derived in the framework of the modified KA model, we can evaluate χ_n' and χ_n''. To carry out the calculation, one period of the alternating magnetic field $H(\omega t)$ was divided into 360 regular intervals, and $M(\omega t)$ was numerically obtained at each point. Using the calculated results of $M(\omega t)$ in Eqs. (5.2) and (5.3), we evaluated χ_n' and χ_n''.

The temperature dependence of χ_n comes from the parameters which involve T. In the modified KA model, the temperature dependence of χ_n is introduced through the material parameters k and B_0, surface barriers ΔH, and lower critical fields H_{c1}.

In Sec. III of Chap. 4, we obtained the temperature dependence of k and B_0 for melt-processed Y123 as

$$k(T/T_c) = k(0)(1-T/T_c)^3, \tag{5.4}$$

$$B_0(T/T_c) = B_0(0)(1-T/T_c)^{3/2}, \tag{5.5}$$

where we used the KA model. However, as the first approximation, we adopt the relation given by Eqs. (5.4) and (5.5) in further numerical calculations of χ_n for Bi2212 and Y123 single crystals. This assumption seems not to be intolerable by the following three reasons.

(1) Observed χ_n profiles are qualitatively very similar even for different materials, Bi2212 and Y123.

(2) The parameters k and B_0 are physically independent of ΔH and H_{c1}.

(3) Simulations using Eqs. (5.4) and (5.5) seem to be successful for both Bi2212 and Y123.

Although the dependence of ΔH still remains to be resolved, we empirically assumed

$$\Delta H(T/T_c) = \Delta H(0)(1-T/T_c)^{3/2}. \tag{5.6}$$

This assumption is based on the fact that iterative simulations of experimental χ_n converge to the exponent $3/2$ in Eq. (5.6). It is suggestive that the temperature dependence of ΔH found here is similar to that of the critical-current density J_c for a tunnel junction, $J_c \propto (1-T/T_c)^{3/2}$. As to H_{c1}, we discuss below.

B. Thin-Film Single Crystals

In Fig. 5.2, we show observed χ_n ($n = 2, 3, 5, 7$) versus reduced temperature T/T_c for thin-film Bi2212, where the applied field is perpendicular to the film surface (parallel to the c axis). In Fig. 5.3, we also show χ_n ($n = 2, 3, 5, 7$) versus T/T_c for thin-film Y123 observed in a similar experimental condition, where χ_3, χ_5, and χ_7 are taken from Ref. 111. Data are normalized to the saturated value of $|\chi_1'|$ of each sample. The reproducibility of the data were excellent.

Specific features seen in the figures are as followings:

(1) In the $\chi_5(T)$ and $\chi_7(T)$ curves, we see small oscillations in the lower temperature regions (Bi2212: $T/T_c <\sim 0.85$, Y123: $T/T_c <\sim 0.97$).

(2) χ_2 signals of Bi2212 are much larger than those of Y123.

For simulations of observed χ_n with Eqs. (5.2) and (5.3), we apply the magnetization equations developed in Chap. 2. However, in the theoretical treatments there, we considered an infinite cylindrical specimen, and therefore for applications of the theory to a thin-film or fractional bulk specimen, corrections for the demagnetization effect are needed.

When a magnetic field H is applied along the rotation axis of a spheroid, the internal magnetic field H_i is uniform and is written as [81]

$$H_i = [H - \frac{N_c B(H)}{\mu_0}]/(1-N_c), \tag{5.7}$$

where $B(H)$ denotes the magnetic flux density in the spheroid and N_c is the demagnetization coefficient.

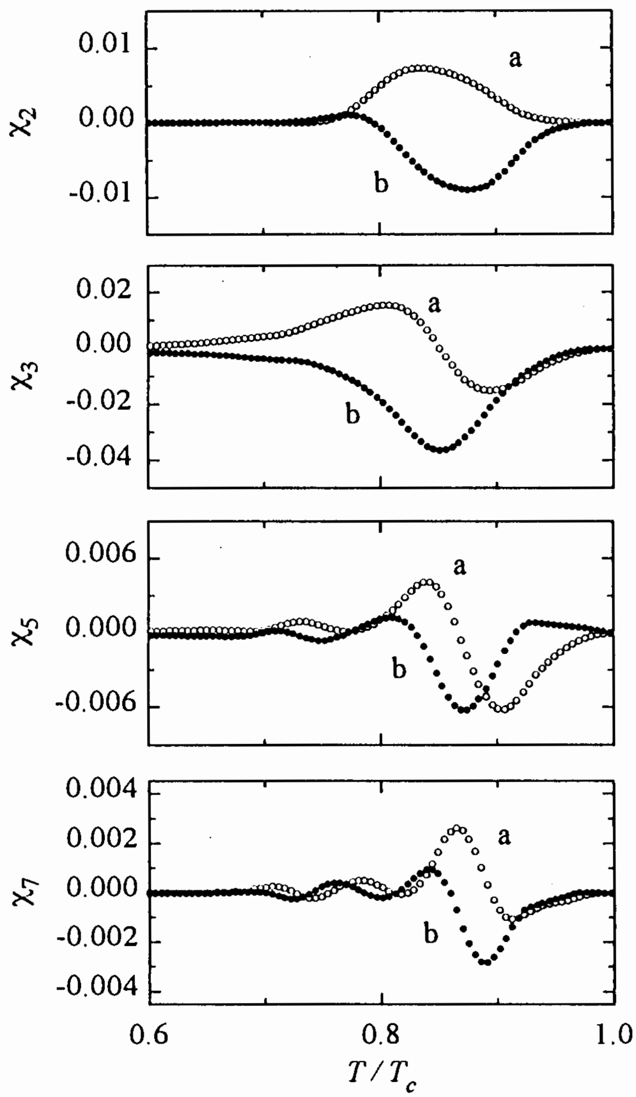

FIG. 5.2. Observed χ_n ($n = 2, 3, 5, 7$) versus T/T_c for thin-film Bi2212, where $\mu_0 H_{ac} = 0.1$ mT and $f = 132$ Hz. (a) is the real component and (b) is the imaginary component. Data are normalized to the saturated value of $|\chi_1'|$.

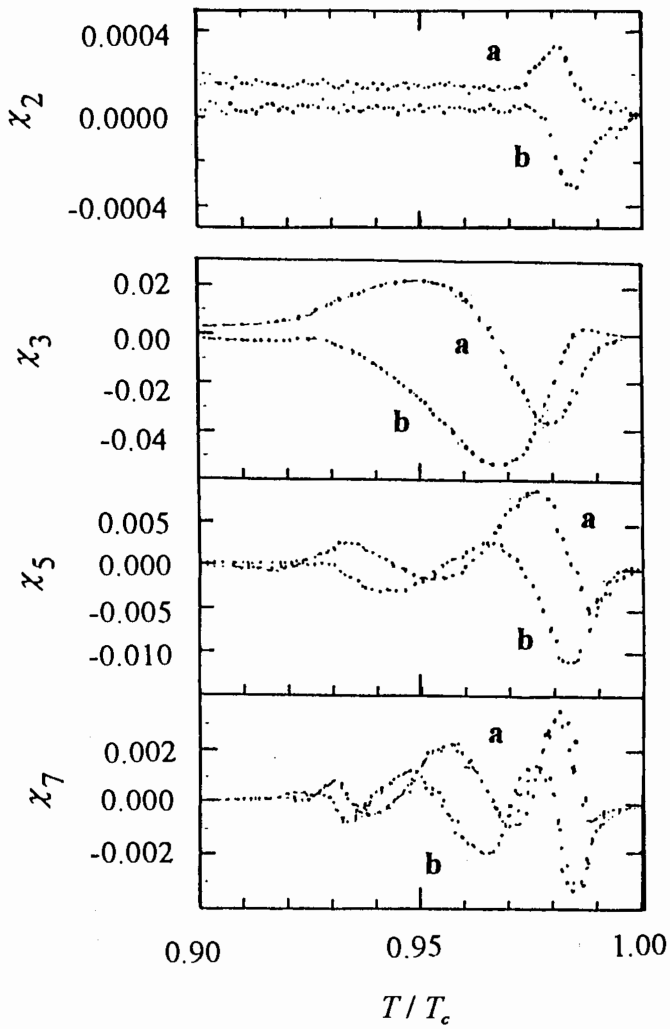

FIG. 5.3. Observed χ_n ($n = 2, 3, 5, 7$) versus T/T_c for thin-film Y123, where χ_3, χ_5, and χ_7 are taken from Ref. 111. $\mu_0 H_{ac} = 0.1$ mT and $f = 132$ Hz. (a) is the real component and (b) is the imaginary component. Data are normalized to the saturated value of $|\chi_1'|$.

A film can be regarded as a flat spheroid with a thin pancake shape whose length of the short axis reaches a limit value to zero, and in this case, N_c is approximately given by $N_c = 1 - \frac{1}{2}\pi(d/R)$ [81], where $2d$ is the film thickness and R is the radius. Therefore, the demagnetization coefficient N_c is nearly unit, i.e., the internal field of the sample is extremely enhanced. When the sample is perfectly diamagnetic $[B(H) = 0]$, $H_i = (2R/\pi d)H$. This relation implies that the effective lower critical field for a thin film can be neglected.

Above discussion suggests that in the magnetization curve measured for thin-film specimens, one cannot find a step-like feature predicted by the theory in Chap. 2. In fact, as shown in Fig. 5.4, we do not find any step-like feature in the magnetization loop for thin-film Y123 measured at 4.2 K.

To reveal the origin of small oscillations found in the χ_5 and χ_7 versus T/T_c curves for Bi2212 below $T/T_c \sim 0.85$, we demonstrate two types of calculations; $\Delta H = 0$ and $\Delta H \neq 0$. First, in Fig. 5.5, we show χ_n ($n = 2, 3, 5, 7$) versus T/T_c with $\Delta H = 0$. As seen in the figure, we can reproduce well the profile in the temperature region near T_c, but small oscillations which appear in the lower temperature region can never be reproduced. On the contrary, when a nonzero value of ΔH is introduced in the calculation, the small oscillation appeared in the profiles of χ_5 and χ_7 can be reproduced. We show the best result in Fig. 5.6, where $k(0) = 250$ N/m^3, $B_0(0) = 1$ mT, $\mu_0 \Delta H(0) = 0.5$ mT, $H_{c1} = 0$, $\mu_0 H_{ac} = 0.1$ mT, and $\mu_0 H_{dc} = 0.03$ mT. This fact strongly suggests that the surface barrier plays an essential role for the magnetic response of thin-film superconductors. From the best fitting shown in Fig. 5.6, we find the surface barrier for thin-film Bi2212 is 0.5 mT, which lies in the same order to the result by Zeldov *et al.* [48], ~ 0.5 mT at 75 K.

Similar fittings were carried out for observed χ_n versus T/T_c of thin-film Y123. In Fig. 5.7, are shown the best fittings of χ_n versus T/T_c for the Y123 film, where $k(0) = 2.0 \times 10^6$ N/m^3, $B_0(0) = 1500$ mT, $\mu_0 \Delta H(0) = 3.0$ mT, $H_{c1} = 0$, $\mu_0 H_{ac} = 0.1$ mT, and $\mu_0 H_{dc} = 0.03$ mT. As given here, the surface barrier of thin-film Y123 is 3.0 mT, which is comparable to the result by Yamamoto *et al.* [111] deduced from the modified Bean model, 1.0 mT.

As discussed in Chap. 4, the even-n harmonics appear only when the magnetization curve has an asymmetric feature. The nonzero values of χ_2 shown in Figs. 5.2 and 5.3 should therefore be originated from the asymmetric $M(H)$ loops. In Fig. 5.8, we show the $M(H)$ curves used

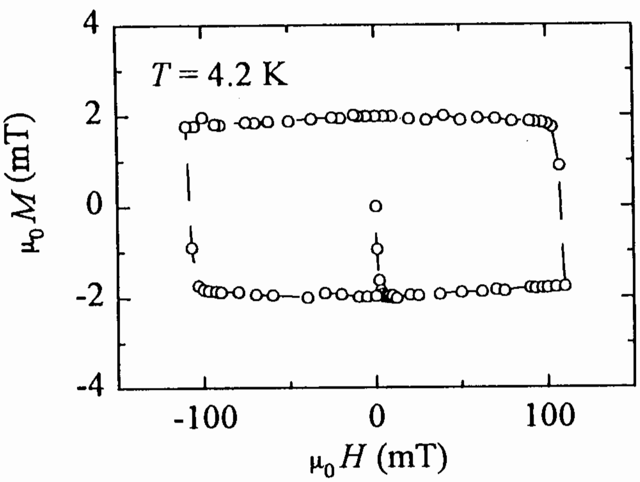

FIG. 5.4. Observed initial and full-hysteresis curves for thin-film Y123 at 4.2 K.

for theoretical simulations of χ_2 given in Figs. 5.6 and 5.7. As demonstrated in Fig. 5.8(a), the $M(H)$ loop for Bi2212 has a strong asymmetric feature which is caused by the existence of H_{dc} as well as by the B_i-dependent J_c [$= k/(B_0 + |B_i|)$], where B_i is the local flux density inside the specimen. And this certainly gives rise to relatively large signals of χ_2.

On the contrary, the asymmetry of the $M(H)$ loop for Y123 [Fig. 5.8(b)] is quite weak, and the loop draws almost like a Bean-type curve. It should be noted that when J_c is a constant, the $M(H)$ loop tends to hold a symmetric nature even when $H_{dc} \neq 0$ (see Sec. IV of Chap. 2). Since the dependence of J_c on B_i for thin-film Y123 is quite small, χ_2 signals are to be small compared to those of Bi2212.

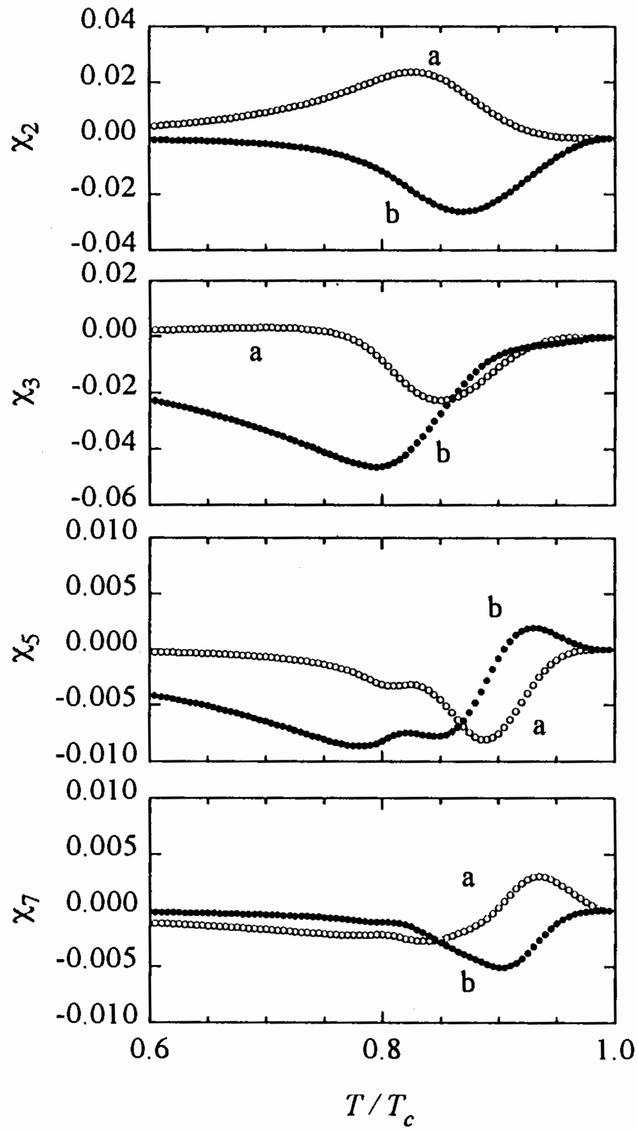

FIG. 5.5. Calculated χ_n ($n = 2, 3, 5, 7$) versus T/T_c for thin-film Bi2212 by the modified KA model, where $k(0) = 250$ N/m^3, $B_0(0) = 1$ mT, $\Delta H = 0$, $H_{c1} = 0$, $\mu_0 H_{ac} = 0.1$ mT, and $\mu_0 H_{dc} = 0.03$ mT. (a) is the real component and (b) is the imaginary component.

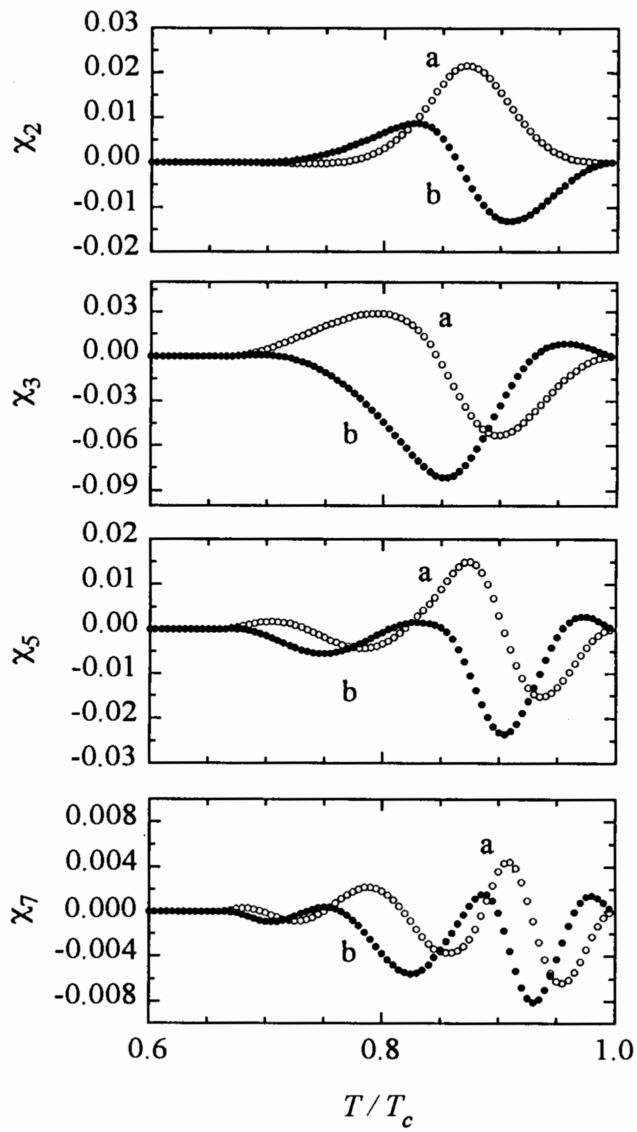

FIG. 5.6. Calculated χ_n ($n = 2, 3, 5, 7$) versus T/T_c for thin-film Bi2212 by the modified KA model, where $k(0) = 250$ N/m^3, $B_0(0) = 1$ mT, $\mu_0 \Delta H(0) = 0.5$ mT, $H_{c1} = 0$, $\mu_0 H_{ac} = 0.1$ mT, and $\mu_0 H_{dc} = 0.03$ mT. (a) is the real component and (b) is the imaginary component.

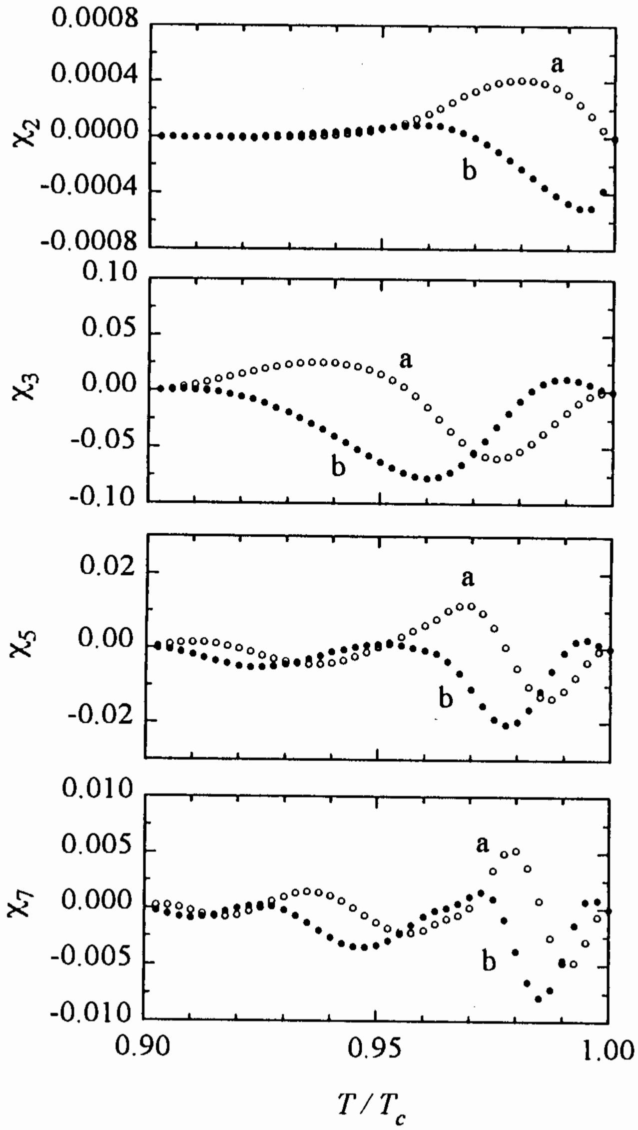

FIG. 5.7. Calculated χ_n ($n = 2, 3, 5, 7$) versus T/T_c for thin-film Y123 by the modified KA model, where $k(0) = 2 \times 10^6$ N/m^3, $B_0(0) = 1500$ mT, $\mu_0 \Delta H(0) = 3.0$ mT, $H_{c1} = 0$, $\mu_0 H_{ac} = 0.1$ mT, and $\mu_0 H_{dc} = 0.03$ mT. (a) is the real component and (b) is the imaginary component.

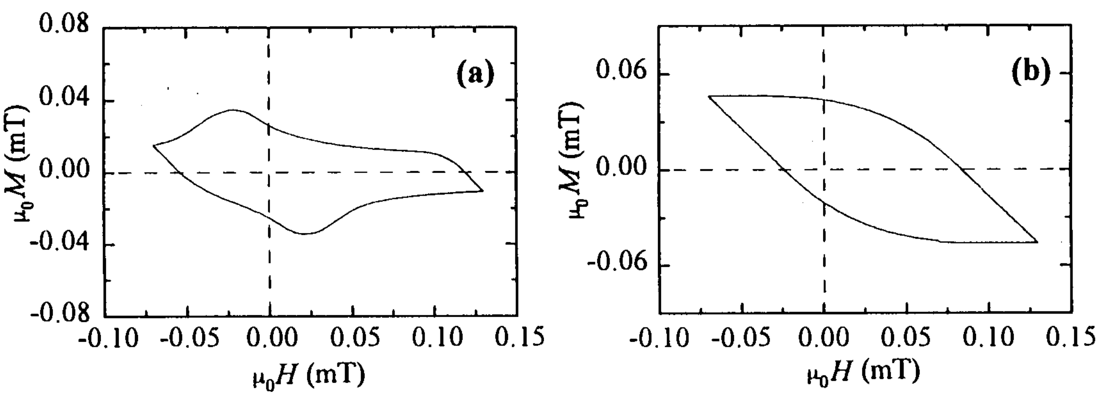

FIG. 5.8. $M(H)$ loops calculated by using the modified KA model. (a) thin-film Bi2212 at $T/T_c = 0.95$ and (b) thin-film Y123 at $T/T_c = 0.96$.

C. Bulk Single Crystals

In Fig. 5.9, we show a typical magnetization curves of the Bi2212 bulk specimen at 50 K. Evidently, we observe a step-like feature in the full-hysteresis loop, indicating that H_{c1} cannot be neglected for the bulk sample, and thus a nonzero value of H_{c1} should be introduced in analyses of observed χ_n. Recall that for thin-film samples, we did not recognize such a step-like feature (see Fig. 5.4).

As have been revealed in Chap. 3, the temperature dependences of H_{c1} of Bi2212 and Y123 bulk specimens are

$$H_{c1}(T/T_c) = H_{c1}(0)[1-(T/T_c)^{2.6}], \tag{5.8}$$

$$H_{c1}(T/T_c) = H_{c1}(0)[1-(T/T_c)^{1.0}]. \tag{5.9}$$

In Fig. 5.10, we show χ_n ($n = 2$, 3, 5) versus T/T_c experimentally obtained for Bi2212. Comparison of the $\chi_n - T/T_c$ curves with those for the thin-film Bi2212 shown in Fig. 5.2 has revealed that the profile is very different. Especially, the $\chi_2 - T/T_c$ curve of the bulk sample has a particular feature, i.e., the value of χ_2'' is much smaller than that of χ_2'.

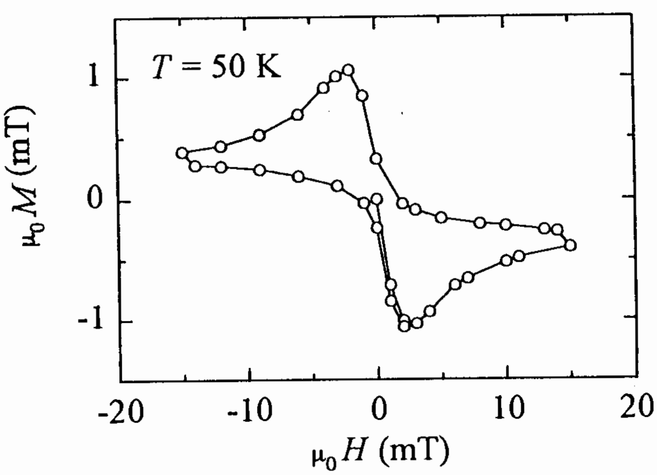

FIG. 5.9. Observed initial and full-hysteresis curves for bulk Bi2212 at 50 K.

In order to clarify the effect of H_{c1}, we first demonstrate typical $\chi_n - T/T_c$ curves calculated with $H_{c1} = 0$. As shown in Fig. 5.11, the results do not reproduce the experimental observations, where $k(0) = 5 \times 10^5$ N/m^3, $B_0(0) = 250$ mT, $\mu_0 \Delta H(0) = 0.5$ mT, $\mu_0 H_{ac} = 0.1$ mT, and $\mu_0 H_{dc} = 0.03$ mT. Note that for any value of fitting parameters used here, reproduction of the experimental results could not be achieved as far as $H_{c1} = 0$.

On the contrary, when we use a nonzero value of H_{c1}, the observed $\chi_n - T/T_c$ curves of the bulk sample can be qualitatively well reproduced. The best fittings for the present data are shown in Fig. 5.12, where $k(0) = 5 \times 10^5$ N/m^3, $B_0(0) = 250$ mT, $\mu_0 \Delta H(0) = 0.5$ mT, $\mu_0 H_{c1}(0) = 0.7$ mT, $\mu_0 H_{ac} = 0.1$ mT, and $\mu_0 H_{dc} = 0.03$ mT.

This result together with a step-like feature strongly suggests that the lower critical field H_{c1} plays an essential role in the magnetic response of the single-crystal Bi2212 bulk superconductor. The reason for a visual effect of H_{c1} in the bulk sample certainly comes from a different demagnetization coefficient N_c against thin films. The size of the present Bi2212 is 3.0 mm $\times$ 1.0 mm $\times$ 0.1 mm, and therefore N_c should be much smaller than that of thin films. Eventually, in such a case, we cannot approve of neglecting H_{c1} anymore.

In Fig. 5.13, are shown χ_n ($n = 2, 3, 5, 7$) versus T/T_c curves measured for the Y123 bulk single crystal. In the $\chi_5 - T/T_c$ and $\chi_7 - T/T_c$ curves, we find small oscillations in the lower temperature region ($T/T_c <\sim 0.99$), being similar to the case of thin films. This specific nature

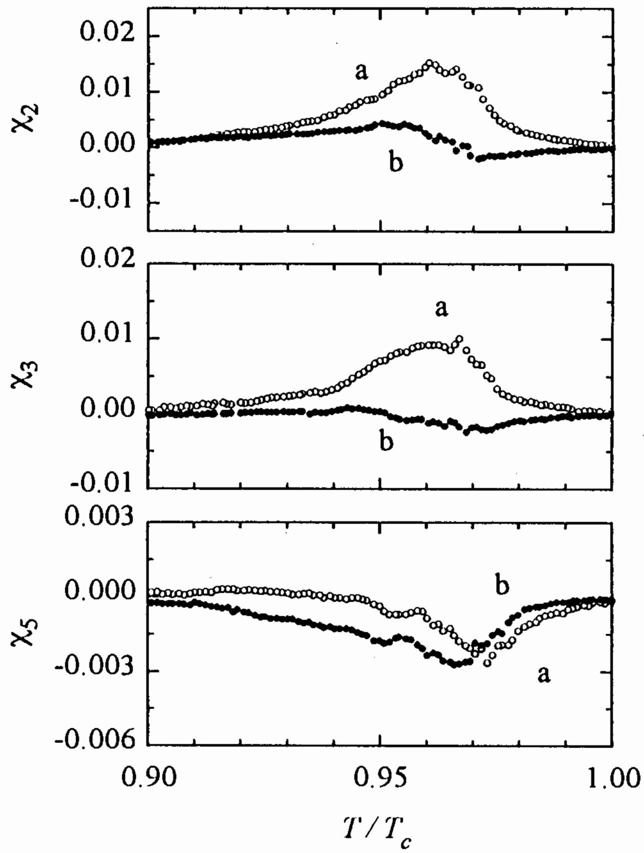

FIG. 5.10. Observed χ_n ($n = 2, 3, 5$) versus T/T_c for bulk Bi2212, where $\mu_0 H_{ac} = 0.1$ mT and $f = 132$ Hz. (a) is the real component and (b) is the imaginary component. Data are normalized to the saturated value of $|\chi_1'|$.

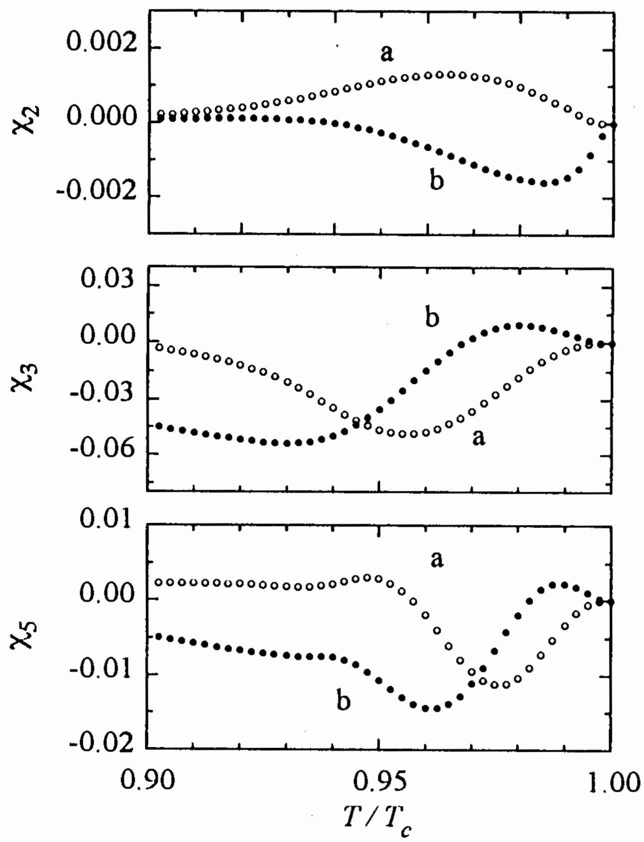

FIG. 5.11. Calculated χ_n ($n = 2, 3, 5$) versus T/T_c for bulk Bi2212 by the modified KA model ($H_{c1} = 0$), where $k(0) = 5 \times 10^5$ N/m^3, $B_0(0) = 250$ mT, $\mu_0 \Delta H(0) = 0.5$ mT, $\mu_0 H_{ac} = 0.1$ mT, and $\mu_0 H_{dc} = 0.03$ mT. (a) is the real component and (b) is the imaginary component.

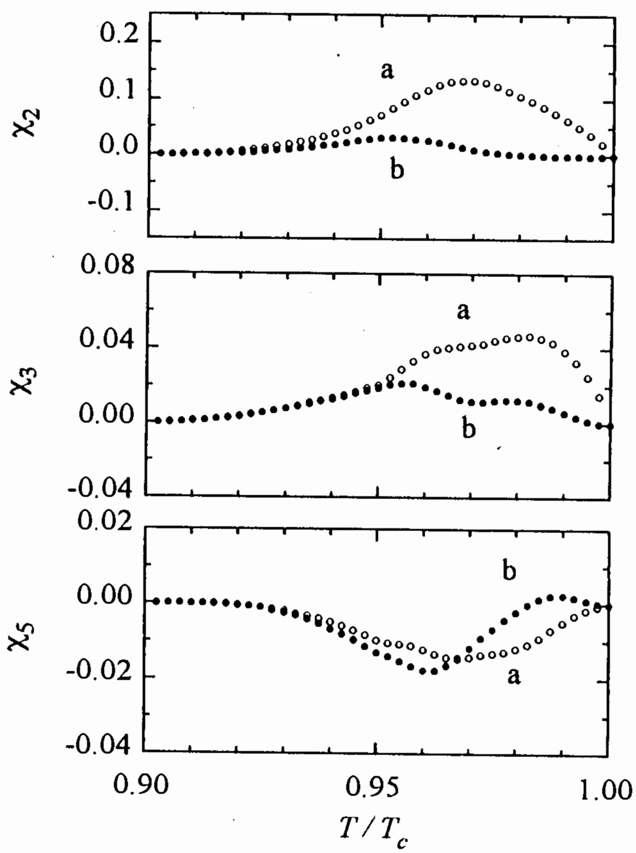

FIG. 5.12. Calculated χ_n ($n = 2, 3, 5$) versus T/T_c for bulk Bi2212 by the modified KA model, where $k(0) = 5 \times 10^5$ N/m^3, $B_0(0) = 250$ mT, $\mu_0 \Delta H(0) = 0.5$ mT, $\mu_0 H_{c1}(0) = 0.7$ mT, $\mu_0 H_{ac} = 0.1$ mT, and $\mu_0 H_{dc} = 0.03$ mT. (a) is the real component and (b) is the imaginary component.

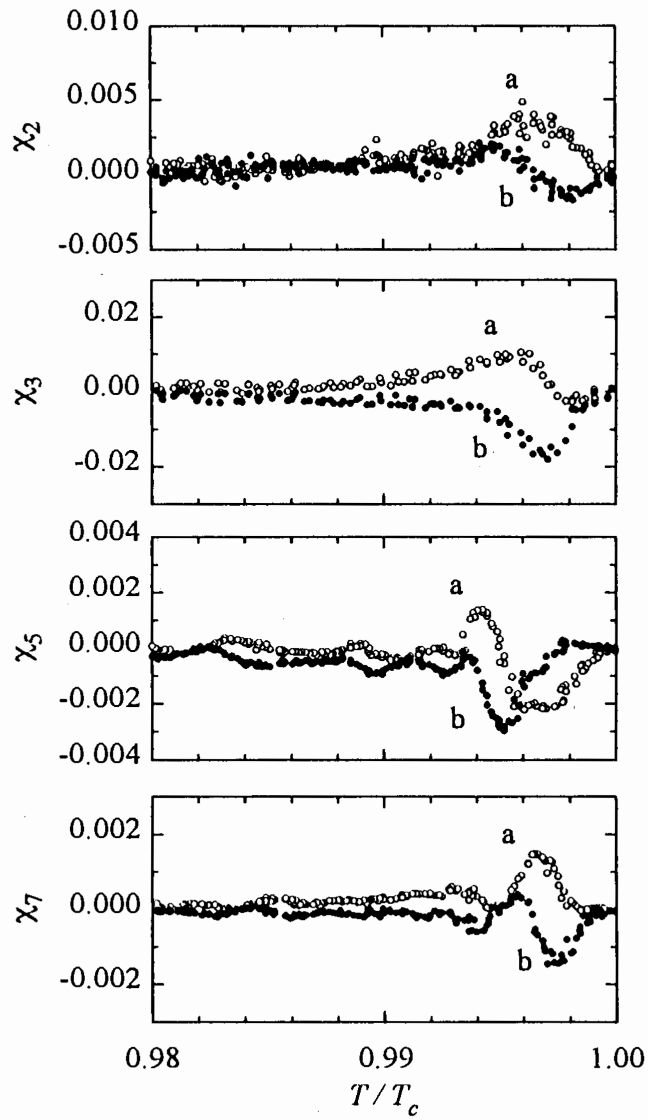

FIG. 5.13. Observed χ_n (n = 2, 3, 5, 7) versus T/T_c for bulk Y123, where $\mu_0 H_{ac} = 0.18$ mT and $f = 132$ Hz. (a) is the real component and (b) is the imaginary component. Data are normalized to the saturated value of $|\chi_1'|$.

suggests that in the case of the Y123 bulk sample, surface barriers play an important role. In order to clarify this effect, in Fig. 5.14, we first show the χ_n ($n = 2, 3, 5, 7$) versus T/T_c curves calculated with $\Delta H = 0$, where $k(0) = 5 \times 10^7$ N/m^3, $B_0(0) = 200$ mT, $\mu_0 H_{c1}(0) = 3$ mT, $\mu_0 H_{ac} = 0.18$ mT, and $\mu_0 H_{dc} = 0.03$ mT. As far as $\Delta H = 0$, we could not reproduce the observed results for any value of other parameters. Especially, the small oscillation of χ_5 and χ_7 in the lower temperature region can never be reproduced when ΔH is assigned to zero. However, when we adopt a nonzero value of ΔH, the specific nature of the experimental χ_n curves can be qualitatively reproduced. In Fig. 5.15, we show the best fittings of χ_n ($n = 2, 3, 5, 7$) versus T/T_c, where the fitting parameters are the same with those used in Fig. 5.14, except $\mu_0 \Delta H(0) = 80$ mT.

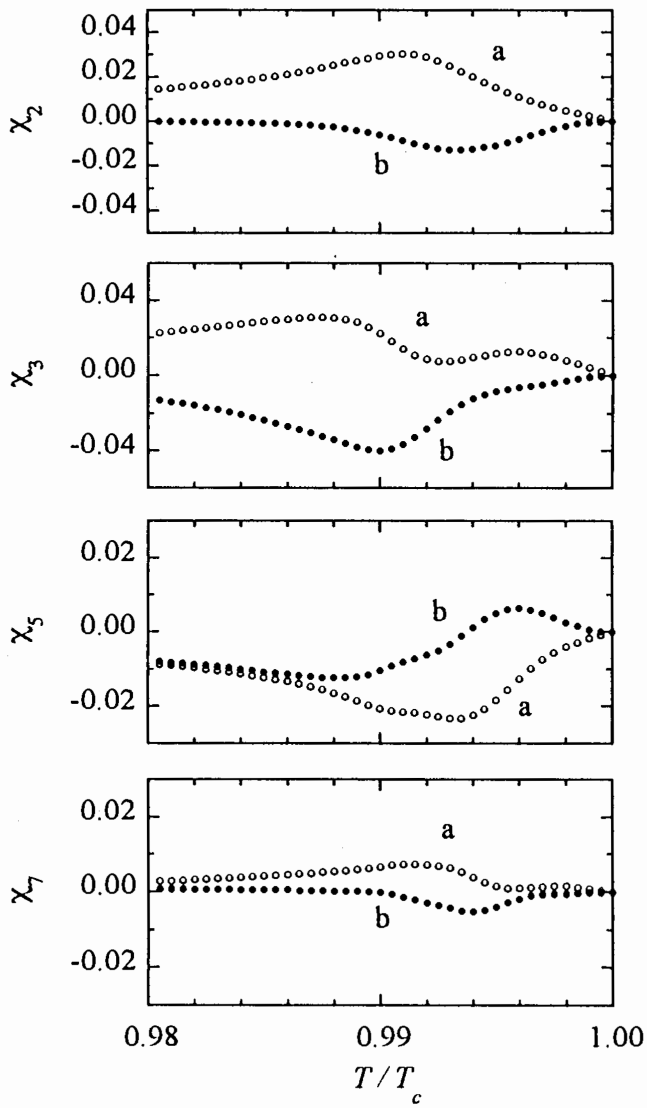

FIG. 5.14. χ_n ($n = 2, 3, 5, 7$) versus T/T_c for bulk Y123 by the modified KA model ($\Delta H = 0$), where $k(0) = 5 \times 10^7$ N/m^3, $B_0(0) = 200$ mT, $\mu_0 H_{c1}(0) = 3$ mT, $\mu_0 H_{ac} = 0.18$ mT, and $\mu_0 H_{dc} = 0.03$ mT. (a) is the real component and (b) is the imaginary component.

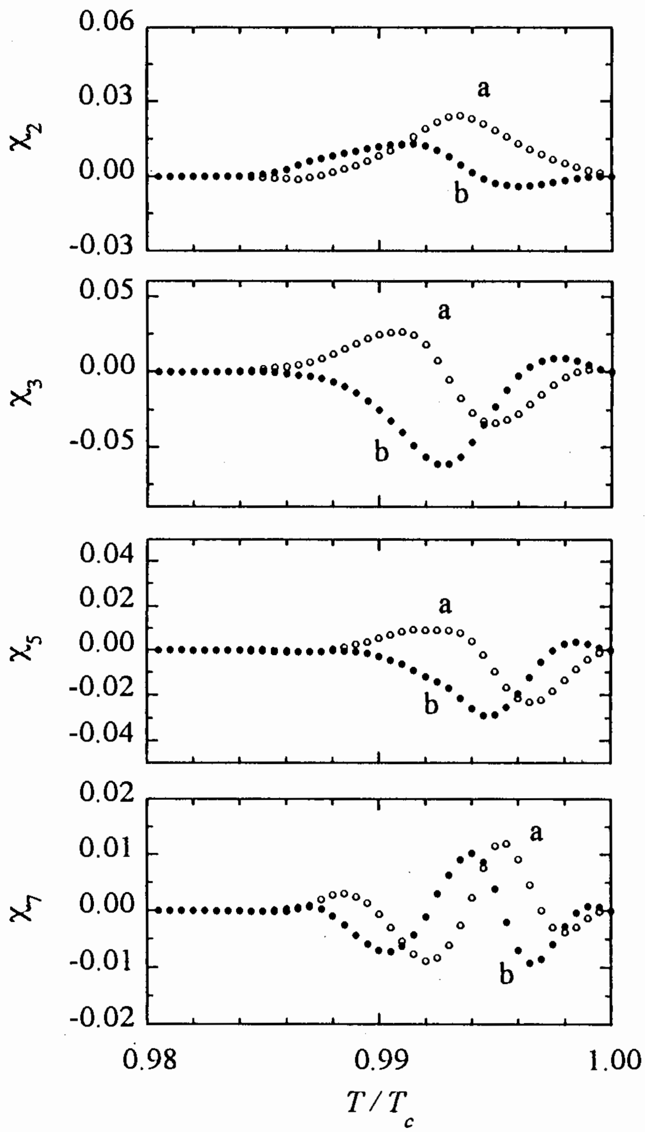

FIG. 5.15. Calculated χ_n ($n = 2, 3, 5, 7$) versus T/T_c for bulk Y123 by the modified KA model, where $k(0) = 5 \times 10^7$ N/m^3, $B_0(0) = 200$ mT, $\mu_0 \Delta H(0) = 80$ mT, $\mu_0 H_{c1}(0) = 3$ mT, $\mu_0 H_{ac} = 0.18$ mT, and $\mu_0 H_{dc} = 0.03$ mT. (a) is the real component and (b) is the imaginary component.

IV. DISCUSSION

Table 5.1 lists surface barriers and lower critical fields for cuprate-based oxide superconductors (thin-film and bulk single crystals). Noticeable features revealed in the table are:

(1) Surface barriers $\mu_0 \Delta H$ for thin films are a few mT or less.

(2) There is a remarkable difference between $\mu_0 \Delta H$'s of bulk Bi2212 and bulk Y123, and moreover $\mu_0 \Delta H$ for bulk Bi2212 has a similar value found for thin films.

(3) Present result of $\mu_0 \Delta H$ for thin-film Bi2212 lies in the same order to that given in Ref. 48, in spite of the different measurement.

(4) Lower critical fields $\mu_0 H_{c1}$ for thin films are effectively zero due to the demagnetization effect.

First, we discuss more or less quantitatively about geometrical barriers. We consider a thin superconducting strip with a rectangular cross section of width $2W$ ($-W < x < W$) and thickness d ($-d/2 < z < d/2$ and $d \ll W$) which infinitely expands in the y direction. When the applied field H is perpendicular to the strip (along the positive z direction), the resulting Meissner current is given as [161, 162]

$$J_y(x) \quad = \quad -\frac{H}{2\pi d}\frac{x}{(W^2-x^2)^{1/2}}, \qquad |x| < W. \tag{5.10}$$

Applying Eq. (5.10), Zeldov *et al.* [48] obtained a position-dependent vortex energy per unit length $\varepsilon(x)$ not too close to the edges;

$$\varepsilon(x) \quad = \quad \varepsilon_0 + \phi_0 \int_x^W J_y(t)dt, \tag{5.11}$$

TABLE 5.1. Surface barriers ΔH and lower critical fields H_{c1} for single-crystal (thin film and bulk) superconductors.

Samples	$\mu_0 \Delta H(0)$	$\mu_0 \Delta H(T/T_c)$	$\mu_0 H_{c1}(0)$	T_c	Ref.
Thin-film Bi2212	0.5 mT	$\sim$ 0.1mT ($T/T_c = 0.83$)	0.0 mT	76.0 K	present
Thin-film Y123	3.0 mT	–	0.0 mT	88.9 K	present
Bulk Bi2212	0.5 mT	–	0.7 mT	85.0 K	present
Bulk Y123	80.0 mT	$\sim$ 36mT ($T/T_c = 0.44$)	3.0 mT	92.0 K	present
Thin-film Y123	1.0 mT	–	0.0 mT	88.9 K	[111]
Thin-film Bi2212	–	$\sim$ 0.5mTat75K ($T/T_c =\sim 0.83$)	–	$\sim$ 90 K	[48]
Bulk Y123	–	$\sim$ 10mTat35K ($T/T_c =\sim 0.44$)	–	$\sim$ 80 K	[46]

where ε_0 is the line energy of a non-interacting vortex and ϕ_0 is the flux quantum. In increasing H the vortices initially cut through the sharp rims of the sample without complete penetration, and thus effectively round off the curvature of the edges on the order of $d/2$ (see Fig. 1 of Ref. 48). From Eqs. (5.10) and (5.11), we realize that $\varepsilon(x)$ increases with decreasing d, resulting in the increase of the geometrical barrier.

Above discussion indicates that for superconducting thin films subjected to a perpendicular magnetic field, the geometrical barrier is expected to be predominant due to very small values of d. Therefore, the values of $\mu_0\Delta H$ listed in Table 5.1 for thin films is reasonably considered to be attributed to the geometrical barrier.

It is evident that for bulk specimens with much larger d, the geometrical barrier should be much smaller than those for thin films. However, from the best fittings of experimental χ_n, we found $\mu_0\Delta H(0) = 80$ mT for the present bulk Y123. Comparison of the values of $\mu_0\Delta H$ for the thin-film and bulk Y123 suggests that the present result, 80 mT, should be practically attributed to another origin, i.e., to the BL barrier which is a surface energy barrier caused by an image force for a semi-infinite superconducting specimen.

Using $YBa_2Cu_4O_8$ (Y124) single crystals, Xu *et al.* [46] have reported strong surface barrier effects which show a classic BL shape with magnetization close to zero for the leg of the hysteresis loop. According to their observations, $\mu_0\Delta H$ at 35 K ($T/T_c = 0.44$) is roughly 10 mT. Although the experimental procedures are essentially different, their result is comparable to our result for bulk Y123; $\mu_0\Delta H(0.44) = 36$ mT.

A noticeable fact found here is that $\mu_0\Delta H$ for Bi2212 is much smaller than that for bulk Y123, 80mT, and is comparable to that of thin films, 0.5 mT. The main reason for this experimental evidence probably comes from the distinctive structural character of Bi2212. As is well known, the crystal structure of Bi2212 consists of leaf-like laminating layers and is breakable along the direction of the CuO_2 plane. Due to this specific structural feature, the origin of ΔH for bulk Bi2212 would be the geometrical barriers, and thus $\mu_0\Delta H$ gives a similar value to that of thin films.

In order to obtain the intrinsic value of ΔH for a fractional specimen, we have to take into consideration the demagnetization effect. For a thin film which can be approximated as a flat spheroid with a thin pancake shape whose length of the short axis reaches a limit value to zero, the demagnetization coefficient N_c is nearly unit. On the contrary, N_c for a bulk specimen becomes smaller than unit. From the sample geometry, we estimated N_c of the present bulk Y123 as 0.82. The intrinsic lower critical field can be obtained from the relation, $H'_{c1} = H_{c1}/(1 - N_c)$, and thus $\mu_0 H'_{c1}(0)$ is 16.5 mT. Corrections for ΔH are also needed. Since, in the initial magnetization, ΔH draws the Meissner slope in the same way as H_{c1}, we believe that the intrinsic value of surface barriers can be obtained using a similar relation, $\Delta H' = \Delta H/(1 - N_c)$, and thus $\mu_0 \Delta H'(0) = 440$ mT.

Meanwhile, in the London theory, the field for first vortex entry H_s is given as the sum of the BL barrier and the lower critical field ;

$$\begin{aligned} \mu_0 H_s(0) &= \mu_0 \Delta H_{\mathrm{BL}}(0) + \mu_0 H'_{c1}(0) \\ &= \frac{\phi_0}{4\pi\lambda_{ab}(0)\xi_{ab}(0)}, \end{aligned} \tag{5.12}$$

where

$$\mu_0 H'_{c1}(0) = \frac{\phi_0}{4\pi\lambda_{ab}^2(0)}\left[\ln\frac{\lambda_{ab}(0)}{\xi_{ab}(0)} + 0.5\right]. \tag{5.13}$$

In Eqs. (5.12) and (5.13), λ_{ab} and ξ_{ab} are the penetration depth and the coherence length, respectively, in the direction of the current. Substituting $\lambda_{ab}(0) = 142$ nm [83] and $\xi_{ab}(0) = 1.6$ nm [84], $\mu_0 \Delta H_{\mathrm{BL}}(0)$ and $\mu_0 H'_{c1}$ are roughly obtained as 680 and 40.7 mT, respectively.

The calculated value of $\Delta H_{\mathrm{BL}}(0)$ is larger than $\mu_0 \Delta H'(0) = 440$ mT found in the present work, but lies in the same order. This indirectly supports that $\mu_0 \Delta H'(0)$ for the Y123 determined here would be attributed to the BL barrier. Note that calculated $\mu_0 H'_{c1}(0)$ is also comparable to the experimentally determined result, $\mu_0 H'_{c1}(0) = 16.5$ mT.

V. CONCLUSIONS

Determinations of surface barriers ΔH of cuprate-based oxide superconductors have been attempted from measurements of higher-harmonic susceptibilities χ_n. The samples used were Bi2212 and Y123 single crystals (thin-film and bulk specimens).

Experimentally obtained χ_n in an ac magnetic field superimposed on a dc field were analyzed using magnetization equations derived in the framework of the modified KA model, where k, B_0, ΔH, and H_{c1} were used as fitting parameters.

From the results for thin-film Bi2212 and Y123 in the magnetic field perpendicular to the film surface (parallel to the c axis), we found the following features;

(1) χ_5 and χ_7 versus T/T_c curves showed small oscillations in the lower temperature region.

(2) χ_2 signals of Bi2212 are much larger than those of Y123.

Analyses of the observed χ_n have revealed that the small oscillation can be reproduced by adopting nonzero values of ΔH, indicating that ΔH is responsible for the oscillation. Distinctive difference between χ_2 signals of Bi2212 and Y123 were attributed to their different asymmetry of the magnetization loops. In addition, it has been confirmed that H_{c1} can be practically neglected due to the demagnetization effect.

The values of $\mu_0\Delta H(0)$ for the films were found to be a few mT or less. The results found here can be attributed to the geometrical barrier, because it should be predominant for thin films in an applied field perpendicular to the film surface.

The specific features found from observed χ_n for bulk Bi2212 and Y123 specimens are:

(1) Similar to χ_n for thin-film specimens, the χ_5 and χ_7 versus T/T_c curves for Y123 also show small oscillations in the lower temperature region.

(2) However, the oscillations do not seem to appear for Bi2212.

From analyses of the observed χ_n, we found a remarkable difference between ΔH's of bulk Bi2212 and bulk Y123. $\mu_0\Delta H(0)$ for Bi2212 has a similar value found for the thin films, 0.5 mT, while $\mu_0\Delta H(0)$ for Y123 is as large as 80 mT. It is evident that for bulk specimens much thicker than thin films, the geometrical barrier should be much smaller than those for thin films, and therefore $\mu_0\Delta H(0) = 80$ mT for bulk Y123 is reasonably attributed to the BL barrier. The small value $\mu_0\Delta H(0) = 0.5$ mT for Bi2212 probably attributed to the specific structural characteristic which consists of leaf-like laminating layers.

Inferring from the results obtain here, we believe the experimental technique promoted here in terms of χ_n would provide a useful tool for investigations of ΔH.

Chapter 6

Correlation between Carrier Density and Critical Temperature of $Bi_2Sr_2CaCu_2O_{8+\delta}$ and $YBa_2Cu_3O_{7-\delta}$ Single Crystals

I. INTRODUCTION

There have been many researches [14, 15, 163–167] on the topic of a remarkable correlation between the superconducting transition temperature T_c of cuprate-based oxide superconductors and the carrier (hole) density of the two-dimensional CuO_2 plane involved in these systems. The reason for such active investigations is that this correlation provides a basic approach to the fundamental mechanism of superconductivity in the cuprate superconductors and would lead to the key which brings to light the high critical temperature far above the value predicted by the BCS theory.

There are several conventional methods to prepare the oxide superconductors with different carrier densities; for example, substitution of elements with different valence electrons, compression of the sample under high pressures, or control of oxygen concentration by annealing. In the followings, we first review briefly some of the serial studies on the correlation between T_c and the carrier density.

By substituting various elements with different valence elements, Kakihana *et al.* [15] have performed a series of investigations in terms of Raman spectra. Using different Co content x in $YBa_2Cu_{3-x}Co_xO_{7-\delta}$ ($0 \leq x \leq 0.6$), they made systematic observations of the Raman spectra and revealed that the oxygen vibration modes as well as T_c are sensitive to local changes of the valency and the charge balance between the CuO chains and the CuO_2 planes.

The influence of partial isomorphous substitution of Sr for the Ba sites and trivalent ions for the Cu sites in $YBa_2Cu_3O_{7-\delta}$ (Y123), Kakihana *et al.* [166] observed Raman scattering and neutron diffraction. From the results, they suggested that the variation of T_c and the structural changes are caused by a hole charge transfer from the CuO_2 planes to the CuO chains. Berastegui *et al.* [167] have studied the crystal structure of $Y_{1-x}Ca_xBa_2Cu_4O_8$ at room temperature by Rietveld analysis of time-of-flight neutron powder diffraction. From calculations of Madelung energies based upon the structural data, they concluded that the number of holes in the conducting CuO_2 plane increases with increasing Ca content, which is qualitatively consistent with the observed increase in T_c. More recently, Kakihana *et al.* [14] investigated the phonon Raman spectra of $Bi_2Sr_2Ca_{1-x}Y_xCu_2O_{8+\delta}$ ($x = 0-1$) in a number of well-defined single-crystal and polycrystalline samples, and observed a rapid suppression of T_c at $x \approx 0.5$. The

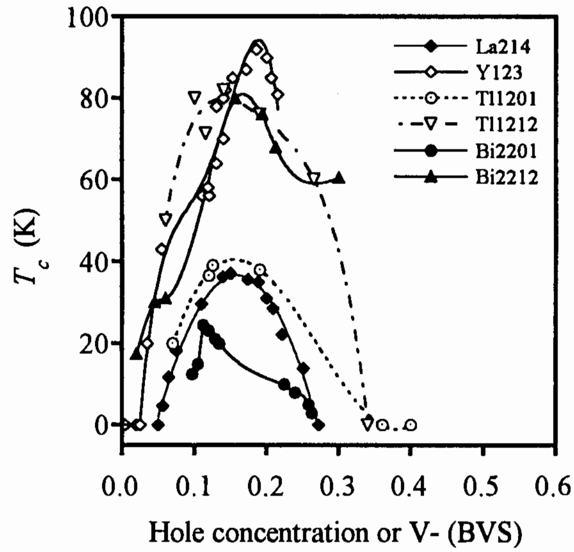

FIG. 6.1. Schematic illustration of how change carrier concentration in CuO_2 plane and T_c in various high-T_c cuprates [165].

phonon-frequency changes observed there were explained by the "*internal pressure*" induced by the decrease in the average Ca/Y ion size and additional "*charge-transfer*" induced by the change in the Cu and Bi valences with Y doping.

Through these studies together with those by other groups [163, 164], it has been revealed that T_c first increases with the increase of carrier doping, and then at a certain optimum carrier density, T_c shows saturation. In overdoped regions, however, suppression of T_c occurs (see Fig. 6.1).

There have been another serial investigations on the carrier-density dependence of T_c in terms of muon-spin relaxation (μSR). Uemura *et al.* [168] carrier out μSR measurements on $YBa_2Cu_3O_{7-\delta}$ with averaged oxygen concentrations $\delta = 0$, 0.05, and 0.34. They combined the results with the earlier work on $La_{1.85}Sr_{0.15}CuO_4$ [169], and discussed about the systematic variation of the observed μSR rate σ and the derived magnetic field penetration depth. Their results indicate that T_c is approximately proportional to the superconducting carrier concentration n_s divided by the effective electron mass m^*.

Using sixteen specimens of cuprate-based sintered superconductors, $La_{2-x}Sr_xCuO_4$ (La214) ($x = 0.08 - 0.21$), $YBa_2Cu_3O_{7-\delta}$ ($\delta = 0.13 - 0.33$), $Bi_2Sr_2CaCu_2O_{8+\delta}$ (Bi2212), $Bi_{2-x}Pb_xSr_2$-$Ca_2Cu_3O_{10}$ (Bi2223), and $Tl_2Ba_2Ca_2Cu_3O_{10}$ (Tl2223), Uemura *et al.* [170] measured the μSR rate σ and found a universal linear relation between T_c and $\sigma(0) \propto n_s/m^*$. In overdoped samples, however, T_c shows saturation and suppression with increasing n_s/m^*, as have been reported on the correlation between T_c and the normal-state carrier density. From these evidences, they argue that the feature distinguishes these cuprate-based oxide superconductors from ordinary BCS superconductors.

As reviewed above, the μSR technique is very effective for studies of this topic. However, as discussed by Kossler *et al.* [169], in μSR measurements, the transverse relaxation function $G_x(t)$ is assumed to have a Gaussian distribution $G_x(t) = \exp(-\sigma^2 t^2)$, and from experimental $G_x(t)$, they evaluate the relaxation rate σ which is proportional to the inverse square of the London penetration depth, $1/\lambda_L^2$ ($\propto n_s/m^*$).

On the contrary, in H_{c1} measurements, one can derive the correlation between T_c and n_s more straightly without fitting procedures as in the μSR measurement. In order to make the best use of this merit, we attempt to search the dependence of T_c on the carrier density through lower critical fields H_{c1}. For measurements of H_{c1}, we use Y/Pb-doped Bi2212 and Co/Ca-doped Y123 single crystals.

In this chapter, we present the experimental procedure and give some discussion with the aid of the London theory and the Ginzburg–Landau (GL) theory.

II. EXPERIMENTAL

A. Sample Preparation

Two groups of the samples were prepared. One is the Bi2212 group (samples A1, A2, A3) and the other is the Y123 group (B1, B2, B3, B4, B5). The composition and the onset temperature of the superconducting transition T_c of these samples are listed in Table 6.1. All of the samples were grown by the self-flux method [171]. In Bi2212 systems, by substituting Y^{3+} for the Ca^{2+} sites, we expect a decrease of the hole density in the CuO_2 plane, while by substituting Pb^{2+} for the Bi^{3+} sites, the density increases. Among the Bi2212 group, sample A1 has the lowest carrier concentration (underdoped) and sample A3 has the highest (overdoped).

In the Y123 group, by substituting Co^{3+} for the Cu^{2+} sites, we expect a decrease of the hole density in the CuO_2 plane, while by substituting Ca^{2+} for the Y^{3+} sites, the density increases. The variation of the hole density was carefully confirmed from the Raman spectroscopy. More details of the sample preparation and structural characterizations were previously reported [14, 79].

TABLE 6.1. Compositions, T_c, and the demagnetization coefficients N_c [80, 81] of the present samples.

Samples	Composition	T_c (K)	N_c
A1	$Bi_2Sr_2Ca_{0.6}Y_{0.4}Cu_2O_{8+\delta}$	78.0	0.84
A2	$Bi_2Sr_2CaCu_2O_{8+\delta}$	80.0	0.87
A3	$Bi_{1.8}Pb_{0.2}Sr_2CaCu_2O_{8+\delta}$	75.0	0.87
B1	$YBa_2Cu_{2.8}Co_{0.2}O_{7-\delta}$	62.0	0.59
B2	$YBa_2Cu_3O_{7-\delta}$	89.0	0.58
B3	$Y_{0.95}Ca_{0.05}Ba_2Cu_3O_{7-\delta}$	87.0	0.59
B4	$Y_{0.90}Ca_{0.10}Ba_2Cu_3O_{7-\delta}$	86.0	0.58
B5	$Y_{0.80}Ca_{0.20}Ba_2Cu_3O_{7-\delta}$	84.0	0.59

B. Determinations of the Lower Critical Field at Various Temperatures

In the London theory [3], the magnetic field penetration depth λ_{ab} is related to the superconducting condensate density n_s and the effective electron mass m^* as

$$\lambda_{ab}^2 = \frac{m^*}{n_s e^2}, \tag{6.1}$$

where the subscript ab on λ denotes the direction of the current. While, as discussed in Sec. IV of Chap. 3, the anisotropic lower critical field $H_{c1,c}$ is related to the GL parameter κ as

$$\mu_0 H_{c1,c} = \frac{\phi_0}{4\pi\lambda_{ab}^2}(\ln \kappa_c + 0.5), \tag{6.2}$$

where ϕ_0 is the flux quantum and the subscript c on κ and H_{c1} denotes the direction of the applied field.

Substituting Eq. (6.1) to Eq. (6.2), we obtain

$$\frac{n_s}{m^*} = \frac{4\pi}{e^2\phi_0(\ln \kappa_c + 0.5)}\mu_0 H_{c1,c}. \tag{6.3}$$

From Eq. (6.3), we recognize that we can evaluate n_s/m^* when $H_{c1,c}$ is determined from the magnetization curves $M(H)$, and thus the correlation between T_c and n_s/m^* can be straightly clarified.

To obtain $H_{c1,c}$ ($\propto n_s/m^*$), $M(H)$ curves of samples A1 – A3 (Bi2212 group) and samples B1 – B5 (Y123 group) at various temperatures below the critical temperature were measured using a superconducting quantum interference device (SQUID), where the applied field was parallel to the c axis of the specimen.

In Fig. 6.2, we show typical initial and hysteresis curves of Bi2212 specimens, (a) sample A1 at 30.0 K and (b) sample A3 at 50.0 K. In Fig. 6.3, we also show typical $M(H)$ curves of Y123 specimens, (a) sample B1 at 45.0 K and (b) sample B5 at 70.0 K. As described in Chaps. 2 and 3, by measuring the shift of the central line in the distorted hysteresis loop, we can determine $H_{c1,c}$. In this method of determinations of $H_{c1,c}$, the effect of the surface barrier ΔH is completely excluded (see Sec. II of Chap. 3). So far, $H_{c1,c}$ has not been applied for evaluations of n_s/m^*, in disregard of a well known relation, $H_{c1,c} \propto n_s/m^*$. The reason for this is that experimentally it is quite difficult to extract $H_{c1,c}$ from the initial magnetization curve which intrinsically includes the effect of surface barriers.

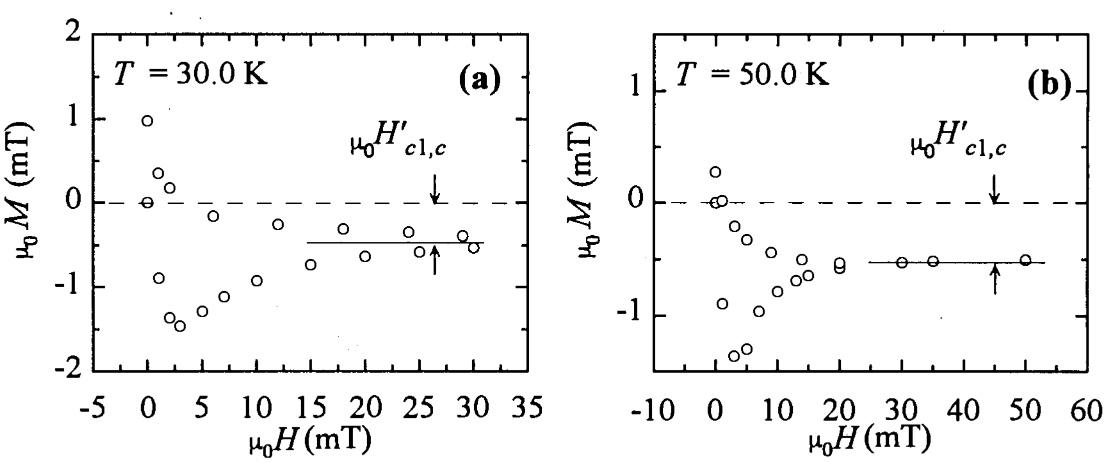

FIG. 6.2. Initial and hysteresis curves of (a) sample A1 [$Bi_2Sr_2Ca_{1-y}Y_yCu_2O_{8+\delta}$ ($y = 0.4$)] at 30.0 K and (b) sample A3 [$Bi_{2-x}Pb_xSr_2CaCu_2O_{8+\delta}$ ($x = 0.2$)] at 50.0 K, where the applied magnetic field is parallel to the c axis.

In the theoretical treatment developed in Chap. 2 for derivations of the magnetization equations within the construct of the modified Kim–Anderson model, we used an infinite long cylindrical specimen. However, it is reasonable to apply the theory to a practical fractional specimen by correcting for the demagnetization effect. The lower critical field $H'_{c1,c}$ observed in each figure should be corrected for the demagnetization effect. From the sample geometry, the demagnetization coefficients of the samples, N_c, can be estimated as listed in Table 6.1 [80, 81]. Using $H_{c1,c} = H'_{c1,c}/(1 - N_c)$, we determine $H_{c1,c}(T)$.

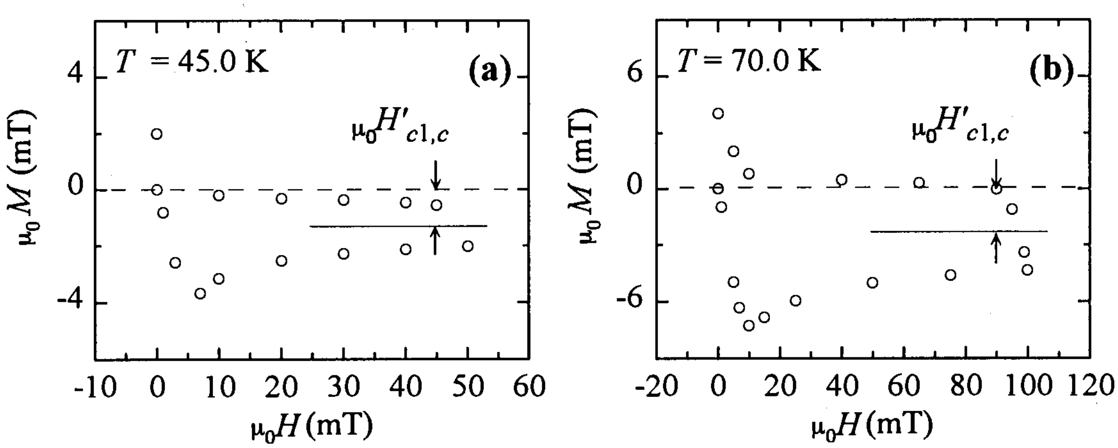

FIG. 6.3. Initial and hysteresis curves of (a) sample B1 [$YBa_2Cu_{1-y}Co_yO_{7-\delta}$ ($y = 0.2$)] at 45.0 K and (b) sample B5 [$Y_{1-x}Ca_xBa_2Cu_3O_{7-\delta}$ ($x = 0.2$)] at 70.0 K, where the applied magnetic field is parallel to the c axis.

III. RESULTS AND DISCUSSION

As have been revealed in Chap. 3, the temperature dependences of $H_{c1,c}$ of Bi2212 and Y123 are

$$H_{c1,c}(T) = H_{c1,c}(0)[1-(T/T_c)^{2.6}] \qquad (H \parallel c \text{ axis of Bi2212}), \tag{6.4}$$

$$H_{c1,c}(T) = H_{c1,c}(0)[1-(T/T_c)^{1.0}] \qquad (H \parallel c \text{ axis of Y123}). \tag{6.5}$$

Assuming Y/Pb-doped Bi2212 and Co/Ca-doped Y123 have similar temperature dependences to undoped specimens (A2, B2), we plot in Fig. 6.4(a) $\mu_0 H_{c1,c}$ of samples A1 – A3 versus $1-(T/T_c)^{2.6}$ and in Fig. 6.4(b) $\mu_0 H_{c1,c}$ of samples B1 – B5 versus $1-T/T_c$.

By a least-squares fitting and extrapolating the fitting curves to $T=0$, we obtain $\mu_0 H_{c1,c}(0)$ for each sample. Using the values of $H_{c1,c}(0)$ thus determined, we plot T_c versus $\mu_0 H_{c1,c}(0)$ ($\propto n_s/m^*$) in Figs. 6.5(a) and (b). The figures show that T_c takes nearly the maximum value around $H_{c1,c}(0)$ for undoped specimens. In the overdoped region, however, T_c tends to decrease as $H_{c1,c}(0)$ increases.

This trend found here is qualitatively similar to those obtained by means of μSR measurements [170], although direct comparison of the data in terms of $H_{c1,c}(0)$ and the μSR rate σ cannot be made (see Fig. 6.6).

Present results indicate that the correlation between T_c and n_s/m^* can be successfully made in terms of lower critical fields and this technique is much more simple compared with the conventional methods including μSR measurements.

Recently, very stimulative works were successively published. Niedermayer *et al.* [172] and Uemura *et al.* [173] independently carried out the systematic μSR measurements for the strongly overdoped $Tl_2Ba_2CuO_{6+\delta}$ (Tl2201) prepared by annealing at various oxygen partial pressures, and showed that n_s/m^* falls to zero as T_c suppressed in overdoped specimens in which the normal-state charge-carrier concentration increases as T_c decreases (see Fig. 6.7). On this incompatible results with the BCS picture, the former group argues that their data are explicable in terms of pair breaking and complements a growing body of evidence for the prominence of pair breaking, and nearly gapless superconductivity in the high-T_c cuprate.

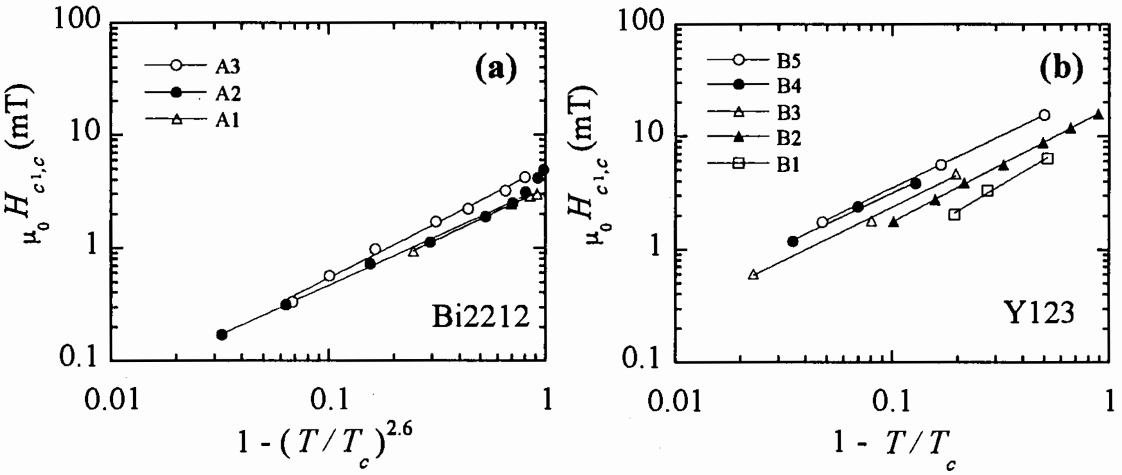

FIG. 6.4. Temperature dependence of lower critical fields of (a) Bi2212 and (b) Y123 single crystals.

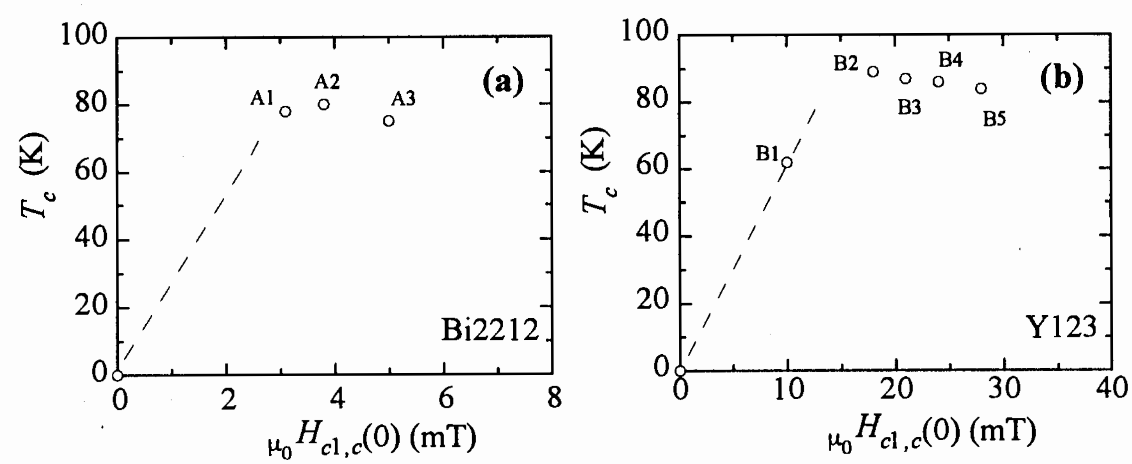

FIG. 6.5. Relation between T_c and the lower critical field $\mu_0 H_{c1,c}(0)$ of Y123 and Bi2212 single crystals.

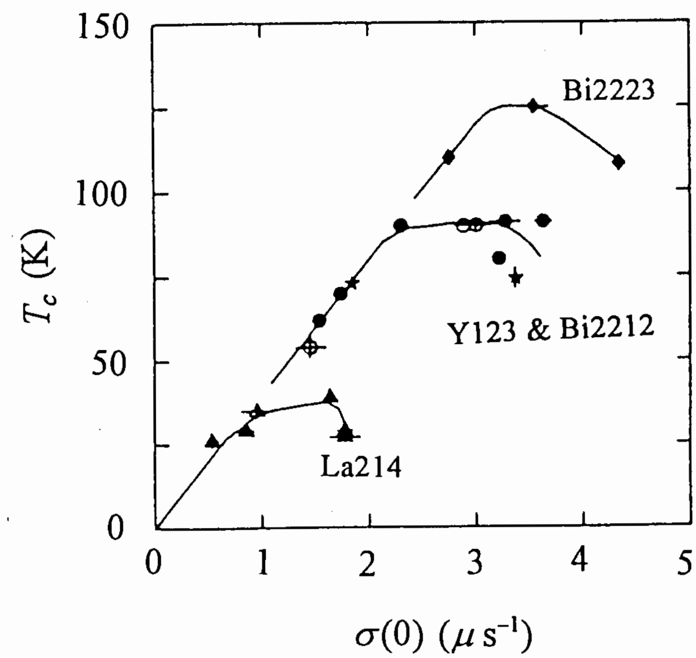

FIG. 6.6. T_c versus low-temperature μSR rate $\sigma(0)$ measured in different specimens of cuprate superconductors [170]. The horizontal axis $\sigma(0)$ is proportional to $1/\lambda_{ab}^2$ and consequently to n_s/m^*.

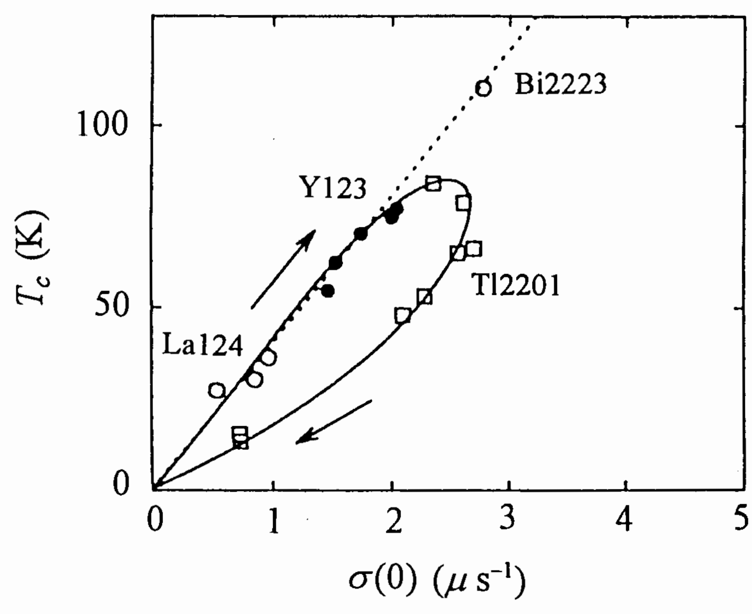

FIG. 6.7. Relation between T_c and the depolarization rate $\sigma(0)$. Open squares indicate data on Tl2201 extending into the overdoped region [172, 173]. Open and closed circles represent data on La214, Y123, and Bi2223 [170].

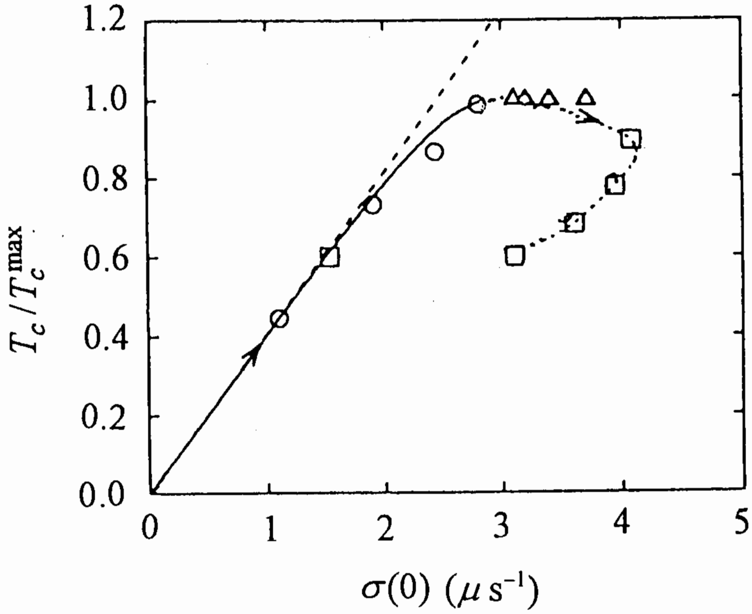

FIG. 6.8. T_c/T_c^{max} versus the low-temperature depolarization rate $\sigma(0)$ for a variety of polycrystalline Y123, $Y_2Ba_4Cu_7O_{15-\delta}$, and $YBa_2Cu_4O_8$ [174].

More recently, Niedermayer and his co-workers [174] extended their μSR measurements to a variety of polycrystalline Y123, $Y_2Ba_4Cu_7O_{15-\delta}$, and $YBa_2Cu_4O_8$ (see Fig. 6.8). In preparations of the heavily doped samples, Ca substitution allows the doping on the planes and chains to be independently controlled. From obtained μSR data, they showed that, when these chains are free of disorder, the superconducting condensate density originating in the CuO_2 planes is greatly enhanced due to the additional carriers on these chains condensing as Cooper pairs. That is, the CuO chains become superconducting by proximity to the intrinsically superconducting planes providing significant enhancement in the condensate density. Moreover, they argue that pair breaking on oxygen-deficient chains could provide the low-energy excitations deduced from several studies, without having to invoke d-wave symmetry.

Unfortunately, in the present $H_{c1,c}$ measurements, the heavily overdoped samples were not available. Nevertheless, we believe the present technique would provide another useful tool for further investigations on this interesting topic. Measurements of $H_{c1,c}$ for strongly overdoped systems are desired.

IV. CONCLUSIONS

We measured the magnetization curves of Y/Pb-doped Bi2212 and Co/Ca-doped Y123 single crystals at various temperatures below T_c, where we used SQUID and the applied field was parallel to the c axis. The samples were prepared by the self-flux method and characterized in terms of complex susceptibilities and Raman spectra. On the basis of our theoretical study described in Chap. 2, we determined $\mu_0 H_{c1,c}$ and plotted as a function of temperature; $H_{c1,c}(T) = H_{c1,c}(0)[1-(T/T_c)^{2.6}]$ for the Bi2212 group and $H_{c1,c}(T) = H_{c1,c}(0)(1-T/T_c)$ for the Y123 group, where corrections for the demagnetization effect were made. By a least-squares fitting and extrapolating the fitting curve to $T = 0$, we obtained $H_{c1,c}(0)$ for each sample.

From the GL theory together which the London theory, it is known that $H_{c1,c}(0)$ is proportional to the superconducting carrier density n_s divided by the effective electron mass m^*. Plots of $H_{c1,c}(0)$ ($\propto n_s/m^*$) versus T_c have revealed that these samples show a well known universal feature of the high-T_c superconductors, i.e., the existence of a chemical composition that gives a maximum transition temperature, separating the so-called underdoped and overdoped regimes. Comparison with the previous researches on the correlation between the critical temperature and the carrier density indicates that the present method in terms of lower critical fields is applicable as a new technique for further investigations of this topic. Measurements of H_{c1} for a strongly overdoped specimen is desired to bring to light the specific dependence of T_c on n_s/m^* recently reported for Tl2201 and Y123 systems.

Chapter 7

Conclusion

In this thesis, we have investigated the magnetic response of cuprate-based oxide superconductors both theoretically and experimentally.

In Chap. 2, the magnetization equations for type-II superconductors located in an ac magnetic field superimposed on a dc field have been thoroughly derived within the construct of the modified Kim–Anderson (KA) model, where surface barriers ΔH and lower critical fields H_{c1} are explicitly taken into consideration.

Applying the magnetization equations thus derived, we studied in Chap. 3 the temperature dependence of H_{c1} for $Bi_2Sr_2CaCu_2O_{8+\delta}$ (Bi2212) and $YBa_2Cu_3O_{7-\delta}$ (Y123) single crystals. Anomalous temperature dependence of H_{c1} of Bi2212 in the lower temperature region has been attributed to a proximity effect induced in the normal layer between the CuO_2 planes as well as to the correlation between the coherence length and the large lattice spacing of Bi2212. In addition, penetration-depth ratios calculated using a theory based on incoherent quasiparticle hopping have revealed that both Bi2212 and Y123 possess the nature of d-wave pairings.

In order to apply the magnetization equations derived in Chap. 2 for investigations of ΔH, in Chap. 4, we treated complex magnetic susceptibilities χ_n generated from a superconductor located in a time-dependent magnetic field. Then, the forms of temperature dependence of the material parameters k and B_0 involved in the KA model have been determined.

In Chap. 5, we have studied ΔH of Bi2212 and Y123 (thin film and bulk) in terms of χ_n. Experimentally obtained χ_n as a function of temperature are analyzed in the framework of the modified KA model, where k, B_0, ΔH, and H_{c1} are used as fitting parameters. From the results, we have found a remarkable difference between ΔH's of Bi2212 and Y123. $\mu_0 \Delta H$ for single-crystal Bi2212 has a similar value found for thin films, 0.5 mT, while $\mu_0 \Delta H$ for single-crystal Y123 is as large as 80 mT which would be attributed to the Bean–Livingston barrier.

Finally, in Chap. 6, we measured H_{c1} of Y/Pb-doped Bi2212 and Co/Ca-doped Y123 single crystals at various temperatures below the critical temperature T_c. Plots of $H_{c1} \propto n_s/m^*$ versus T_c have revealed that these samples show a well-known universal feature of high-T_c superconductors, where n_s is the superconducting carrier density and m^* is the effective mass. Comparison with the previous researches on the correlation between T_c and n_s indicates that the present method in terms of H_{c1} is applicable as a new technique for further investigations of this attractive topic.

References

[1] H.K. Onnes, van Wetenschappen **14**, 113, 818 (1911).

[2] W. Meissner and R. Ochsenfeld, Naturwissenshaften **21**, 787 (1933).

[3] F. London and H. London, Proc. Roy. Soc. (London) A **149**, 71 (1935).

[4] V.L. Ginzburg and L.D. Landau, Sov. Phys. – JETP **20**, 1064 (1950).

[5] A.B. Pippard, Proc. Roy. Soc. (London) A **216**, 547 (1953).

[6] J.G. Bardeen, L.N. Cooper, and J.R. Schrieffer, Phys. Rev. **108**, 1175 (1957).

[7] N.N. Bogoliubov, Sov. Phys. – JETP **34**, 41 (1958).

[8] L.P. Gor'kov, Sov. Phys. – JETP **36**, 1364 (1959).

[9] A.A. Abrikosov, Sov. Phys. – JETP **32**, 1442 (1957).

[10] G. Bednorz and K.A. Müller, Z. Phys. B **64**, 189 (1986).

[11] M.K. Wu, J.R. Ashburn, C.J. Torng, P.H. Hor, R.L. Meng, L. Gao, Z.J. Huang, Y.Q. Wang, and C.W. Chu, Phys. Rev. Lett. **58**, 908 (1987).

[12] A. Schilling, M. Cantoni, J.D. Guo, and H.R. Ott, Nature **363**, 56 (1993).

[13] C. Park and R.L. Snyder, J. Am. Ceram. Soc. **78**, 3171 (1995).

[14] M. Kakihana, M. Osada, M. Käll, L. Börjesson, H. Mazaki, H. Yasuoka, M. Yashima, and M. Yoshimura, Phys. Rev. B **53**, 11796 (1996).

[15] M. Kakihana, L. Börjesson, S. Eriksson, P. Svedlindh, and P. Norling, Phys. Rev. B **40**, 6787 (1989).

[16] C.P. Bean, Phys. Rev. Lett. **8**, 250 (1962).

[17] Y.B. Kim, C.F. Hempstead, and A.R. Strnad, Phys. Rev. Lett. **9**, 306 (1962).

[18] Y.B. Kim, C.F. Hempstead, and A.R. Strnad, Phys. Rev. **129**, 528 (1963).

[19] P.W. Anderson, Phys. Rev. Lett. **9**, 309 (1962).

[20] D.X. Chen and R.B. Goldfarb, J. Appl. Phys. **66**, 2489 (1989).

[21] J.H. Watson, J. Appl. Phys. **39**, 3406 (1968).

[22] C.P. Bean, Rev. Mod. Phys. **36**, 31 (1964).

[23] H. London, Phys. Lett. **6**, 162 (1963).

[24] F. Irie and K. Yamafuji, J. Phys. Soc. Jpn. **23**, 255 (1967).

[25] I.M. Green and P. Hlawiczka, Proc. Inst. Elec. Engi. **114**, 1329 (1967).

[26] S. Tochihara, H. Yasuoka, and H. Mazaki, Physica C **268**, 241 (1996).

[27] S. Tochihara, H. Yasuoka, and H. Mazaki, Physica C **295**, 101 (1998).

[28] K. Yamamoto, H. Mazaki, and H. Yasuoka, Phys. Rev. B **47**, 915 (1993).

[29] K. Yamamoto, H. Mazaki, H. Yasuoka, S. Katsuyama, and K. Kosuge, Phys. Rev. B **46**, 1122 (1992).

[30] H. Yasuoka, H. Mazaki, N. Koide, M. Kakihana, and M. Yoshimura, Advances in Superconductivity **V**, 179 (1993).

[31] H. Yasuoka, T. Koga, and H. Mazaki, Physica C **235–240**, 3195 (1994).

[32] H. Mazaki, H. Yasuoka, M. Kakihana, H. Fujimori, M. Yashima, and M. Yoshimura, Physica C **252**, 275 (1995).

[33] C.P. Bean and J.D. Livingston, Phys. Rev. Lett. **12**, 14 (1964).

[34] W.I. Dunn and P. Hlawiczka, Brit. J. Appl. Phys. **1**, 1469 (1968).

[35] J.R. Clem, J. Appl. Phys. **50**, 3518 (1979).

[36] A. Fortini, A. Hairie, and E. Paumier, Phys. Rev. B **21**, 5065 (1980).

[37] T.R. McGuire, T.R. Dinger, P.J.P. Freitas, W.J. Gallagher, T.S. Plaskett, R.L. Standstorm, and T.M. Shaw, Phys. Rev. B **36**, 4032 (1987).

[38] A. Umezawa, G.W. Crabtree, J.Z. Liu, T.J. Moran, S.K. Malik, L.H. Munez, W.L. Kwok, and C.H. Sowers, Phys. Rev. B **38**, 2843 (1988).

[39] T.T.M. Palstra, B. Batlogg, R.B. van Dover, L.F. Schneemeyer, and J.V. Waszczak, Appl. Phys. Lett. **54**, 763 (1989).

[40] L. Burlachkov, M. Konczykowski, Y. Yeshurun, and F. Holtzberg, J. Appl. Phys. **70**, 5759 (1991).

[41] N. Chikumoto, M. Konczykowski, N. Motohira, and A.P. Malozemoff, Phys. Rev. Lett. **69**, 1260 (1992).

[42] F. Zuo, D. Vacaru, H.M. Duan, and A.M. Hermann, Phys. Rev. B **47**, 5535 (1993).

[43] R. Kato, Y. Enomoto, and S. Maekawa, Phys. Rev. B **47**, 8016 (1993).

[44] L. Burlachkov, Phys. Rev. B **47**, 8056 (1993).

[45] Th. Schuster, M.V. Indenbom, H. Kuhn, E.H. Brandt, and M. Konczykowski, Phys. Rev. Lett. **73**, 1424 (1994).

[46] M. Xu, D.K. Finnemore, G.W. Crabtree, V.M. Vinokur, B. Dabrowski, D.G. Hinks, and K. Zhang, Phys. Rev. B **48**, 10630 (1993).

[47] E. Zeldov, J.R. Clem, M. McElfresh, and M. Darwin, Phys. Rev. B **49**, 9802 (1994).

[48] E. Zeldov, A.I. Larkin, V.B. Geshkenbein, M. Konczykowski, D. Majer, B. Khaykovich, V.M. Vinokur, and H. Shtrikman, Phys. Rev. Lett. **73**, 1428 (1994).

[49] M.V. Indenbom, G. D'Anna, M.O. André, V.V. Kabanov, and W. Benoit, Physica C **235–240**, 201 (1994).

[50] E. Zeldov, D. Majer, M. Konczykowski, A.I. Larkin, V.M. Vinokur, V.B. Geshkenbein, N. Chikumoto, and H. Shtrikman, Europhys. Lett. **30**, 367 (1995).

[51] C.J. van der Beek, M.V. Indenbom, G. D'Anna, and W. Benoit, Physica C **258**, 105 (1996).

[52] M. Benkraouda and J.R. Clem, Phys. Rev. B **53**, 5716 (1996).

[53] L. Burlachkov, A.E. Koshelev, and V.M. Vinokur, Phys. Rev. B **54**, 6750 (1996).

[54] R. Labusch and T.B. Doyle, Physica C **290**, 143 (1997).

[55] T.B. Doyle, R. Labusch, and R.A. Doyle, Physica C **290**, 148 (1997).

[56] M.S. James, S.T. Stoddart, S.J. Bending, S. Aukkaravittayapun, P.J. King, and M. Henini, Phys. Rev. B **56**, R5771 (1997).

[57] M. Benkraouda and J.R. Clem, Phys. Rev. B **58**, 15103 (1998).

[58] C. Rettori, D. Davidov, I. Belaish, and I. Felner, Phys. Rev. B **36**, 4028 (1987).

[59] B. Batlogg, T.T.M. Palstra, L.F. Schneemeyer, R.B. van Dover, and R.J. Cava, Physica C **153–155**, 1062 (1988).

[60] N. Kobayashi, H. Iwasaki, S. Terada, K. Noto, A. Tokiwa, M. Kikuchi, Y. Syono, and Y. Muto, Physica C **153–155**, 1525 (1988).

[61] J.P. Ströbel, A. Thomä, B. Hensel, H. Adrian, and G. Saemann–Ischenko, Physica C **153–155**, 1537 (1988).

[62] S. Sridhar, D.H. Wu, and W. Kennedy, Phys. Rev. Lett. **63**, 1873 (1989).

[63] H. Adrian, W. Assmus, A. Höhr, J. Kowalewski, H. Spille, and F. Steglich, Physica C **162–164**, 329 (1989).

[64] L. Krusin–Elbaum, A.P. Malozemoff, Y. Yeshurum, D.C. Cronemeyer, and F. Holtzberg, Phys. Rev. B **39**, 2936 (1989).

[65] M.W. McElfresh, Y. Yeshurun, A.P. Malozemoff, and F. Holtzberg, Physica A **168**, 308 (1990).

[66] M. Naito, A. Matsuda, K. Kitazawa, S. Kambe, I. Tanaka, and H. Kojima, Phys. Rev. B **41**, 4823 (1990).

[67] D.H. Wu and S. Sridhar, Phys. Rev. Lett. **65**, 2074 (1990).

[68] D.S. Hirashima and T. Matsuura, J. Phys. Soc. Jpn. **59**, 24 (1990).

[69] T. Koyama, N. Takezawa, and M. Tachiki, Physica B **165&166**, 1105 (1990).

[70] M. Konczykowski, L.I. Burlachkov, Y. Yeshurun, and F. Holtzberg, Phys. Rev. B **43**, 13707 (1991).

[71] J.R. Clem, M.W. Coffey, and Z. Hao, Phys. Rev. B **44**, 2732 (1991).

[72] J.R. Clem, Supercond. Sci. Technol. **5**, S33 (1992).

[73] L. Burlachkov, Y. Yeshurun, M. Konczykowski, and F. Holtzberg, Phys. Rev. B **45**, 8193 (1992).

[74] D.X. Chen, R.B. Goldfarb, R.W. Cross, and A. Sanchez, Phys. Rev. B **48**, 6426 (1993).

[75] D.N. Zheng, A.M. Campbell, J.D. Johnson, J.R. Cooper, F.J. Blunt, A. Porch, and P.A. Freeman, Phys. Rev. B **49**, 1417 (1994).

[76] M. Nideröst, R. Frassanito, M. Saalfrank, A.C. Mota, G. Blatter, V.N. Zavaritsky, T.W. Li, and P.H. Kes, Phys. Rev. Lett. **81**, 3231 (1998).

[77] S. Takahashi and M. Tachiki, Phys. Rev. B **33**, 4620 (1986).

[78] Y. Xu and W. Guan, Appl. Phys. Lett. **53**, 334 (1988).

[79] P. Berastegui, S.G. Eriksson, L.G. Johansson, M. Kakihana, M. Osada, H. Mazaki, and S. Tochihara, J. Solid. State. Chem. **127**, 56 (1996).

[80] J.A. Osborn, Phys. Rev. **67**, 351 (1945).

[81] A.L. Fetter and P.C. Hohenberg, Phys. Rev. **159**, 330 (1967).

[82] D.R. Harshman, R.N. Kleiman, M. Inui, G.P. Espinosa, D.B. Mitzi, A. Kapitulnik, T. Pfiz, and D.L. Williams, Phys. Rev. Lett. **67**, 3152 (1991).

[83] D.R. Harshman, L.F. Schneemeyer, J.V. Waszczak, G. Aeppli, R.J. Cava, B. Batlogg, L.W. Rupp, E.J. Ansaldo, and D.Ll. Williams, Phys. Rev. B **39**, 851 (1989).

[84] U. Welp, W.K. Kwok, G.W. Crabtree, K.G. Vandervoort, and J.Z. Liu, Phys. Rev. Lett. **62**, 1908 (1989).

[85] J.R. Cooper, L. Ferro, and B. Keszei, Nature **243**, 444 (1990).

[86] R.J. Radtke, V.N. Kostur, and K. Levin, Phys. Rev. B **53**, R522 (1996).

[87] N.R. Werthamer, in "Superconductivity", ed. by R.D. Parks, **Vol. 1**, p.321 (Dekker, New York, 1969).

[88] H. Mazaki, Y. Ueda, Y. Aihara, T. Kubozoe, and K. Kosuge, Jpn. J. Appl. Phys. **28**, L368 (1989).

[89] T. Ishida and H. Mazaki, Jpn. J. Appl. Phys. **26**, L2003 (1987).

[90] J. Takada, Y. Bando, and H. Mazaki, Appl. Phys. Lett. **53**, 332 (1988).

[91] D.R. Harshman and A.P. Mills, Jr., Phys. Rev. B **45**, 10684 (1992).

[92] M. Däumling and G.V. Chandrashekhar, Phys. Rev. B **46**, 6422 (1992).

[93] W.N. Hardy, D.A. Bonn, D.C. Morgan, R. Liang, and K. Zhang, Phys. Rev. Lett. **70**, 3999 (1993).

[94] T. Shibauchi, H. Kitano, K. Uchinokura, A. Maeda, T. Kimura, and K. Kishio, Phys. Rev. Lett. **72**, 2263 (1994).

[95] J. Mao, D.H. Wu, J.L. Peng, R.L. Greene, and S.M. Anlage, Phys. Rev. B **51**, 3316 (1995).

[96] E. Roddick and D. Stroud, Phys. Rev. Lett. **74**, 1430 (1995).

[97] J.N. Li, K. Kadowaki, M.J.V. Menken, Y.K. Huang, K. Bakker, A.A. Menovsky, and J.J.M. Franse, Appl. Phys. A **47**, 209 (1988).

[98] A. Yamamoto, M. Onoda, E. Takayama–Muromachi, F. Izumi, T. Ishigaki, and H. Asano, Phys. Rev. B **42**, 4228 (1990).

[99] J.D. Jorgensen, B.W. Veal, A.P. Paulikas, L.J. Nowicki, G.W. Crabtree, H. Claus, and W.K. Kwok, Phys. Rev. B **41**, 1863 (1990).

[100] K. Kanoda, H. Mazaki, T. Yamada, N. Hosoito, and T. Shinjo, Phys. Rev. B **33**, 2052 (1986).

[101] K. Kanoda, H. Mazaki, N. Hosoito, and T. Shinjo, Phys. Rev. B **35**, 6736 (1987).

[102] T. Ishida and H. Mazaki, J. Appl. Phys. **52**, 6798 (1981).

[103] R.W. Rollins and J. Silcox, Phys. Rev. **155**, 404 (1967).

[104] L. Hartshorn, J. Sci. Instrum. **2**, 145 (1925).

[105] H. Yasuoka, S. Tochihara, M. Mashino, and H. Mazaki, Physica C **305**, 125 (1998).

[106] H. Mazaki, K. Yamamoto, and H. Yasuoka, in "Magnetic Susceptibilities of Superconductors and Other Spin Systems", ed. by R.A. Hein, T.L. Francavilla, and D.H. Liebenberg, p.333 (Plenum Press, New York 1991).

[107] S. Tochihara, K. Harashima, H. Yasuoka, and H. Mazaki, J. Jpn. Soc. Powder and Powder Metallurgy **44**, 787 (1997).

[108] H. Mazaki, M. Takano, R. Kanno, and Y. Takeda, Jpn. J. Appl. Phys. **26**, L780 (1987).

[109] M. Kakihana, J. Sol-Gel Sci. & Technol. **6**, 7 (1996).

[110] T. Terashima, K. Iijima, K. Yamamoto, Y. Bando, and H. Mazaki, Jpn. J. Appl. Phys. **27**, L91 (1988).

[111] K. Yamamoto, H. Mazaki, H. Yasuoka, T. Terashima, and Y. Bando, Physica C **192**, 47 (1992).

[112] Y.B. Kim, C.F. Hempstead, and A.R. Strnad, Phys. Rev. **131**, 2486 (1963).

[113] J.A. Hulbert, Brit. J. Appl. Phys. **16**, 1657 (1965).

[114] S. Jin, T.H. Tiefle, R.C. Sherwood, G.W. Kammlott, and S.M. Zahurak, Appl. Phys. Lett. **51**, 953 (1987).

[115] S. Jin, T.H. Tiefle, R.C. Sherwood, R.B. van Dover, M.E. Davis, G.W. Kammlott, and R.A. Fastnacht, Phys. Rev. B **37**, 7850 (1988).

[116] M. Murakami, M. Morita, K. Doi, and K. Miyamoto, Jpn, J. Appl. Phys. **28**, 1189 (1989).

[117] M. Murakami, M. Morita, and N. Koyama, Jpn. J. Appl. Phys. **28**, L1125 (1989).

[118] N. Ogawa, I. Hirabayashi, and S. Tanaka, Physica C **177**, 101 (1991).

[119] W.A. Fietz, M.R. Besaley, J. Silcox, and W.W. Webb, Phys. Rev. **136**, A335 (1964).

[120] G. Xiao, F.H. Streitz, A. Gavrin, M.Z. Cieplak, J. Chidress, M. Lu, A. Zwicker, and C.L. Chien, Phys. Rev. B **36**, 2382 (1987).

[121] Y. Yeshurun and A.P. Malozemoff, Phys. Rev. Lett. **60**, 2202 (1988).

[122] P.L. Gammel, L.F. Schneemeyer, J.V. Waszczak, and D.J. Bishop, Phys. Rev. Lett. **61**, 1666 (1988).

[123] K.A. Müller, M. Takashige, and J.G. Bednorz, Phys. Rev. Lett. **58**, 1143 (1987).

[124] H. Mazaki, K. Yamamoto, and H. Yasuoka, Proceedings of the 6th Int. Conf. on Ferrites, ICF 6, 601 (1992).

[125] M. Murakami, S. Gotoh, N. Koshizuka, S. Tanaka, T. Matsushita, S. Kambe, and K. Kitazawa, Cryogenics **30**, 390 (1990).

[126] P.J. Kung, M.P. Maley, M.E. McHenry, J.O. Willis, M. Murakami, and S. Tanaka, Phys. Rev. B **48**, 13922 (1993).

[127] M. Tinkham, Introduction to Superconductivity, (McGraw-Hill, New York, 1975).

[128] M. Murakami, H. Fujimoto, S. Gotoh, K. Yamaguchi, N. Koshizuka, and S. Tanaka, Physica C **185–189**, 321 (1991).

[129] A.M. Cambell and J.E. Evetts, Adv. Phys. **21**, 199 (1972).

[130] M.V. Feigel'man, V.B. Geshkenbein, A.I. Larkin, and V.M. Vinokur, Phys. Rev. Lett. **63**, 2303 (1989).

[131] E.V. Thuneberg, J. Kurkijärvi, and D. Rainer, Phys. Rev. Lett. **48**, 1853 (1982).

[132] E.V. Thuneberg, J. Kurkijärvi, and D. Rainer, Phys. Rev. B **29**, 3913 (1984).

[133] E.M. Chudnovsky, Phys. Rev. Lett. **65**, 3060 (1990).

[134] R. Labusch, Crystal Lattice Defects **1**, 1 (1969).

[135] T. Matsushita, E.S. Otabe, B. Ni, K. Kimura, M. Morita, M. Tanaka, M. Kimura, K. Miyamoto, and K. Sawano, Jpn. J. Appl. Phys. **30**, L342 (1991).

[136] K. Yamamoto, H. Mazaki, H. Yasuoka, T. Terashima, and Y. Bando, Jpn. J. Appl. Phys. **31**, 770 (1992).

[137] A.P. Malozemoff, T.K. Worthington, Y. Yeshurun, and F. Holtzberg, Phys. Rev. B **48**, 7203 (1988).

[138] C.C. Almasan, M.C. de Andrade, Y. Dalichaouch, J.J. Neumeier, C.L. Seaman, M.B. Maple, R.P. Guertin, M.V. Kuric, and J.C. Garland, Phys. Rev. Lett. **69**, 3812 (1992).

[139] Y. Xu and M. Suegawa, Phys. Rev. B **43**, 5516 (1991).

[140] A. Gupta, Y. Kopelevich, M. Ziese, P. Esquinazi, P. Fischer, F.I. Schulz, and H.F. Braun, Phys. Rev. B **48**, 6359 (1993).

[141] H. Yasuoka, S. Tochihara, Y. Tanaka, and H. Mazaki, Physica C **282–287**, 2211 (1997).

[142] M.R. Beasley, R. Labusch, and W.W. Webb, Phys. Rev. **181**, 682 (1969).

[143] A. Houghton, R.A. Pelcovits, and A. Subdø, Phys. Rev. B **40**, 6763 (1989).

[144] F. Lindemann, Phys. Z. **11**, 69 (1910).

[145] D.S. Fisher, Phys. Rev. B **22**, 1190 (1980).

[146] E.H. Blant, J. Low Temp. Phys. **26**, 709 (1977).

[147] E.H. Blant, J. Low Temp. Phys. **26**, 735 (1977).

[148] E.H. Blant, J. Low Temp. Phys. **28**, 263 (1977).

[149] E.H. Blant, J. Low Temp. Phys. **28**, 291 (1977).

[150] M.P.A. Fisher, Phys. Rev. Lett. **62**, 1415 (1989).

[151] D.S. Fisher, M.P.A. Fisher, and D.A. Huse, Phys. Rev. B **43**, 130 (1991).

[152] T.K. Worthington, M.P.A. Fisher, D.A. Huse, J. Toner, A.D. Marwick, T. Zabel, C.A. Field, and F. Holtzberg, Phys. Rev. B **46**, 11854 (1992).

[153] M. Konczykowsky, F. Rullier–Albenque, E.R. Yacoby, A. Shaulov, Y. Yeshurun, and P. Lejay, Phys. Rev. B **44**, 7167 (1991).

[154] M. Konczykowsky, V.M. Vinokur, F. Rullier–Albenque, Y. Yeshurun, and F. Holtzberg, Phys. Rev. B **47**, 5531 (1993).

[155] L.M. Paulius, J.A. Fendrich, W.K. Kwok, A.E. Koshelev, V.M. Vinokur, G.W. Crabtree, and B.G. Glagola, Phys. Rev. B **56**, 913 (1997).

[156] G.D. Cody and G.W. Cullen, Conf. on Type II Superconductivity, Cleveland, IV-14-IV-37 (1964).

[157] G.B. Mardion, B.B. Goodman, and A. Lacaze, Phys. Lett. **2**, 321 (1962).

[158] T. Kinsel, E.A. Lynton, and B. Serin, Phys. Lett. **3**, 30 (1962).

[159] J.D. Livingston, Phys. Rev. **129**, 1943 (1963).

[160] J.D. Livingston, Int. Conf. on the Science of Superconductibity, New York (1963).

[161] A.I. Larkin and Y.N. Ovchinnikov, Sov. Phys. – JETP **34**, 651 (1972).

[162] R.P. Huebener, R.T. Kampwirth, and J.R. Clem, J. Low Temp. Phys. **6**, 275 (1972).

[163] Y. Tokura, in "Physics of High-Temperature superconductors", ed. by S. Maekawa and M. Sato, (Springer-Verlag, 1992).

[164] See, for a review, J.S. Schilling and S. Klotz, in "Physical Properties of High Temperature Superconductors III", ed. by D.M. Ginzburg, p.59 (World Scientific, Singapore, 1992), or H. Takahashi, N. Môri, M. Azuma, Z. Hiroi, and M. Takano, Physica C **227**, 395 (1994).

[165] M. Osada, Thesis, Tokyo Institute of Technology, (1998).

[166] M. Kakihana, S.G. Eriksson, L. Börjesson, L.G. Johansson, C. Ström, and M. Käll, Phys. Rev. B **47**, 5359 (1993).

[167] P. Berastegui, M. Kakihana, S.G. Eriksson, S. Nishio, H. Mazaki, H. Yasuoka, M. Osada, M. Yashima, and M. Yoshimura, Physica C **235–240**, 377 (1994).

[168] Y.J. Uemura, V.J. Emery, A.R. Moodenbaugh, M. Suenaga, D.C Johnston, A.J. Jacobson, J.T. Lewandowski, J.H. Brewer, R.F. Kiefl, S.R. Kreitzman, G.M. Luke, T. Riseman, C.E. Stronach, W.J. Kossler, J.R. Kempton, X.H. Yu, D. Opie, and H.E. Schone, Phys. Rev. B **38**, 909 (1988).

[169] W.J. Kossler, J.R. Kempton, X.H. Yu, H.E. Schone, Y.J. Uemura, A.R. Moodenbaugh, M. Suenaga, and C.E. Stronach, Phys. Rev. B **35**, 7133 (1987).

[170] Y.J. Uemura, G.M. Luke, B.J. Sternlieb, J.H. Brewer, J.F. Carolan, W.N. Hardy, R. Kadono, J.R. Kempton, R.F. Kiefl, S.R. Krietzman, P. Mulhern, T.M. Riseman, D. Ll. Williams, B.X. Yang, S. Uchida, H. Takagi, J. Gopalakrishnan, A.W. Sleight, M.A. Subramanian, C.L. Chien, M.Z. Cieplak, G. Xiao, V.Y. Lee, B.W. Statt, C.E. Stronach, W.J. Kossler, and X.H. Yu, Phys. Rev. Lett. **62**, 2317 (1989).

[171] R. Jayavel, A. Thamizhavel, P. Murugakoothan, and P. Ramasamy, Physica C **215**, 429 (1992).

[172] Ch. Niedermayer, C. Bernhard, U. Binninger, H. Gluckler, J.L. Tallon, E.J. Ansaldo, and J.I. Budnick, Phys. Rev. Lett. **71**, 1764 (1993).

[173] Y.J. Uemura, A. Keren, L.P. Le, G.M. Luke, W.D. Wu, Y. Kubo, T. Manako, Y. Shimakawa, M. Subramanian, J.L. Cobb, and J.T. Markert, Nature **364**, 605 (1993).

[174] J.L. Tallon, C. Bernhard, U. Binninger, A. Hofer, G.V.M. Williams, E.J. Ansaldo, J.I. Budnick, and Ch. Niedermayer, Phys. Rev. Lett. **74**, 1008 (1995).

Acknowledgments

The present thesis has been submitted to the Tokyo Institute of Technology for the degree of Doctor. This work has been performed in the Department of Mathematics and Physics, the National Defense Academy, from April 1995 to November 1999.

The author would like to acknowledge sincerely to Dean of the Graduate School, Professor Hiromasa Mazaki of the National Defense Academy, for his exhaustive instruction and continuous support throughout the duration of this work.

He would also like to express his gratitude to Professor Hiroshi Yasuoka of the National Defense Academy for many stimulating suggestions, and to Professor Masato Kakihana and Professor Masahiro Yoshimura of the Tokyo Institute of Technology, and Dr. Minoru Osada of the Institute of Physical and Chemical Research, especially for their kind cooperation in sample preparations. Without their support and suggestions, this project would not have been completed.

Emeritus Professor Yoshichika Bando, Professor Mikio Takano, and Dr. Takahito Terashima of Kyoto University, Mr. Motoharu Komatsu of Tohoku Electric Power Co., Inc., and Dr. Megumi Hirota of Technology Research and Development Institute of Japan Defense Agency are acknowledged for their kind offer of the samples. Special thanks are due to Dr. Shinya Sawai and Mr. Masami Mashino of the National Defense Academy for many hard hours of LaTeX 2_ε training.

The author would like to acknowledge General Toshio Tamogami, Col. Hideki Akai, Lt. Col. Dr. Hidehiko Kaneko, and Cap. Naoya Kaneko for their warmful encouragement during his stay in the Academy.

Finally, the author is grateful to the staff of the Department of Mathematics and Physics of the National Defense Academy for their kind support and to the coworkers in the Laboratory for their assistance in measurements.

List of Publications

(1) Relevant Papers and Proceedings

1. S. Tochihara, H. Yasuoka, and H. Mazaki, "Magnetization of type-II superconductors in the modified Bean model", Physica C **268**, 241–256 (1996).
2. 栃原信二郎, 安岡宏, 間崎啓匡, 小松基張, 永野貢, "MBE法で作成した $YBa_2Cu_3O_{7-d}$ 単結晶薄膜の高調波複素帯磁率", 粉体および粉末冶金 **43**, 1070–1075 (1996).
3. S. Tochihara, K. Harashima, H. Yasuoka, and H. Mazaki, "Magnetic response of a single-crystal thin film $Bi_2Sr_2CaCu_2O_y$", Journal of the Japan Society of Powder and Powder Metallurgy **44**, 787–791 (1997).
4. S. Tochihara, H. Yasuoka, and H. Mazaki, "Effect of surface barriers and lower critical fields to magnetization of type-II superconductors", Physica C **295**, 101–125 (1998).
5. S. Tochihara, K. Harashima, H. Yasuoka, H. Mazaki, M. Osada, and M. Kakihana, "Effect of lower critical fields on magnetization of a single-crystal $Bi_2Sr_2CaCu_2O_{8+d}$ bulk superconductor", Journal of the Japan Society of Powder and Powder Metallurgy **45**, 135–139 (1998).
6. H. Yasuoka, S. Tochihara, M. Mashino, and H. Mazaki, "Material parameters of YBa_2Cu_3-O_y in the Kim–Anderson critical-state model", Physica C **305**, 125–138 (1998).
7. S. Tochihara, H. Yasuoka, and H. Mazaki, "Surface barriers in a single-crystal $YBa_2Cu_3O_y$ bulk superconductor", Physica C **312**, 28–34 (1999).
8. S. Tochihara, H. Yasuoka, H. Mazaki, M. Osada, and M. Kakihana, "Lower critical fields of $Bi_2Sr_2CaCu_2O_{8+d}$ and $YBa_2Cu_3O_{7-d}$ single crystals", Journal of Applied Physics **85**, 8299–8306 (1999).
9. S. Tochihara, M. Mashino, H. Yasuoka, H. Mazaki, M. Osada, and M. Kakihana, "Effect of Ca doping on the lower critical field of $YBa_2Cu_3O_{7-d}$ single crystals", Advances in

Superconductivity **XI** (Proceedings of 11th International Symposium on Superconductivity), 267–270 (1999).

(2) Other Publications

1. H. Yasuoka, H. Mazaki, S. Tochihara, M. Kakihana, and M. Yoshimura, "Critical currents of ceramic superconductors induced by pulsed magnetic fields", Journal of Applied Physics **74**, 6759–6766 (1993).
2. 奈須野善之, 垣花眞人, 長田実, 安岡宏, 栃原信二郎, 間崎啓匡, 藤森宏高, 八島正知, 吉村昌弘, "錯体重合法による Ca 置換 $YBa_2Cu_3O_{7-d}$ の合成とラマン散乱", 粉体および粉末冶金 **43**, 1065–1069 (1996).
3. H. Yasuoka, S. Tochihara, H. Mazaki, M. Komatsu, and M. Nagano, "Magnetic response of a single-crystal $YBa_2Cu_3O_y$ thin film", Proceedings of the 16th International Cryogenic Engineering Conference / International Cryogenic Materials Conference (ICEC16/ICMC), 1537–1540 (1996).
4. P. Berastegui, S.G. Eriksson, L.G. Johansson, M. Kakihana, M. Osada, H. Mazaki, and S. Tochihara, "A neutron diffraction study of Ca doped and oxygen deficient YBa_2Cu_3-O_{7-d}", Journal of Solid State Chemistry **127**, 56–63 (1996).
5. 井上京由, 長田実, 垣花眞人, 栃原信二郎, 安岡宏, 間崎啓匡, 八島正知, "錯体重合法による $Bi_{2.1}Sr_{1.9-x}La_xCuO_{6+d}$ の合成とそのラマン散乱", 粉体および粉末冶金 **44**, 137–141 (1997).
6. S. Tochihara, H. Yasuoka, and H. Mazaki, "Modification of the Bean critical-state model with surface barriers and lower critical fields", Journal of the Japan Society of Powder and Powder Metallurgy **44**, 168–172 (1997).
7. H. Yasuoka, S. Tochihara, Y. Tanaka, and H. Mazaki, "Temperature dependence of the material parameters in the Kim–Anderson critical-state model for a melt-processed YBa_2Cu_3-O_7", Physica C **282–287**, 2211–2212 (1997).
8. 原島賢一郎, 栃原信二郎, 安岡宏, 間崎啓匡, 長田実, 井上京由, 垣花眞人, "溶融 YBa_2Cu_3-O_7 の交流磁化応答における微弱直流磁場印加効果", 粉体および粉末冶金 **45**, 655–660 (1998).
9. S. Tochihara, K. Harashima, H. Yasuoka, H. Mazaki, M. Osada, and M. Kakihana, "Tem-

perature dependence of lower critical fields in a single-crystal $Bi_2Sr_2CaCu_2O_{8+d}$ bulk superconductor", Advances in Superconductivity X (Proceedings of 10th International Symposium on Superconductivity), 63–66 (1998).

10. M. Kakihana, M. Osada, S. Tochihara, H. Yasuoka, and H. Mazaki, "Polymerizable complex synthesis of multi-component oxides including high-temperature superconducting oxides", High-Temperature Superconductors and Novel Inorganic Materials, ed. by G. Van Tendeloo, E.V. Antipov, and S.N. Putilin, 27–32 (1999).

11. S. Tochihara, A. Goto, H. Yasuoka, H. Mazaki, M. Osada, and M. Kakihana, "Magnetic response of Y/Pb doped single-crystal $Bi_2Sr_2CaCu_2O_{8+d}$ superconductors", IEEE Transactions on Applied Superconductivity **9** (Proceedings of Applied Superconductivity Conference 1998), 2320–2323 (1999).